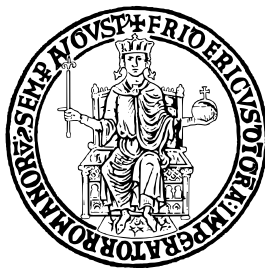


UNIVERSITÀ DEGLI STUDI DI NAPOLI FEDERICO II



SCUOLA POLITECNICA E DELLE SCIENZE DI BASE

DIPARTIMENTO DI FISICA "ETTORE PANCINI"

CORSO DI LAUREA MAGISTRALE IN FISICA

ELECTRODYNAMICS OF
TUNNEL-FERROMAGNETIC JOSEPHSON
JUNCTIONS FOR QUANTUM DEVICES

Relatori

Prof. Francesco TAFURI

Dr. Davide MASSAROTTI

Candidata

Antonella RESTINO

MATR. N94000666

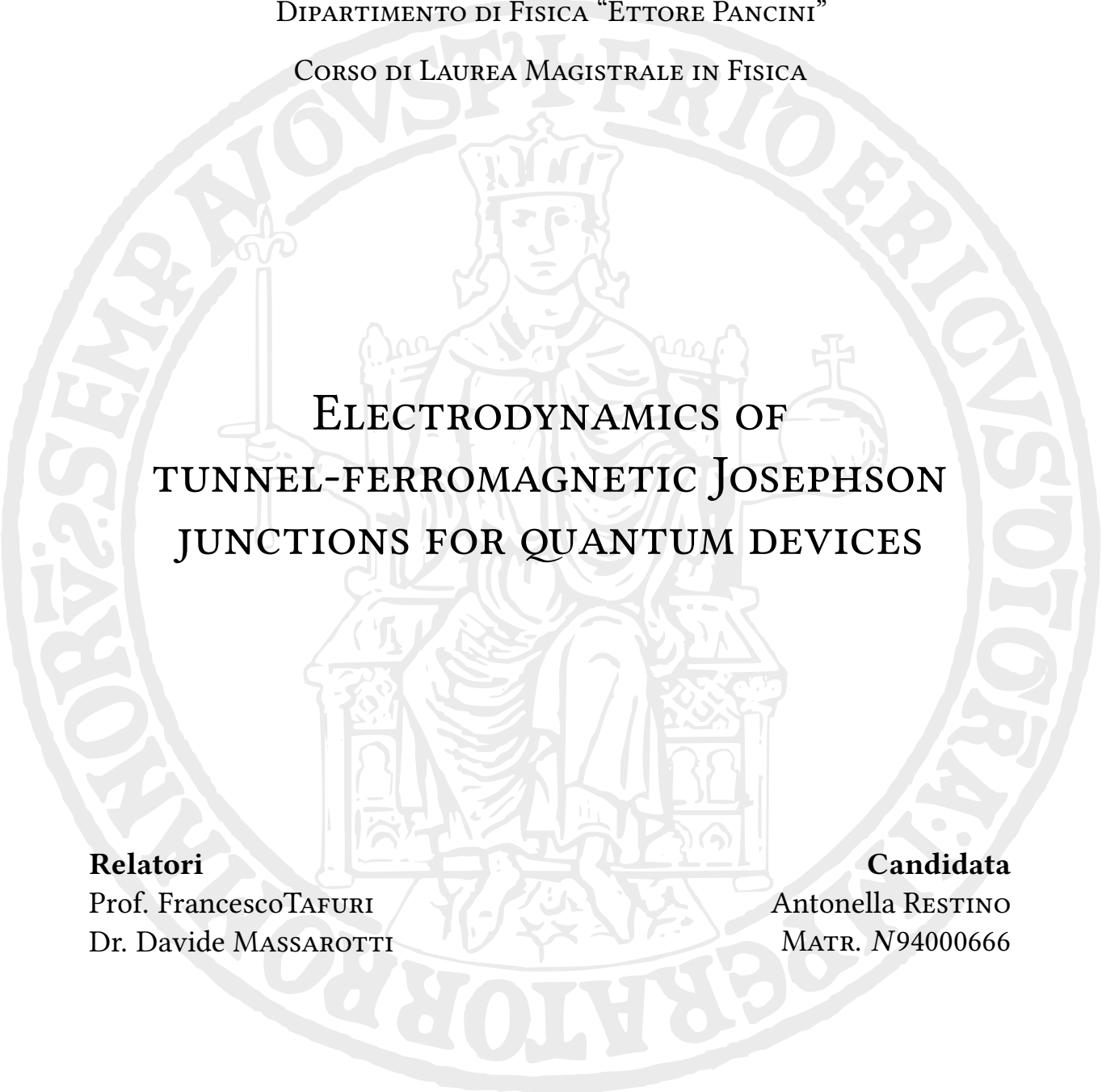
Anno Accademico 2022–2023

UNIVERSITÀ DEGLI STUDI DI NAPOLI FEDERICO II

SCUOLA POLITECNICA E DELLE SCIENZE DI BASE

DIPARTIMENTO DI FISICA "ETTORE PANCINI"

CORSO DI LAUREA MAGISTRALE IN FISICA

The seal of the University of Naples Federico II is a large, faint watermark in the background. It features a central figure, likely a saint or a historical figure, seated on a throne and wearing a crown. The figure is surrounded by a circular border containing Latin text. The text is partially legible as "SEMPER AVGVSTVS FERIO ERICVS OTORAV" and "BATORBO".

ELECTRODYNAMICS OF
TUNNEL-FERROMAGNETIC JOSEPHSON
JUNCTIONS FOR QUANTUM DEVICES

Relatori

Prof. Francesco TAFURI

Dr. Davide MASSAROTTI

Candidata

Antonella RESTINO

MATR. N°94000666

Anno Accademico 2022–2023

Contents

Introduction	iv
1 Conventional Josephson junctions	3
1.1 Introduction to superconductivity	3
1.2 Ginzburg-Landau theory	5
1.3 Josephson Effect	8
1.3.1 Josephson equations	8
1.3.2 Magnetic field effects	10
1.3.3 Phase dynamics	14
1.4 Ferro-Transmon Qubit prospective	26
2 Magnetic Josephson junctions	27
2.1 Ferromagnetic materials	27
2.1.1 Domains and magnetization processes	28
2.2 Proximity effect at S/N interface	33
2.3 Proximity effect at S/F interface	36
2.3.1 SFS junction in magnetic field	39
2.3.2 SIFS JJs	41
2.4 MJJs for digital and quantum electronics	45
3 Experimental setup	49
3.1 Triton Dilution fridge	49
3.2 Filtering systems and electronics	52
3.2.1 DC setup	52
3.3 Readout electronics	55
3.3.1 $I(V)$ measurements	55
3.3.2 Measurements in magnetic fields	57
3.3.3 Conductance measurements	58
3.3.4 Switching Current Distribution measurements	58
3.4 Samples scheme	60

4	Data analysis	65
4.1	Characterization of the samples	65
4.1.1	Current-Voltage characteristics and Conductance	67
4.2	Magnetic field dependence	70
4.3	Switching current distributions (SCDs)	74
	Bibliography	83

Introduction

In the field of quantum technology, the search for superconducting quantum bits (qubits) has inspired a relentless pursuit of innovation in the fabrication, characterisation and analysis of Josephson junctions (JJs), the fundamental components of all superconducting qubits. The main motivation for the development of Josephson junction qubits has been their potential application as building blocks for a quantum computer. This is why companies such as IBM and Google now have large teams of researchers trying to make a significant number of Josephson junction qubits work well together [1]. Superconducting qubits have become a dominant platform for realising large-scale quantum processors [2], which would perform in the near future remarkable computational tasks far beyond the capabilities of classical computers, such as prime factorisation [3] and the simulation of complex quantum systems [4]. Unlike other forms of quantum computing, such as electron spins, trapped ions, ultracold atoms and nitrogen-vacancies in diamond, where quantum information is stored in natural microscopic two level systems, these circuits allow their properties, including their characteristic frequencies to be designed with a high degree of flexibility and scalability [2].

Among the large variety of superconducting qubits that have been designed to date, the transmon has become one of the most widely used since its creation and forms a key part of many scalable quantum information processing architectures using superconducting circuits [5]. Its frequency tunability through the use of the magnetic flux that threads a loop geometry is one of the key advantages. This flux tuneability, which allows for faster gate operations, has however important drawbacks, the most important the susceptibility to flux-noise, which reduces the typical relaxation and phase coherence times. Furthermore, the milliamperic currents that control the flux generate crosstalk between qubits and heating, thus complicating the integration [6, 7]. Recently, a proof-of-concept for a hybrid ferromagnetic transmon qubit, known as ferro-transmon, has been proposed [8]. If it is successfully implemented, this novel approach to qubit architecture has the potential to discover new avenues for engineering superconducting quantum processors.

The main concept behind this architecture is to use a magnetic Josephson junction (MJJ) as the magnetic sensitive component of the superconducting quantum circuit instead of a typical tunnel Superconductor-Insulator-Superconductor (SIS) JJ, which is commonly used as the non-linear element in qubit architectures. This choice allows an alternative tuning of the qubit frequency using magnetic field pulses. MJJs made of a Superconductor-

Ferromagnet-Superconductor (SFS) structure have issues with quasiparticle dissipation, which compromise the qubit performance. However, SISFS JJs have a different structure that allows high quality factors and low quasiparticle dissipation, achieved by including an insulator barrier [9]. Since superconducting quantum circuits almost exclusively rely on aluminium technology, aluminium-based SISFS have been realised for the first time [10].

In this thesis, two types of Josephson junctions are compared in order to identify the main characteristics of a SISFS JJ: the first without ferromagnet; the second with a layer of ferromagnetic material, Permalloy ($\text{Ni}_{80}\text{Fe}_{20}$). The thesis is organised in the following way: the first chapter presents theoretical notions necessary to understand the Josephson effect and the behaviour of a JJ in a magnetic field. Then the phase dynamics of underdamped and moderately damped JJs will be addressed, both in the thermal and in the quantum regime.

The second chapter is focussed on MJJs. After providing a brief overview of the key characteristics of ferromagnetic materials, we proceed to examine SFS and SISFS JJs, discussing their similarities and differences. Then, our discussion is focused on the realization of scalable SISFS JJs, demonstrating that they are the smallest memory elements compatible with standard superconducting circuits [11].

In the third chapter the experimental setup will be described with a special focus on the cryogenic (dilution refrigerator) and room temperature measurement set-up. The role of filters and temperature control techniques within the cryostat are discussed. In the fourth chapter, transport properties of SIS and SISFS Josephson junctions based on aluminium are discussed. In particular, the main electrodynamic parameters of the fabricated JJs are presented. The dependence on the magnetic field and the conductance-voltage trends for tunnel and ferromagnetic junctions are then examined. Finally, in the last section of the chapter, the measurements of switching current distributions are reported, thus providing fundamental insights of the measured junctions.

–1–

Conventional Josephson junctions

The purpose of this chapter is to present the principal notions and theories that we will reference in this thesis. Firstly, after a brief introduction to the notion of superconductivity, the basic principles of the Josephson junction and how it operates when subjected to a magnetic field are presented, emphasising the physical quantities involved in the different processes. After that, we'll discuss the theory of phase dynamics of Josephson devices, which is necessary for a complete understanding of their electrodynamics.

1.1 Introduction to superconductivity

In 1911, while studying the properties of matter at very low temperature, Kamerlingh Onnes discovered that the electrical resistance of mercury goes to zero below 4.2K. This was the very first observation of the phenomenon of superconductivity.

Below the critical temperature T_c , materials undergo a transition into the superconducting state. This state is characterized by two main properties. Firstly, materials in the superconducting state display zero resistivity to the flow of electrical current. Secondly, weak magnetic fields do not penetrate the superconductor but concentrate on its surface, resulting in perfect diamagnetism. In the latter case there is thus a simultaneous transition from a positive finite value of the magnetic susceptibility χ for $T > T_c$ to a value of $\chi = -1$ for $T < T_c$.

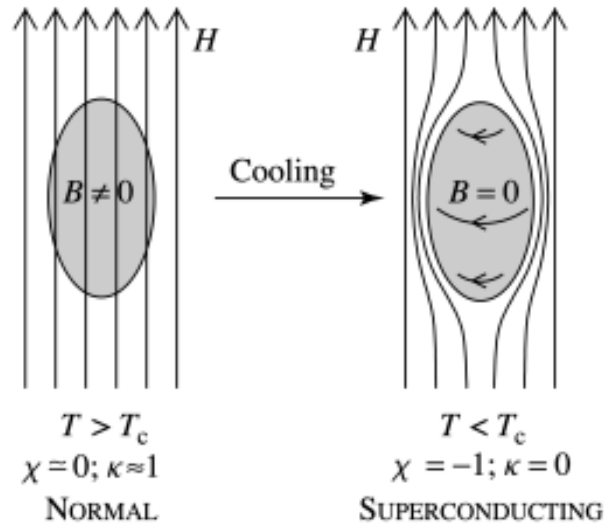


Figure 1.1: Illustration of the Meissner effect: at temperatures higher than T_c (normal state), magnetic field lines pass through the material; at temperatures lower than T_c (superconducting state), the field is expelled from the material [12].

The combination of these two properties provides a clear distinction between a superconductor and a perfect conductor (which has unique transport properties associated with zero resistance) [13].

Consider a system initially exposed to a zero magnetic field and at temperature $T > T_c$, and then cooled until $T < T_c$. At this point, by turning on the magnetic field and being below the critical temperature, we observe that the magnetic field lines are expelled from the superconducting system. Now suppose we reverse the order of events: at temperature $T > T_c$ we turn on the magnetic field and there will be a flux associated with the material, then we cool the material to a temperature $T < T_c$, again there will be an ejection of the magnetic field flux lines from the superconductor. The ejection of the magnetic field is due to the generation of surface screening currents, which in turn induce a magnetic field that balances the external magnetic field. This field expulsion phenomenon is known as the Meissner effect [14] (Fig. 1.1).

The first phenomenological model to explain the transitions to the superconducting state, and in particular the Meissner effect, was proposed in 1935 by F. and H. London using two equations. Their idea was to treat the superconducting system as a two-fluid model, where the current density flowing in a superconductor is given by the sum of the normal current density and the superconducting current density.

The first London equation describes the dynamics of electrons in the absence of collisions and implies that a perfect conductor cannot sustain an electric field. The second London equation predicts that a superconductor under stationary conditions cannot support a magnetic field inside it, except for a thin surface layer. Indeed the magnetic field penetrates into the superconductor within a characteristic distance, the *London penetration length*: using the theory of Ginzburg and Landau, it is derived to be

equal to

$$\lambda_L = \sqrt{\frac{m_s c^2}{4\pi n_s q^2}} \quad (1.1)$$

where, m_s is the mass, n_s represents the superconducting electron density and q is the charge.

The value of the London penetration length depends on the material.

London penetration length increases slowly at low temperatures and diverges as it approaches the transition temperature T_c . The empirical law predicting the temperature dependence of the London penetration depth is

$$\lambda_L(T) = \lambda_L(0) \left[1 - \left(\frac{T}{T_c} \right)^4 \right]^{-1/2} \quad (1.2)$$

To understand what happens when an external magnetic field is applied to a superconductor, consider a semi-infinite sheet of superconducting material placed in a region of space with a uniform magnetic field with a direction parallel to the z -axis, as shown in Figure 1.2.

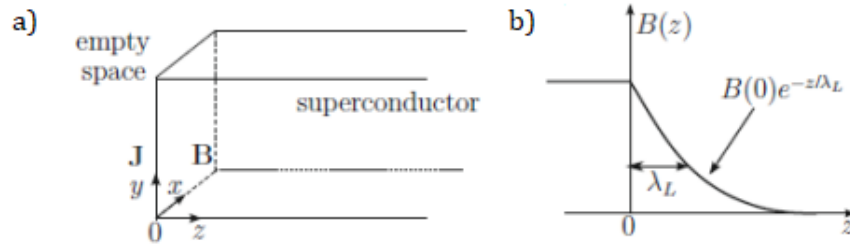


Figure 1.2: a) Geometry of the semi-infinite superconducting plate; b) penetration length of the magnetic field parallel to the surface as a function of the z axis.

So a magnetic field parallel to the interface, for example along the z -axis, penetrates into the superconductor and decays exponentially according to the behaviour $B(z) = B(0)e^{-z/\lambda_L}$ [15].

1.2 Ginzburg-Landau theory

An important theoretical approach explaining superconductivity is the macroscopic phenomenological theory of Ginzburg-Landau (1950) [16]. This theory focuses primarily on current carriers in the superconducting state, called superparticles, which were later identified, thanks to the BCS (Bardeen-Cooper-Schrieffer) microscopic theory, as special bosonic entities, called Cooper pairs, consisting of electron pairs with opposite spin, mass $m^* = 2m_e$ and charge $e^* = 2e$ [17].

To describe the superconducting state, a macroscopic complex function is introduced, the order parameter ψ , which characterises the level of order reached in the transition from the disordered phase for $T > T_c$ (normal metal) to the ordered phase for $T < T_c$ (superconducting phase), the modulus of which is proportional to the density of Cooper pairs [18].

$$\psi(\vec{r}) = \sqrt{n_s(\vec{r})} e^{i\theta(\vec{r})} \quad (1.3)$$

where the real quantity $\theta(\vec{r})$ is the phase. $\psi(\vec{r})$ at a given temperature T is related to the local number of the carriers in the superconductor by the relation:

$$n_{pairs} = |\psi(\vec{r})|^2 \quad (1.4)$$

The thermodynamic properties of the superconducting state can be described in terms of the free energy $F(T) = U - TS$, where U is the internal energy, T is the temperature and S is the entropy, according to the mean-field theories [12]. Because we are near the transition, the order parameter is small. This led Ginzburg and Landau to suggest that near the critical temperature the free energy can be expressed as a series of the order parameter $\psi(\vec{r})$ [16]:

$$F_S(\vec{r}, T) = F_N(\vec{r}, T) + \alpha|\psi|^2 + \frac{\beta}{2}|\psi|^4 + \frac{1}{2m}|(-i\hbar\vec{\nabla} - 2e\vec{A})\psi|^2 + \frac{B^2}{2\mu_0} \quad (1.5)$$

where $F_N(T)$ is the free energy in the normal state, α and β are two phenomenological parameters and the last term is the vacuum energy of the magnetic field. The magnetic vector potential A is such that $\vec{B} = \nabla \times \vec{A}$. $F_S(T)$ is a functional of the order parameter ψ . We remark here that since all the terms in eq. (1.5) represents energy densities, the total free energy of the system is

$$F_S(T) = \int_V d\vec{r} F_S(\vec{r}, T) \quad (1.6)$$

We now apply the variational method to find the equilibrium condition $\delta F_S(T) = 0$, which gives us the *first* and *second Ginzburg-Landau equations*:

$$\begin{aligned} \alpha\psi + \beta|\psi|^2\psi + \frac{1}{2m} \left(-i\hbar\vec{\nabla} - \frac{2e}{c}\vec{A} \right)^2 \psi &= 0 \\ \vec{J}_s &= \frac{e\hbar}{2im} (\psi^*\nabla\psi - \psi\nabla\psi^*) - \frac{2e^2}{mc} \psi^*\psi\vec{A} \end{aligned} \quad (1.7)$$

Let us consider the first equation of GL 1.7. In the absence of a magnetic field it becomes:

$$\alpha(T)\psi + \beta|\psi|^2\psi - \frac{1}{2m}\hbar^2\nabla^2\psi = 0, \quad (1.8)$$

from which dividing by α gives:

$$\psi + \frac{\beta}{\alpha(T)}|\psi|^2\psi - \frac{\hbar^2}{2m\alpha(T)}\nabla^2\psi = 0. \quad (1.9)$$

The coefficient for the second derivative in the first GL equation represents a new characteristic length: the *coherence length* ξ defined as the characteristic length over which the macroscopic wave function ψ varies

$$\xi = \sqrt{\frac{\hbar^2}{2m\alpha(T)}}. \quad (1.10)$$

Let us assume that, in the vicinity of T_c , $\alpha(T) \sim \alpha_0(T - T_c)$ and $\beta(T) \sim \beta_0$, with α_0 and β_0 defined as positive and such that $\alpha(T)$ vanishes at T_c and is negative below T_c . In this way, we obtain a temperature dependence given by [12]:

$$\xi = \frac{\hbar^2}{2m|\alpha_0|} \begin{cases} \left(\frac{T}{T_c} - 1\right)^{-\frac{1}{2}} & \text{for } T > T_c \\ \left(1 - \frac{T}{T_c}\right)^{-\frac{1}{2}} & \text{for } T < T_c \end{cases} \quad (1.11)$$

The *coherence length*, together with the *London penetration length*, helps us to understand the difference between a type 1 and a type 2 superconductor.

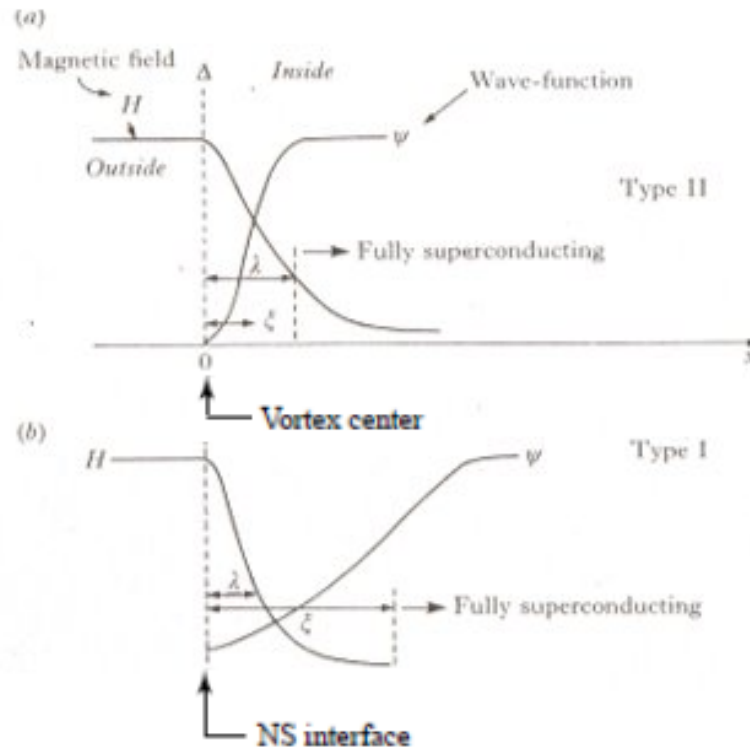


Figure 1.3: Variation of magnetic field \vec{H} and wave function ψ at the normal metal - superconductor interface. a) In a type I superconductor we have $\lambda_L < \xi$, instead in a type II superconductor b) we have $\lambda_L > \xi$ [12].

-
- A type I superconductor will not accept a magnetic field until a critical applied field H_c is reached. Above this value, the field completely destroys the superconducting state and it reverts to the normal state.
 - In a type II superconductor, the external magnetic flux is completely expelled until a first critical field H_{C1} is reached, at which point a mixed state occurs in which the flux partially penetrates the superconducting region in the form of vortices, each carrying a flux quantum defined as $\phi_0 = \frac{h}{2e}$. When $H > H_{C2} > H_{C1}$, there is complete penetration of the field, again resulting in the destruction of the superconducting state.

1.3 Josephson Effect

One of the most important theoretical breakthroughs in superconducting physics came in 1962, when Brian D. Josephson first predicted that a non-dissipative current could flow between two superconducting electrodes separated by insulating barriers of a few nanometres. This device, known as a Josephson junction (JJ), has become a widely used tool in science and for engineering applications in superconducting electronics. From a fundamental physics point of view, the Josephson effect is unique in that it provides direct access to the phase difference φ of the macroscopic wave function that describes the superconducting state. We will therefore give some hints about the quantum nature of the Josephson effect in insulating barrier junctions (SIS), commonly referred to as conventional JJs, since their properties have been widely represented by models obeying BCS theory.

1.3.1 Josephson equations

The Josephson junction consists of two superconducting electrodes separated by a thin insulator (SIS). The operation of the Josephson junction is based on the physical phenomenon of the tunneling of Cooper pairs through the insulating layer from one superconductor to the other, so that the whole system behaves as a single superconductor. Therefore, in order to understand the Josephson effect, let us look at the simplified model of a Josephson junction (fig. 1.4). There is a Josephson effect as long as the macroscopic wave functions of the two electrodes $\psi_L = |\psi_L|e^{i\varphi_L}$ and $\psi_R = |\psi_R|e^{i\varphi_R}$ overlap in the barrier region, giving rise to a finite current of Cooper pairs, the supercurrent I_s . This is a non-dissipative current, i.e. there is no finite voltage across the junction in the superconducting state.

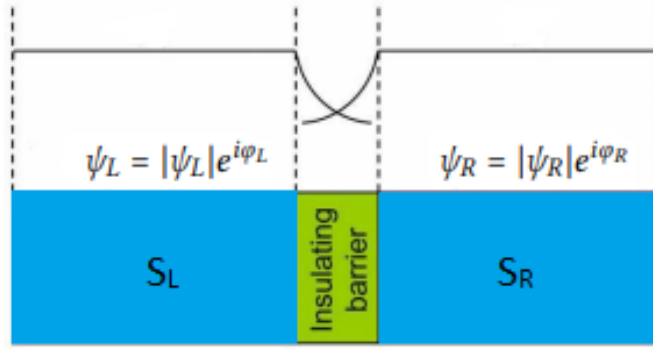


Figure 1.4: Qualitative behaviour of the superconducting wave functions in a JJ. In the central region it is possible to observe the overlapping of the wave functions.

The first and second Josephson equations are the following [17]:

$$\begin{cases} I_s = I_c \sin \varphi \\ \frac{\partial \varphi}{\partial t} = \frac{2eV}{\hbar} \end{cases} \quad (1.12)$$

where $\varphi = \varphi_L - \varphi_R$ is the phase difference between the two superconducting electrodes φ_L and φ_R . The first equation states that the supercurrent flowing through the junction depends only on the phase difference between the two superconducting electrodes. I_c is the critical current of the junction. The critical current is the maximum current that can flow through the junction without a voltage drop across it. The second equation predicts the behaviour of the phase difference as a function of time when a finite voltage appears across the junction.

The first Josephson equation defines the current-phase relation (CPR) of the device and is fundamental to calculate most of junction properties [1]. A more general expression of I_s includes the higher harmonics for unconventional junctions:

$$I_s = I_c \sin \varphi + \sum_{m=2} I_{cm} \sin(m\varphi) \quad (1.13)$$

We note from the Josephson equations that even at $V = 0$, current can flow by biasing the current up to the maximum value of the supercurrent, I_c . Instead, in the presence of a potential difference $V \neq 0$, the phase varies with time

$$\varphi = \varphi_0 + \frac{2eV}{\hbar} t \quad (1.14)$$

and an alternating current appears

$$I = I_c \sin \left(\varphi_0 + \frac{2eV}{\hbar} t \right) \quad (1.15)$$

with a frequency $\omega = 2\pi\nu = \frac{2eV}{\hbar}$. This is referred to as the *a.c. Josephson effect*. The ratio between frequency and voltage is constant and is given by:

$$\frac{\nu_0}{V} = \frac{2e}{h} = 483.6 \text{MHz}/\mu\text{V} \quad (1.16)$$

The experimental observation of this phenomenon can be seen in the case of a junction subjected to microwaves with a DC voltage bias, where there are steps in the current at constant voltage. Such steps were first observed by Shapiro [19] in 1963 and are therefore called *Shapiro steps*. The steps current occurs at voltage:

$$V_n = \frac{nh}{2e} \nu_0 \quad (1.17)$$

where n is an integer number.

Above we have introduced the critical current of a junction in a somewhat phenomenological way. The expression for the critical current can be derived rigorously on the basis of the microscopic BCS theory, and it was first done by V. Ambegaokar and A. Baratoff [20]. The resulting Ambegaokar-Baratoff (AB) relation for the critical current of the junction reads:

$$I_c(T) = \frac{\pi}{2eR_N} \Delta(T) \tanh\left(\frac{\Delta(T)}{2k_B T}\right), \quad (1.18)$$

where an increase in temperature causes a suppression of the critical current I_c . R_N is the normal-state resistance and Δ is the superconducting gap [20]. For $T = 0$, Eq. 1.18 takes the following simplified form

$$I_c(0) \approx \frac{\pi\Delta}{2eR_N}. \quad (1.19)$$

1.3.2 Magnetic field effects

One of the most useful and exciting aspects of the Josephson junction is its behaviour in a magnetic field. Let us consider a planar junction, as shown in the figure 1.5, in the x - y plane and apply a magnetic field along y . From the *second Ginzburg-Landau equation*, it is possible to derive the phase gradient as a function of the current density:

$$\vec{\nabla}\varphi_{R,L} = \frac{2e}{\hbar c} \left(\frac{mc}{2e^2|\psi|^2} \vec{J}_s + \vec{A} \right) \quad (1.20)$$

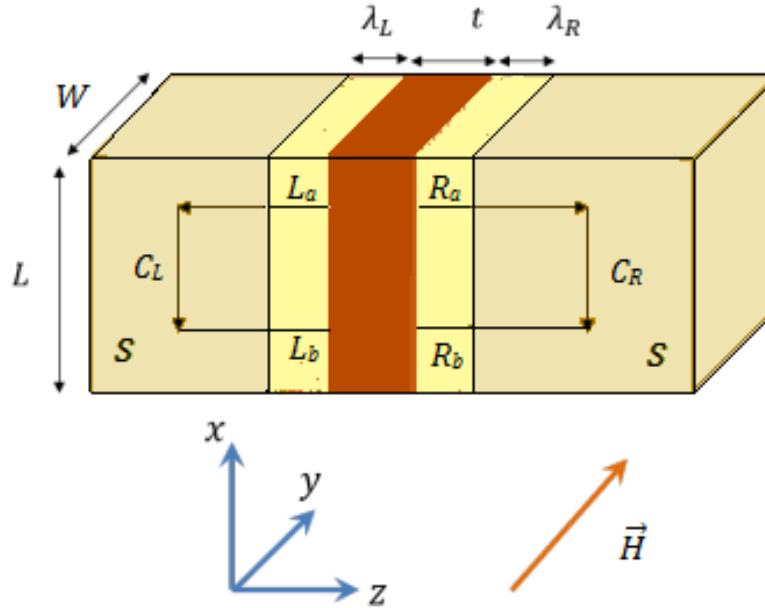


Figure 1.5: Scheme of a standard Josephson junction in an external magnetic field H_y . The areas in yellow indicate the regions where the field penetrates the superconducting electrodes.

To obtain the relationship between the supercurrent passing through the junction and the applied magnetic field, we need to integrate along the path shown in the figure 1.5. Assuming that the thickness of the superconducting films is much greater than the London penetration length, we can extend the contours C_L and C_R outside the penetration region where \vec{J}_s current density becomes zero. We choose the integration paths shown in the figure so that they are perpendicular to the supercurrent \vec{J}_s inside the penetration region. In this way we obtain [17]

$$\begin{aligned}
 \varphi(x + dx) - \varphi(x) &= [\varphi_{Lb}(x + dx) - \varphi_{Rb}(x + dx)] - [\varphi_{La}(x) - \varphi_{Ra}(x)] \\
 &= \frac{2e}{\hbar c} \left[\int_{C_L} \vec{A} \cdot d\vec{l} + \int_{C_R} \vec{A} \cdot d\vec{l} \right] \\
 &= \frac{2e}{\hbar c} \oint \vec{A} \cdot d\vec{l}
 \end{aligned} \tag{1.21}$$

In the last expression, the integral along the two paths is equal to the circuit of the vector potential and thus to the magnetic flux. Switching to differential notation, we can rewrite the previous equation as

$$\frac{d\varphi}{dx} = \frac{2e}{\hbar c} (2\lambda + t) H_y \tag{1.22}$$

which, when integrated along x , becomes

$$\varphi = \frac{2e}{\hbar c} d_m H_y x + \varphi_0 \tag{1.23}$$

where

$$d_m = (\lambda_L + \lambda_R + t) \quad (1.24)$$

is the magnetic thickness, i.e., the thickness penetrated by the external magnetic field H_y [15, 21], with λ_L and λ_R the London penetration depths in the two superconductors, t the thickness of the barrier and φ_0 is the phase difference for $x = 0$. This relation is valid until the electrodes can be considered bulk, i. e. when $d_{L(R)} > \lambda_{L(R)}$, where $d_{L(R)}$ are the left (right) electrode thicknesses. For junctions with $d_{L(R)} < \lambda_{L(R)}$, instead, the effective magnetic spacing becomes

$$d' = t + \lambda_L \tanh\left(\frac{d_L}{2\lambda_L}\right) + \lambda_R \tanh\left(\frac{d_R}{2\lambda_R}\right). \quad (1.25)$$

Substituting equation 1.23 into the first Josephson equation 1.12 and integrating over the entire junction area, we obtain the analytical expression for the critical current $I_c(H)$. In particular, a rectangular junction with a lateral size L and a uniform tunneling current distribution shows a dependence of the maximum supercurrent on the applied magnetic field in the form of a Fraunhofer-like diffraction pattern as shown in figure 1.6:

$$I_c(\Phi) = I_c \left| \frac{\sin\left(\frac{\pi\Phi}{\Phi_0}\right)}{\pi \frac{\Phi}{\Phi_0}} \right| \quad (1.26)$$

where $\Phi = H_y L d_m$ is the magnetic flux and $\Phi_0 = \frac{h}{2e} = 2.07 \cdot 10^{-15} \text{ Wb}$ is the magnetic flux quantum. The analogy with the course of the light intensity in the Fraunhofer diffraction produced by a slit of the same shape as the barrier is obvious, where in this case the minima are found at values of the magnetic field flux multiples integer of the flux quantum, arranged symmetrically and uniformly with respect to to the origin [17]. The periodicity of I_c is defined as half the amplitude of the first lobe of the Fraunhofer pattern. In terms of magnetic field it is given by

$$\Delta H = \frac{\Phi_0}{L(\lambda_L + \lambda_R + t)} \quad (1.27)$$

and if the two superconductors are equal ($\lambda_L = \lambda_R$) this periodicity furnishes a method for the determination of the London penetration depth. This applies as long as the thicknesses of the superconducting films are large compared with λ_L . When this condition is no longer satisfied, eq. 1.27 is modified as

$$\Delta H = \frac{\Phi_0}{L \left(\lambda_L \tanh \frac{d_L}{2\lambda_L} + \lambda_R \tanh \frac{d_R}{2\lambda_R} + t \right)} \quad (1.28)$$

For circular JJs with a uniform zero-field tunneling current distribution, modulation takes the form of an Airy pattern [17]

$$I_c(\Phi) = I_c \left| \frac{2J_1\left(\frac{\pi\Phi}{\Phi_0}\right)}{\frac{\pi\Phi}{2\Phi_0}} \right| \quad (1.29)$$

where $I_c = \pi R^2 J_c$ and $J_1(x)$ is the Bessel function of the first kind. In this case, the flux threading the junction is: $\Phi = \mu_0 H 2Rd_m$, with R the radius of the junction. For H oriented along \hat{x} or \hat{y} and J_c uniform, the secondary lobes are of much smaller amplitude and the minima are not integer multiples of the flux quantum Φ_0 , in contrast to a rectangular junction. A qualitative sketch can be looked at in Fig. 1.6.

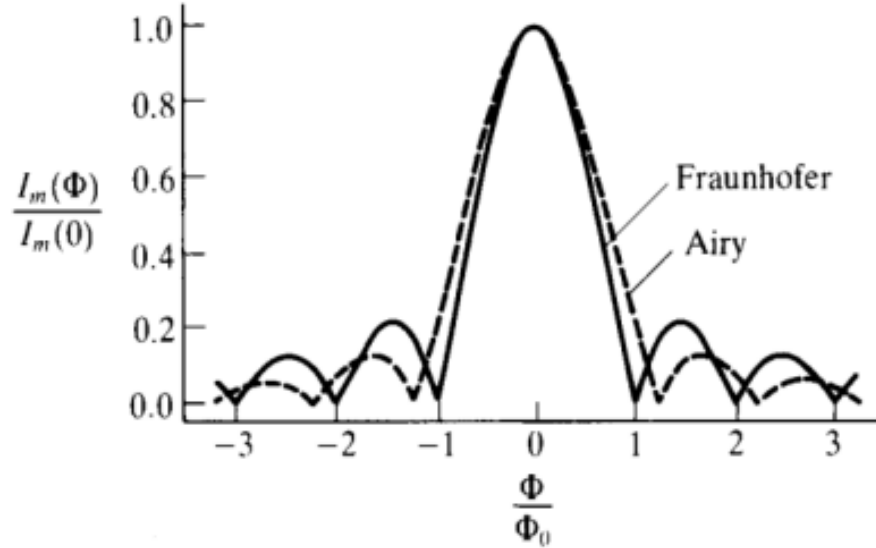


Figure 1.6: Dependence of the maximum supercurrent on the external flux for differently shaped JJs. Square junctions follow a Fraunhofer pattern (solid line), circular junctions follow an Airy diffraction pattern (dashed line) [15].

$I_c(\Phi)$ measurements are an important tool for characterising the quality of the junction. Deviations from the expected behaviour of $I_c(H)$, such as minima with non-zero current, suppression of the amplitude of some lobes, asymmetry of the pattern and inaccurate definition of the junction geometry (e.g. patterning problems) or spatial inhomogeneities in the tunnel barrier, can be related to non-uniform current distribution, arbitrary orientation of the applied in-plane magnetic fields or structural fluctuations [17]. The periodicity for a circular junction is given by [22]

$$\Delta H = \frac{\Phi_0}{2Rd} \quad (1.30)$$

This description is valid within the short junction limit, i.e., when R is smaller than the Josephson penetration depth λ_J :

$$\lambda_J = \sqrt{\frac{\Phi_0}{2\pi\mu_0 J_c d_m}}, \quad (1.31)$$

which is defined as the penetration length for the phase-difference φ . In this limit, the self-field due to the current flowing in the junction electrodes can be neglected. In the

long junction limit, i.e. for a JJ with transverse dimensions larger than λ_J , instead, the self-field due to the current flowing in the electrodes cannot be neglected and a distortion of the Fraunhofer pattern is experimentally measured [17].

1.3.3 Phase dynamics

Current-voltage ($I-V$) curves are the first indication of the nature of the junction. Through them, it is possible to define the transport mechanism of a junction, its electrodynamics and understand its potential applications for digital and quantum circuits.

When the temperature of the system is finite ($T > 0$), we excite several quasiparticles, a number of Cooper pairs, due to thermal excitation, break and single electrons can flow through the junction. This happens when the voltage at the ends of the junction is non-zero. For temperatures close to the transition temperature ($T < T_c$) the energy $2\Delta(T)$ (Δ is the energy gap) required to break up a Cooper pairs is much smaller than $k_B T$. Therefore, almost all Cooper pairs are broken up and the concentration of quasiparticles is close to the electron density in the normal state [23]. Consequently, the current follows the usual ohmic law

$$I_N = G_N V = R_N^{-1} V \quad (1.32)$$

where R_N is always identified as the normal resistance and G_N is the normal conductance of the junction. We observe this ohmic regime due to quasiparticles also for junction voltage above the so-called gap voltage, $V_g = (\Delta_L + \Delta_R)/e$, at all temperatures.

At $T = 0$, the equivalent conductance for the normal channel is given by [18]

$$G_N(V) = \begin{cases} 0 & \text{for } |V| < 2\Delta/e \\ \frac{1}{R_N(T)} & \text{for } |V| \geq 2\Delta/e. \end{cases} \quad (1.33)$$

At finite temperatures, thermally excited quasiparticles can form at voltages below the gap voltage with a finite resistance $R_{sg}(T)$, called the subgap resistance. Thus for $T > 0$ the conductance is given by [18]

$$G_N(V) = \begin{cases} \frac{1}{R_N} & \text{for } |V| \geq 2\Delta/e \\ \frac{1}{R_{sg}(T)} & \text{for } |V| < 2\Delta/e. \end{cases} \quad (1.34)$$

Here, it has been taken into account that the energy gap, and thus the gap voltage, is temperature dependent. It's clear that the non superconducting channel results in a nonlinear conductance $G_N(V, T)$ that depends on voltage and temperature [23].

Indeed, in addition to the supercurrent, one can observe the displacement current due to the finite capacitance of the junction and a dissipative quasi-particle current responsible for the ohmic behaviour of the circuit. As the voltage between the two superconducting electrodes varies over time, a displacement current I_D begins to flow through the device:

$$I_D = C \frac{dV}{dt} \quad (1.35)$$

The junction's capacitance can be schematised as a capacitor with flat, parallel planes. For a planar tunnel junction with area A and an insulating barrier of thickness d the capacitance is just given by

$$C = \frac{\epsilon_r \epsilon_0 A}{d}. \quad (1.36)$$

The voltage dependence of R is considered in the framework of nonlinear resistive shunt junction models (RSJN) and microscopic tunnel junction models (TJM). In RSJN model [24, 25], the term $I_N = V/R_N$ has been for instance approximated by a simple piecewise-linear behavior [1]:

$$I_N(V) = V \cdot \begin{cases} 1/R_L \text{ for } |V| < V_g \\ 1/R_N \text{ for } |V| > V_g \end{cases} \quad (1.37)$$

or by a power-law:

$$I_N(V) = \frac{V}{R_N} \frac{(V/V_g)^n}{1 + (V/V_g)^n} \quad (1.38)$$

with $n \gg 1$.

An almost exact description of hysteretic JJs with insulating barriers can be given by the Tunnel Junction Microscopic (TJM) model, developed by Werthamer, Larkin and Ovchinnikov in 1966. In fact, the TJM model gives a complete microscopic description of tunnel JJs within the tunneling Hamiltonian formalism [26]. In essence, the TJM model uses the simple sinusoidal current-phase relationship and the external parallel resistance used in the basic RSJ model are replaced by a more general expression for the current $I(\varphi)$ derived from the microscopic theory, which includes the effects of both quasiparticle and pair transport [17, 27]:

$$I = \frac{\Phi_0}{2\pi} C \frac{\partial^2 \varphi}{\partial t^2} + I(\varphi), \quad (1.39)$$

where the phase φ is related to the voltage by the a.c. Josephson relation (Equation 1.12). In the adiabatic approximation, the voltage $V(t)$ is small and slowly dependent on time compared to the gap frequency $2\Delta/\hbar$ and equation 1.39 thus becomes becomes:

$$I = \frac{\Phi_0}{2\pi} C \frac{\partial^2 \varphi}{\partial t^2} + I_{qp}V(t) + I_{J2}V(t)\cos(\varphi(t)) + I_{J1}V(t)\sin(\varphi(t)). \quad (1.40)$$

The time-dependent total current $I(t)$ that flows in the device is given by the sum of a supercurrent term $I_s(t)$, which includes the terms I_{J1} and I_{J2} , due to the tunneling of Cooper pairs, and a quasiparticle dissipative current $I_{qp}(t)$ [26]. The phase dependent quasiparticle term in equation 1.40 is not simply related to the ohmic resistance above the gap voltage, but to the shape of the subgap branch ($V < V_{gap}$) in the $I(V)$ characteristic and the slope of the $I(V)$ curve near the superconducting branch, i.e. the subgap resistance R_{sg} . The latter is related to the tunneling of quasiparticles and their dissipation [17, 28, 29]. The TJM model is therefore a powerful tool for estimating quasiparticle tunneling. It is therefore essential for the engineering of superconducting circuits. In fact, a large subgap resistance in JJs, exploited in superconducting qubits, provides a reduction of quasiparticle noise, which affects both relaxation and coherence times [30, 31].

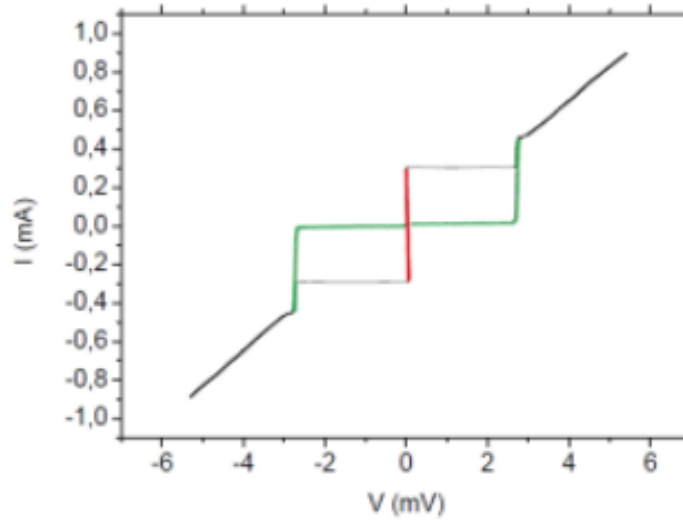


Figure 1.7: I-V characteristic of a conventional JJ Nb-AlO_x-Nb at $T = 4.0K$.

Figure 1.7 shows the $I - V$ characteristic of a Josephson junction Nb-AlO_x-Nb JJ at $T = 4.0K$: the vertical branch represents the passage of the supercurrent through the junction, with a maximum value of I_c (or $-I_c$). When the current flowing through the junction exceeds the critical current value, a finite voltage value is observed at the ends of the junction and the so-called quasi-particle branch (green branch) is observed; the normal state branch is shown in black.

In general, the Josephson junction can be schematised according to the RCSJ (Resistively and Capacitively Shunted Junction) model in an external circuit modeled as an ideal JJ in parallel with a resistance R and a capacitor C [17]. The capacitance C results from the charge accumulation at the interfaces between the superconducting electrodes, while the ohmic element is due to the generation of a dissipative current. The circuit is assumed to be current biased [1].

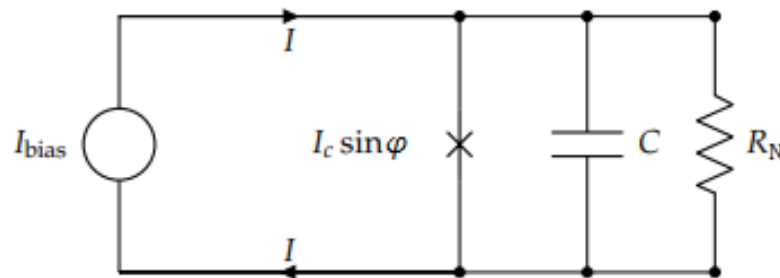


Figure 1.8: Equivalent circuit of a current biased Josephson junction according to the RCSJ model showing a dc I_{bias} source and the parallel of a JJ, its capacitance and resistance.

If a d.c. current I is biasing the JJ, the balance equation is obtained by solving the

Kirchhoff second circuit law for the circuit in the fig. 1.8

$$I = I_c \sin \varphi + I_N + C \frac{dV}{dt} \quad (1.41)$$

Combining formulae (1.12), the voltage across JJ is given by

$$V(t) = \frac{\hbar}{2e} \frac{1}{I_c \cos \varphi} \frac{dI}{dt} \quad (1.42)$$

i.e., a JJ is a non-linear inductor with

$$L_J = \frac{\hbar}{2e} \frac{1}{I_c \cos \varphi} = L_c \frac{1}{\cos \varphi} \quad (1.43)$$

If $I = 0$, the junction can be schematised as an anharmonic LC oscillator with resonant frequency (plasma frequency)

$$\omega_{p0} = \frac{1}{\sqrt{L_c C}} = \sqrt{\frac{2eI_c}{\hbar C}} \quad (1.44)$$

By applying Eq. (1.12) we can explain this balance equation in terms of the phase difference φ as it follows:

$$I = \frac{\hbar}{2e} C \frac{\partial^2 \varphi}{\partial t^2} + \frac{\hbar}{2e} \frac{1}{R_N} \frac{\partial \varphi}{\partial t} + I_c \sin \varphi. \quad (1.45)$$

Multiply by $\hbar/2e$ and defining the Josephson coupling energy, i.e., the energy stored in the junction in the superconducting state, as

$$E_J = \frac{\hbar I_c}{2e} \quad (1.46)$$

we obtain

$$\left(\frac{\hbar}{2e}\right)^2 C \frac{\partial^2 \varphi}{\partial t^2} + \left(\frac{\hbar}{2e}\right)^2 \frac{1}{R_N} \frac{\partial \varphi}{\partial t} + \frac{\partial}{\partial \varphi} \left\{ E_J \left[\cos \varphi - \frac{I}{I_c} \varphi \right] \right\} = 0 \quad (1.47)$$

which can be expressed in terms of a potential energy. Thus, the RCSJ model allows the dynamics of a Josephson junction to be described by the motion of a phase particle moving in a tilted washboard potential $U(\varphi, I)$ [1]:

$$U(\varphi, I) = -E_J \left(\cos \varphi + \frac{I}{I_c} \varphi \right). \quad (1.48)$$

It is immediately evident that equation 1.47 is equivalent to the motion equation of a phase particle of mass $M = \left(\frac{\hbar}{2e}\right)^2 C$ and damping $\eta = \left(\frac{\hbar}{2e}\right)^2 \frac{1}{R}$ moving in the washboard potential $U(\varphi, I)$.

Another mechanical analogue to the motion of a particle of mass M in the tilted washboard potential is the physical pendulum. The equation governing the motion dynamics of a torque-driven pendulum is [23]:

$$D = \Theta \ddot{\theta} + \Gamma \dot{\theta} + mgl \sin \theta. \quad (1.49)$$

In this equation, θ stands for the pendulum angle coordinate, with mass m , positioned at a distance l from the axis of rotation. The term $\Theta = ml^2$ denotes the moment of inertia of all the rotating components of the pendulum, while the term $\Gamma \dot{\theta}$ describes the damping of the pendulum with the damping constant Γ , which is dependent on the angular velocity of the pendulum. Once again, the analogy between equations 1.45 and 1.49 is evident, where high capacity junctions have a high moment of inertia, whereas $1/R_N$ corresponds to dynamic friction.

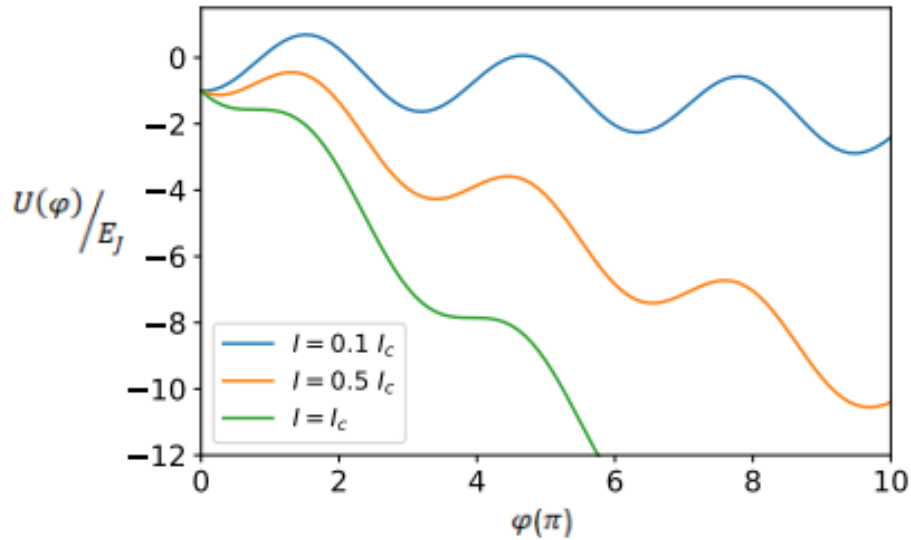


Figure 1.9: Trend of normalised washboard potential $U(\varphi)/E_J$ for different values of normalised polarisation current I/I_c [32].

Washboard potential is a useful tool for visualising the phase dynamics and the I-V curve. Using the tilted washboard potential model (eq. 1.41), the following regimes are distinguished (fig. 1.9):

- for $I < I_c$ the washboard potential is tilted and the phase particle remains in one of the potential wells and oscillates within it until $I = I_c$ is reached, which implies that on average the phase does not change over time and the junction is in the zero voltage state.
- Increasing the bias current for $I \geq I_c$, the particle moves easily along the potential, it follows that the time derivative of the phase is non-zero, thus generating a voltage at the ends of the junction, implying its transition to the resistive state.

- When decreasing the bias current, the particle remains in a non-ohmic resistive state that corresponds to the subgap branch of the I-V curve. We have seen that V does not reach zero until the *retrapping current* I_r is reached.

Hysteresis reflects the inertia of the moving phase particle, which with light damping can overcome a barrier that would have stopped it with heavy damping [15]. If there were no damping, the particle sliding down from a potential maximum would not retract, because the slope ($\propto I$) is reduced to zero, corresponding to $I_r = 0$. With finite damping, I_r is fixed by the current (or the slope of the washboard), at which the energy dissipated in advancing from one washboard maximum to the next equals to the work done by the bias current during the same motion. The two main energy scales are therefore the height of the barrier ($\Delta U(I)$) and the energy dissipated when the system moves within the washboard potential [33].

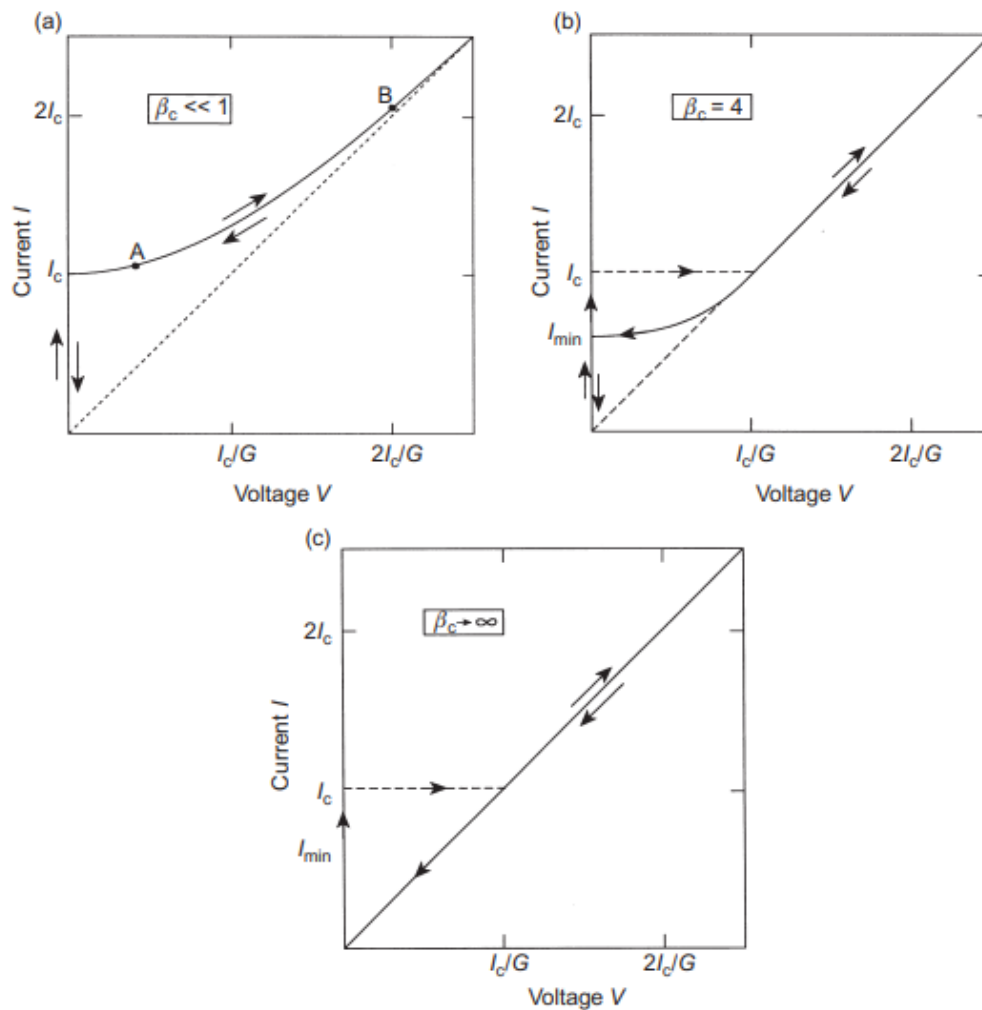


Figure 1.10: Current-voltage characteristics for (a) overdamped junctions ($Q < 1$) (b) moderately damped junctions ($Q > 1$) and (c) underdamped junction ($Q \gg 1$) [17].

It is important to note that the I-V characteristics of a Josephson junction are strongly influenced by the capacitance associated with the junction as it determines the hysteresis of the characteristic itself. The RCSJ model provides another parameter characterising the effect of Josephson junction capacitance: the dimensionless Stewart-McCumber parameter

$$\beta_c = Q^2 \quad (1.50)$$

where Q is the quality or damping factor of the junction that characterizes the strength of friction in the phase particle's motion

$$Q = \omega_{p0}CR_N. \quad (1.51)$$

By using the quality factor Q and normalized time $\tau = \omega_{p0}t$, equation 1.45 is frequently expressed in dimensionless variables. In this way it becomes [34]:

$$\frac{d^2\varphi}{d\tau^2} + \frac{1}{Q} \frac{d\varphi}{d\tau} + \varphi = \frac{I(\varphi)}{I_c}. \quad (1.52)$$

Two operating modes can be distinguished according to the Q values.

If $Q \gg 1$, the system is in the underdamped regime, i.e., in the presence of large capacitances, the device is poorly dissipative, causing hysteresis in the I-V characteristic. In fact, due to the high kinetic energy and low damping, the phase escapes from the well at a certain value of current I_1 , the switching current, and even manages to overcome local maxima. It is only trapped again when the potential has a slope $I_r < I_1$.

If $Q < 1$, the system is said to be overdamped, the capacitance is small, the equation can be solved analytically and a non-hysteretic current-voltage characteristic is obtained. These features are typical of JJ with a metallic barrier. In this case, the particle is trapped at the same value as the switching current, which returns the junction to the zero voltage state, due to its small kinetic energy and the high viscous friction it is subjected to.

When $I < I_c$, ignoring thermal fluctuations, the particle mass is confined to a local minimum where the potential is approximately harmonic for small biases. Thus, the plasma frequency, which for $I = 0$ is ω_{p0} , comes to mean the frequency of small oscillations around a minimum. Instead, at a given bias current I , it is [17, 35, 32]

$$\omega_p = \omega_{p0}(1 - (I/I_c)^2)^{1/4}. \quad (1.53)$$

As the bias current decreases, the particle is retracted into a well, returning to zero voltage when the retrapping current in the weak damping limit is reached [33] [15] [1]:

$$I_r \approx \frac{4I_c}{\pi Q}. \quad (1.54)$$

The RCSJ model is appropriate when the JJs are in the overdamped regime (Fig 1.10 (a)). When the resistance below the gap depends on the voltage, as occurs in hysteretic I(V) curves (Fig 1.10 (c)), the RCSJ model cannot describe the physical processes occurring in the device. An analytical correction to the RCSJ model is represented by the Non-Linear

RCSJ (NLRCSJ) model, in which a non-linear dependence on voltage (typically a power-law V^n , where n is an integer) is introduced in the dissipative element $R_N(V)$ for voltages below the gap, i.e. the subgap region [17, 27]. This model does not provide any further information about the dissipation mechanisms within a JJ.

Using the representation in terms of φ and interpreting the phase as the position variable of the particle, it can happen that the potential to which the particle itself is subjected takes the form of a barrier, and tunneling can take place through it. However, this tunneling does not involve a Cooper pair, but a macroscopic set of particles described by the phase φ . This is known as macroscopic quantum tunneling (MQT). In fact, in the case of underdamped regime and very low temperatures, the phase escapes from the tilted washboard (eq. 1.48) potential well through quantum tunneling, and the system thus passes from the state in which the voltage at the ends of the junction is zero to that in which there is a potential difference, without necessarily exceeding the critical current I_c . In this regime, the escape rate becomes independent of temperature. The passage from the superconducting to the running state of a junction can also happen due to thermal activation (TA) above the potential barrier. In escape processes, the barrier height ΔU of the potential, between a minimum and the subsequent maximum, is [1]:

$$\Delta U(I) = 2E_J \left(\sqrt{1 - \left(\frac{I}{I_c}\right)^2} - \left(\frac{I}{I_c}\right) \arccos \left(\frac{I}{I_c}\right) \right) \quad (1.55)$$

that when the bias approaches I_c gives the cubic potential approximation:

$$\Delta U = \frac{4\sqrt{2}}{3} E_J \left(1 - \frac{I}{I_c}\right)^{\frac{3}{2}}. \quad (1.56)$$

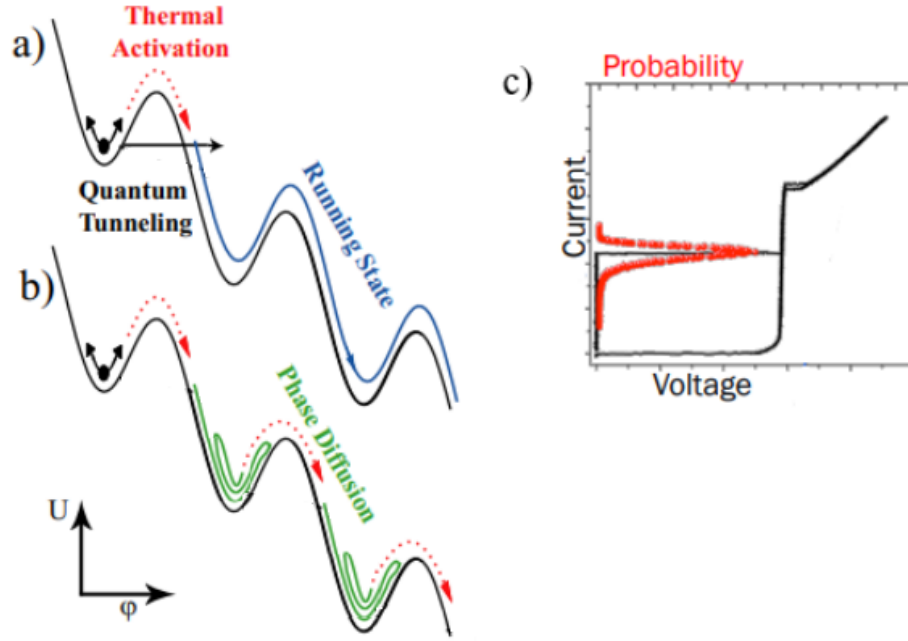


Figure 1.11: Phase dynamics of hysteretic current biased JJ. a) TA and MQT representations in the tilted-washboard potential; the phase ends running down the potential after escape (voltage state); b) diffusive motion of the phase, due to multiple retrappings after escapes; c) The escape is a stochastic phenomenon and one can measure the distribution of the switching currents by repeatedly sweeping the bias current. Taken from [36].

The effect of fluctuations on the phase particle in the potential is to increase or decrease its energy by an amount $k_B T$. Therefore, the condition for which TA dominates is $k_B T \gg \hbar \omega_p$. In this case, the I-V curve of JJs is significantly affected by the presence of thermal fluctuations in the thermal bath and the escape rate is given by the Kramers rate [37]:

$$\Gamma_{TA} = a_{TA} \frac{\omega_p}{2\pi} e^{-\Delta U(I)/k_B T}, \quad (1.57)$$

where $a_{TA} = 4/[(1 + Qk_B T/1.8\Delta U)^{1/2} + 1]^2$ is a damping-dependent prefactor valid for moderately underdamped junctions. Depending on the different damping regimes, the prefactor has different expressions [38].

Due to fluctuations, the escape and retrap of the phase particle are both stochastic processes, governed by specific probability distributions [39]. This is the Switching Current Distributions (SCDs).

Signatures of this regime are asymmetric SCDs with a higher mean value when decreasing temperature, since at low temperatures thermal fluctuations become less relevant, and larger width at higher temperatures [40]. The escape events can be collected in an histogram whose width increases following a universal scaling law $T^{2/3}$.

The MQT regime is characterized by saturation in the width and mean of the SCDs [39]

$$\Gamma_{MQT} = a_{MQT} \frac{\omega_p}{2\pi} \exp \left[-7.2 \frac{\Delta U}{\hbar\omega_p} (1 + 0.87/Q) \right] \quad (1.58)$$

with

$$a_{MQT} = \sqrt{\frac{864\pi\Delta U}{\hbar\omega_p}} \quad (1.59)$$

Due to the stochastic nature of the escape processes, the distribution of switching events is characterised not only by a temperature dependent standard deviation σ , but also by a negative skewness (a measure of the asymmetry in a distribution) of the order of -1, i.e. a tail is generally observed for switching currents $I_{sw} < I_{mean}$, where I_{mean} is the mean value of the SCD [40]. The separation between the thermal and quantum regimes is expressed by the so-called crossover temperature [41]

$$T_{cross} = \frac{\hbar\omega_p}{2\pi k_B} \left[\left(1 + \frac{1}{4Q^2} \right)^{1/2} - \frac{1}{2Q} \right] \quad (1.60)$$

which is simplified to $T_{cross} \approx \hbar\omega_p/2\pi k_B$ in underdamped junctions ($Q \gg 1$), while for overdamped JJs T_{cross} tends to zero, i.e., MQT arises only for low dissipative JJs in the underdamped regime [22]. To express the experimental measurements of the escape rate in a way that is as independent as possible of the parameters of the junction, a parameter, called "escape temperature" (T_{esc}), is traditionally introduced [39]. The rate can therefore be re-parametrized in terms of T_{esc} [42, 43]:

$$\Gamma_{esc} = \frac{\omega_p}{2\pi} \exp \left(-\frac{\Delta U}{k_B T_{esc}} \right). \quad (1.61)$$

Besides the thermal activation and the macroscopic quantum tunneling mechanisms, a third regime can show up in the dynamics of Josephson junctions, the phase diffusion (PD) regime, and is typical of moderately damped junctions ($1 < Q < 5$). This regime is quite different from the well-known case of underdamped systems and appears to be quite common in junctions characterized by low I_c or by higher dissipation, due to the nature of the junction. Due to the increasing use of nanotechnologies in superconducting electronics and the resulting low values of I_c , research on Moderately Damped Regime (MDR) is important for all types of nanoscale junctions. [1]. After phase particle escaping from one barrier, the energy gained by passing from one well to the next one barely exceeds the dissipative losses and the particle eventually gets re-trapped (see Fig. 1.10 b) [44, 45, 46, 47], diffusing to the next wells. At low bias, the process of escape and retrapping can therefore occur several times, producing extensive phase diffusion, until an increase in the slope of the potential due to a change in the bias current increases the velocity of the particle and the junction can switch to the running state. The analytical expression for the retrapping rate from the resistive to the superconducting state, which

thus takes into account the probability that the phase particle is retrapped several times along the washboard [22], has been introduced by Ben-Jacob in Ref. [48]

$$\Gamma_R = \omega_p \frac{I - I_{R0}}{I_c} \exp \left[-E_J Q^2 \frac{(I - I_{R0})^2}{2k_B T I_c} \right] \quad (1.62)$$

where I_{R0} is the retrapping current in absence of thermal fluctuations [49].

The transition temperature, T^* , comes into play, which is defined as the temperature value at which the amplitude σ of the SCD reaches its maximum value. Below T^* , $\Gamma_R \ll \Gamma_{TA}$, and all switching events are solely caused by thermal activation processes. As shown in the figure 1.12a, the corresponding maximum amplitudes of the normalized SCDs decrease with increasing temperature (red curves). When increasing the temperature above T^* , the characteristic collapse of σ with increasing T is observed, as shown in Fig. 1.12b, and the maximum amplitudes of the SCDs increase in this temperature range. In this case, one can observe SCDs becoming more and more symmetric at higher temperatures [37, 40], i.e. the skewness γ increases gradually from -1 to 0.

Such a counterintuitive phenomenon of σ can be elucidated as follows: when retrapping processes are present, a single escape event does not lead to the switching to the voltage state; when a larger number of fluctuation events are required to induce the transition to the running state, the stochasticity in the switching process reduces, leading to sharper distributions of switching currents. This phenomenon also impacts the shape of the SCDs: as in the TA regime the switching histogram shows asymmetry with a distinct tail on the ascending side of the distribution, in the PD regime, the histograms exhibit more symmetry due to multiple retrapping that halts the switching at lower values of the bias current. This results in a gradual reduction of the tail on the ascending side of the SCD [1].

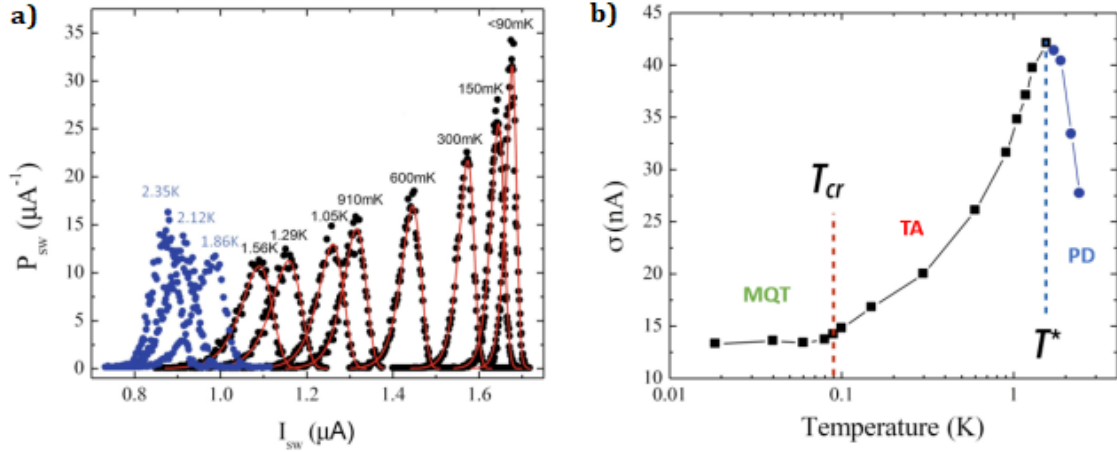


Figure 1.12: a) Measurements of SCDs as a function of temperature in the moderately damped regime. The red curves indicate fits of the SCDs in the TA regime, while the blue points indicate measured histograms in the PD regime. b) Temperature dependence of the standard deviation σ of the switching distributions. Three distinct regimes were identified: MQT for $T < T_{cr}$, TA for $T_{cr} < T < T^*$ and PD for $T > T^*$, respectively [1].

In order to determine the escape rate, a certain sample of switching events is collected at a fixed temperature and the probability distribution is given by the following equation:

$$P(I) = \frac{\Gamma_T(I, t)}{dI/dt} \exp\left(-\int_0^I \frac{\Gamma_T(I, t)}{dI/dt} dI\right) \quad (1.63)$$

where dI/dt is the current ramp rate. The resulting distribution of the switching probability $P(I)$ is used to compute the escape rate out of the zero-voltage state as a function of the bias current [35, 49]:

$$\Gamma(I) = \frac{1}{\Delta I} \frac{dI}{dt} \ln\left(\frac{\sum_{i \geq I} P(i)}{\sum_{i \geq I + \Delta I} P(i)}\right) \quad (1.64)$$

where ΔI is the channel width of the analog-to-digital converter.

In the quantum description of a Josephson junction, the phase φ and the Cooper pair number N are the two fundamental quantum operators. In the absence of dissipation, the Hamiltonian describing the behaviour of a JJ is a function of the phase difference φ and of the charge Q transferred between the electrodes [15]:

$$H(\varphi, Q) = \frac{Q^2}{2C} - E_J \cos \varphi. \quad (1.65)$$

The first term is the capacitive charging energy and the second the Josephson energy. The operators for charge and phase satisfy the commutation relation $[\varphi, Q] = i2e$, i.e.,

they are bound by the Heisenberg uncertainty relation. Depending on which of the two contributions, kinetic or potential, is dominant, two situations can arise. When $E_J \gg E_c$, φ is well defined while Q has very large fluctuations. Therefore, the particle itself can be thought of as confined in one of the wells with a definite value of φ . On the other hand, when $E_J \ll E_c$, Q is well defined, while the phase is subject to large fluctuations. In this situation the junction is known as a Cooper-pair box [50].

1.4 Ferro-Transmon Qubit prospective

The Josephson junction is the element that provides the nonlinearity needed to turn a superconducting circuit into a qubit. Superconducting quantum circuits have almost exclusively relied on Al/AlO_x/Al tunnel Superconductor/Insulator/Superconductor (SIS) JJs [2, 51]. However, many exciting phenomena and functionalities can be accessed by exploiting unconventional superconducting systems [8]. In fact, novel hybrid paradigms have recently been introduced, demonstrating that devices integrating superconductors and exotic barriers can provide additional qubit frequency knobs [52]. As an example, in the specific case of tunable transmon qubits [53], which typically use external flux-fields to change the qubit frequency, hybrid superconductor-semiconductor structures [54, 55] have been used to enable voltage-tunable transmons (gatemons), in order to provide an alternative tuning of the qubit frequency without introducing flux-noise [56]. Among unconventional Josephson devices, a potential advantage can arise from the combination of Superconductors with Ferromagnets (F). The progress in the realisation of Magnetic Josephson Junctions (MJJs) with a wide variety of materials, geometries and structures has created a unique playground for exploring the interplay between superconductivity and ferromagnetism. Progress in the coupling of both ferromagnetic layers with insulating barriers inside the JJ (SIsFS or SIFS JJs) [57] and the ability to exploit intrinsically insulating ferromagnetic materials (SIFS JJs) [58] allow to engineer ferromagnetic JJs characterised by high values of the quality factors and access to the MQT regime [9, 59]. These tunnel-SFS JJs provide additional functionality not only in classical superconducting circuits, but also in quantum architectures [8]. The new plan aims to assess a novel idea for qubit design that employs a Ferromagnetic Josephson junction (MJJ) within the transmon architecture, allowing for a device called the *Ferro-Transmon* qubit.

–2–

Magnetic Josephson junctions

This chapter will explore the properties and functionalities of Magnetic Josephson Junctions (MJJs). The first part of this chapter gives a brief introduction to ferromagnetism, focusing on how it affects superconductivity and overall device behaviour. The second half will focus on specific types of MJJs, Superconductor-Ferromagnet-Superconductor (SFS) and Superconductor-Insulator-Superconductor-Ferromagnet-Superconductor (SISFS) JJs. The latter are already widely used in superconducting electronics as blocks for cryogenic RAM memories [60] in Single Flux Quantum (SFQ) logic. In addition, in recent years there has been an increasing interest in aluminium based SISFS MJJs for possible qubit application [8].

2.1 Ferromagnetic materials

As superconductors, ferromagnetic materials are characterised by spontaneously broken symmetry below a critical temperature, known as the Curie temperature T_{Curie} . At $T \geq T_{Curie}$, the ground state is symmetric, i.e., all magnetic moments are randomly oriented in the bulk material (disordered paramagnetic phase). At $T < T_{Curie}$, however, rotational symmetry is broken and the spins are aligned in the same direction (ferromagnetic state). It follows that ferromagnetic materials can exhibit intense spontaneous magnetization, i.e. they can be magnetised even in the absence of an external field. The orienting action of the exchange energy is counteracted by thermal agitation: as shown in Figure 2.1, the spontaneous magnetisation M_s decreases with increasing temperature until it is cancelled out at the Curie temperature.

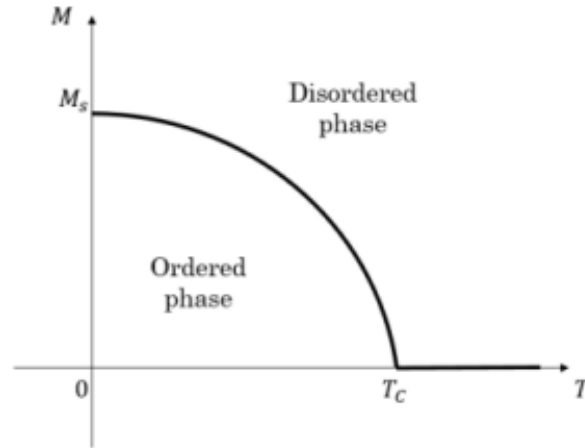


Figure 2.1: Spontaneous magnetization trend as a function of temperature [61].

In Weiss mean field theory, the order parameter for this phase transition is the magnetization

$$\vec{M} = \mu_0 \vec{B} - \vec{H}. \quad (2.1)$$

A ferromagnet is perfectly ordered at $T = 0$ but at non-zero temperature this is disrupted by magnons. A magnon is a quantized spin wave [62]. It has the self consistent expression

$$M(T) = \frac{N}{V} \mu_B \tanh \left(\frac{1}{k_B T} \frac{M V Z}{N \mu_B} \frac{J}{2} \right) \quad (2.2)$$

where N is the total spin number, V is the ferromagnet volume, Z is the coordination number, μ_B is the Bohr magneton and J is the coupling constant, which is the same for all spin pairs [18].

The dependence of the magnetisation on temperature, expressed by this formula, makes it clear that at progressively lower cryogenic temperatures, saturation can be reached with a smaller value of the external magnetic field.

2.1.1 Domains and magnetization processes

An iron, cobalt or nickel crystal, in its demagnetized state, is divided into a number of small regions, called *Weiss domains* [63]. Each domain is spontaneously magnetized with its maximum saturation value M_s , but the magnetization directions of the different domains are such that the sample as a whole has zero net magnetization [64]. The direction of magnetization in each domain in the absence of an external field is not random, but the crystalline electric field gives a preferred direction along which the spin moments must be oriented. The directions taken by the magnetization vector in the domains of a demagnetized sample are called directions of easy magnetization. What happens is that when an external magnetic field tries to orient the spin of an electron, due to the coupling between the spin and the orbital motion of the electron (spin-orbit interaction), the orbit of the electron would also tend to be oriented. But the latter is fixed by the crystalline field

and thus resists the attempt to rotate the spin axis. Since an external field must perform work to turn the direction of magnetization away from that of easy magnetization, this means that if, in a crystal, the vector M_S points in a direction of non-easy magnetization, the crystal embeds a certain amount of energy, known as magnetocrystalline anisotropy energy (E_{anis}). For a uniaxial anisotropy, the energy density can be written as [65]:

$$E_{anis} = K_0 + K_1 \sin^2 \theta + K_2 \sin^4 \theta + \dots \quad (2.3)$$

where θ is the angle between the M_S vector and the direction of easy magnetization. When K_1 and K_2 are both positive, the energy E_{anis} is minimum for $\theta = 0$, and the axis corresponds to an easy axis of magnetization. When K_1 and K_2 are both negative, the minimum value of E_{anis} occurs at $\theta = 90^\circ$. This creates an easy plane of magnetization, which is the basal plane of a hexagonal material, lying perpendicular to the axis [65]. The existence of magnetic domains is due to the minimization of magnetic energy. In fact, the energy is the sum of several terms, in addition to the magnetocrystalline anisotropy energy

$$E = E_{ex} + E_{anis} + E_{dip} + E_{Zeeman}. \quad (2.4)$$

The *exchange energy* forms an important part of the total energy of many molecules and of the covalent bond in many solids. Heisenberg showed that it also plays a decisive role in ferromagnetism. If two atoms i and j have spin angular momentum \vec{S}_i and \vec{S}_j , respectively, then the exchange energy between them is given by

$$E_{ex} = -2J_{ex}\vec{S}_i \cdot \vec{S}_j \cos \phi \quad (2.5)$$

where J_{ex} is a particular integral, called the *exchange integral*, which occurs in the calculation of the exchange effect, and ϕ is the angle between the spins. If J_{ex} is positive, E_{ex} is a minimum when the spins are parallel ($\cos \phi = 1$) and a maximum when they are antiparallel ($\cos \phi = -1$). If J_{ex} is negative, the lowest energy state results from antiparallel spins [65].

Because $\nabla \cdot \vec{H} = -\nabla \cdot \vec{M}$ at the edges of a sample, the magnetic field diverges creating demagnetising fields that fill space and cost $B^2/2\mu_0$ Joules of energy per cubic metre. The energy associated with the demagnetizing field is called the *demagnetization energy*, *magnetostatic energy* or *dipolar energy* (E_{dip}). It takes the value

$$E_{dip} = -\frac{\mu_0}{2} \int_V \vec{M} \cdot \vec{H}_d d\tau, \quad (2.6)$$

where H_d is the demagnetizing field and the integral is taken over the volume of the sample. For an ellipsoidally shaped sample magnetized along one of its principal axes, this energy reduces to

$$E_{dip} = \frac{\mu_0}{2} N M^2 V \quad (2.7)$$

where N_d is the demagnetizing factor and V is the sample volume [65]. The value of N_d depends mainly on the shape of the body, and has a single calculable value only

for ellipsoid. It is minimized by keeping flux inside the ferromagnet: for example, in ferromagnetic thin films, it is minimized by keeping the magnetization in-plane [66]. Finally, *Zeeman energy*, or the external field energy, is the potential energy of a magnetised body in an external magnetic field. In SI units, it is given by

$$E_{Zeeman} = -\mu_0 \int_V \vec{M} \cdot \vec{H} dV, \quad (2.8)$$

where the integral is done over the volume of the body V .

The boundary separating one domain from the adjacent domain is called the domain wall. Because of the energy involved, the boundary between two adjacent domains can be sharp (the wall has a thickness tending to zero) or gradual (the wall has a finite thickness). In the latter case, the domain wall is more extensive and the energy cost of exchange to form it is less than when the boundary is sharp. In reality, however, the wall always has a thickness other than zero and its thickness depends on the competition between the exchange energy and that of the anisotropy. Two types of domain walls can be distinguished (Figure 2.2). Within Bloch walls, spin rotation takes place outside the plane of the domains, whereas within Néel walls it takes place in the plane.

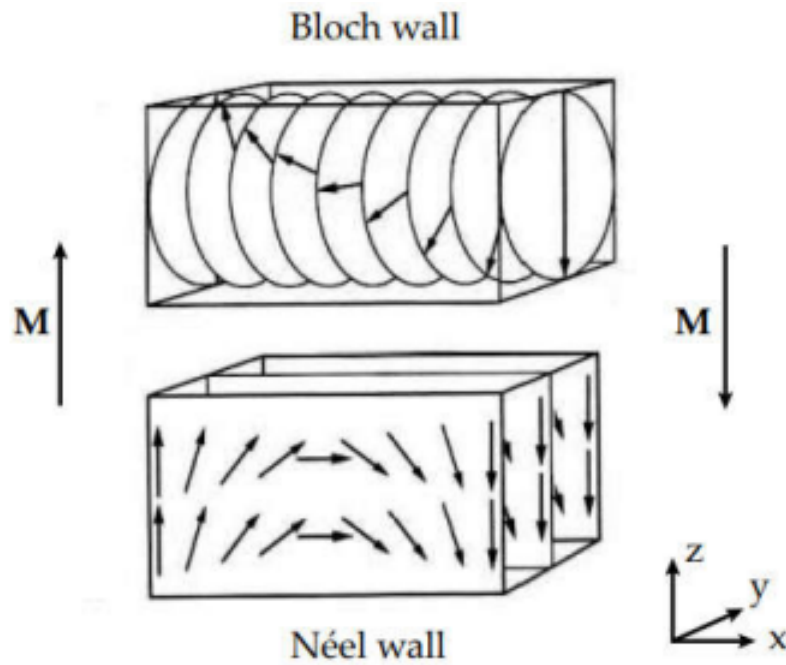


Figure 2.2: Rotation of the magnetization vector \vec{M} in Bloch and Néel walls.

While the exchange energy tries to make the wall as wide as possible to keep the angle ϕ between adjacent spins as small as possible, the anisotropy energy tries to make the wall thin in order to make the spin pointing in an unfavourable direction. As with any interface, Bloch walls are associated with an energy per unit area: the crystal cannot be

divided into an indefinite number of domains so as not to raise the energy of the system too high.

The position of the walls is related to the spatial distribution of lattice defects. If the crystal were an ideal crystal, each position would be energetically equivalent, and therefore the walls could occupy any position. The presence of lattice defects undermines this state of affairs: the domain walls position themselves at the defects to reduce the energy of the crystal. It follows that the application of an increasing magnetic field over time will not lead to a continuous displacement of the walls, but they will move in jerks, carrying themselves from one lattice defect to another, and then remain anchored in the new position until the magnetic field is increased by a sufficient amount to cause them to overcome the obstacle. This is the physical origin of magnetic hysteresis. In particular, it is expected that materials rich in defects will be characterised by rather wide hysteresis curves, while materials poor in defects will give rise to narrower hysteresis curves [64]. The hysteresis loop describes the evolution of the magnetization M as a function of the applied external field H . The shape of the hysteresis loop of a ferromagnetic material depends on the structure and thus on the history (thermal, mechanical, etc.) of the sample. Consider the case of a material with uniaxial anisotropy, where each crystalline grain has its own axis of easy magnetization and the grains are randomly oriented with respect to each other. In the figure 2.3, the arrangement of M_s vectors in domains is represented by a set of vectors drawn from a common origin.

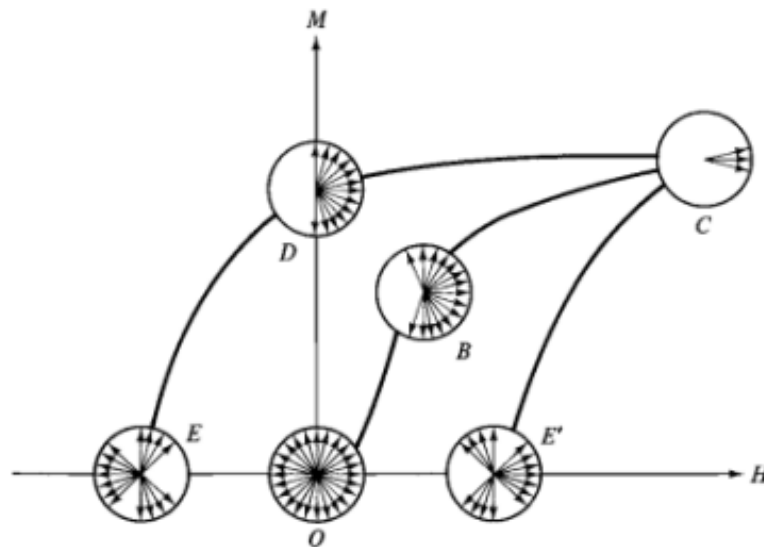


Figure 2.3: Distribution of domains for different magnetization states [64].

When an external field is applied to a demagnetized sample, M increases as H increases according to the curve of first magnetization (curve OC in Figure 2.3). Initially, the domains magnetized in the opposite direction to the positive field are first eliminated by a wall movement of 180° , resulting in the distribution shown in B. Once this point is reached, a further increase in the field rotates the spins within the domains to the saturated state

shown in C. Since the contribution of the magnetocrystalline anisotropy energy must be overcome, a large increase in the H field produces a relatively small increase in M . When all domains have aligned in the direction of the field, the maximum value of the magnetization is reached, called the saturation magnetization M_S , and the external field for which the saturation begins is called the *saturation field* H_S . When the external field is reduced, $M(H)$ describes a curve different from the initial one; in particular, at zero field, the magnetization takes on a finite one, since removing the field, the M_S vectors of the domains do not recover the initial direction, but fall back in the direction of easy magnetization closest to the direction of the H field imposed before. This magnetization value is called *residual magnetization* M_r . We then arrive at point D, where the domain vectors are evenly distributed over half the sphere [64, 67].

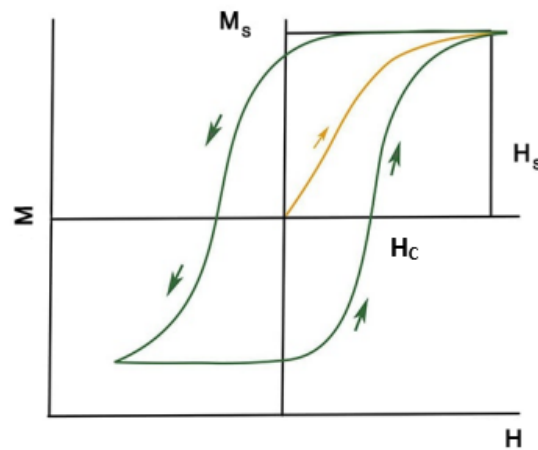


Figure 2.4: Hysteresis loop of a ferromagnetic material and characteristic parameters. The yellow line is the first magnetization curve (also called the virgin curve). The coercive field H_C is the field required to bring the material back to zero magnetization. M_S is the saturation magnetization and the field value at which the magnetization reaches the saturation value is called the saturation field H_S .

By applying a field in the negative direction to a sample in the remanence state, the magnetization domains rotating in the $+H$ direction are reversed, bringing the sample to the zero magnetization state, which is point E in the figure 2.3, where the *coercive field* $-H_c$ is reached. The latter is defined as the value of the field at which the sample demagnetises after being brought to saturation. Further reduction of the magnetic field below $-H_S$ causes the magnetization to saturate at $-M_S$. If the field is increased again, the magnetisation increases accordingly until it reaches zero at H_c (figure 2.4). By further increasing the applied field, M increases to saturation M_S .

2.2 Proximity effect at S/N interface

This section discusses transport through an SNS JJ. The understanding of this key structure is essential for the study of the conduction mechanism through an S/F interface, where F is typically a ferromagnetic metal barrier. When a superconductor S is in close contact with a normal metal N, the Cooper pairs can penetrate the normal metal N for some distance from the interface. As a result, superconducting properties can be induced in N: this phenomenon is known as the *proximity effect*. The proximity effect can be described in the framework of the phenomenological theory of Ginzburg-Landau (GL): the superconducting transition is a second-order phase transition that can be described by an order parameter that depends only on spatial variables [68]. This parameter Ψ takes its maximum value 1 well inside the superconductor and vanishes well inside the metal normal. At the S/N interface, a continuous change in the order parameter between the two phases is observed along the distance x from the interface. By imposing the above boundary conditions, we solve the linearized 1-D GL equation

$$-\xi_N^2 \frac{d^2\psi}{dz^2} + \psi = 0 \quad (2.9)$$

from which we obtain the following solution for the order parameter

$$\psi = \psi_0 \exp\left(-\frac{x}{\xi_N(T)}\right). \quad (2.10)$$

It is deduced that the order parameter decreases exponentially within the metal over a distance of the order of the *coherence length* or *decay length* ξ_N (Fig. 2.7 (a))[69]. For an S/N interface, this characteristic length can have two different expressions depending on how large ξ_N is compared to the mean free path l_N of the normal metal. If $l_N > \xi_N$, the corresponding JJ is in the *clean limit* and the coherence length is [70]:

$$\xi_{N,c} = \frac{\hbar v_F}{2\pi k_B T} \quad (2.11)$$

where v_F is the Fermi velocity and k_B is the Boltzmann constant. If $l_N < \xi_N$ instead, the JJ is in the *dirty limit* and the coherence length is:

$$\xi_{N,d} = \sqrt{\frac{\hbar D_N}{2\pi k_B T}} \quad (2.12)$$

where D_N is the diffusion coefficient. The mechanism by which the transfer of Cooper pairs from the superconductor to the normal metal and vice versa occurs is called *Andreev reflection* and is shown schematically in Figure 2.5. An electron from the normal metal with an energy ϵ lower than the superconducting energy gap Δ reaches the S/N interface and, instead of being reflected, pulls an electron of energy $-\epsilon$ with opposite momentum and spin from the valence band into the superconductor, forming a

Cooper pair. This second electron is taken from the valence band, leaving a hole. This hole travels back along the path of the original incoming electron because it has the opposite momentum. The reverse process can also take place: the particle that reaches the interface is a valence band gap (of energy $-\epsilon$) which, on arrival at the interface, breaks a Cooper pair of the condensate. One of the two electrons in the pair will occupy the hole, while the other electron will occupy an excited state in the conduction band and travels back along the path of the original incoming hole. The net result of an Andreev reflection is therefore a charge transfer of $-2e$ from N to S (Fig. 2.5 a).

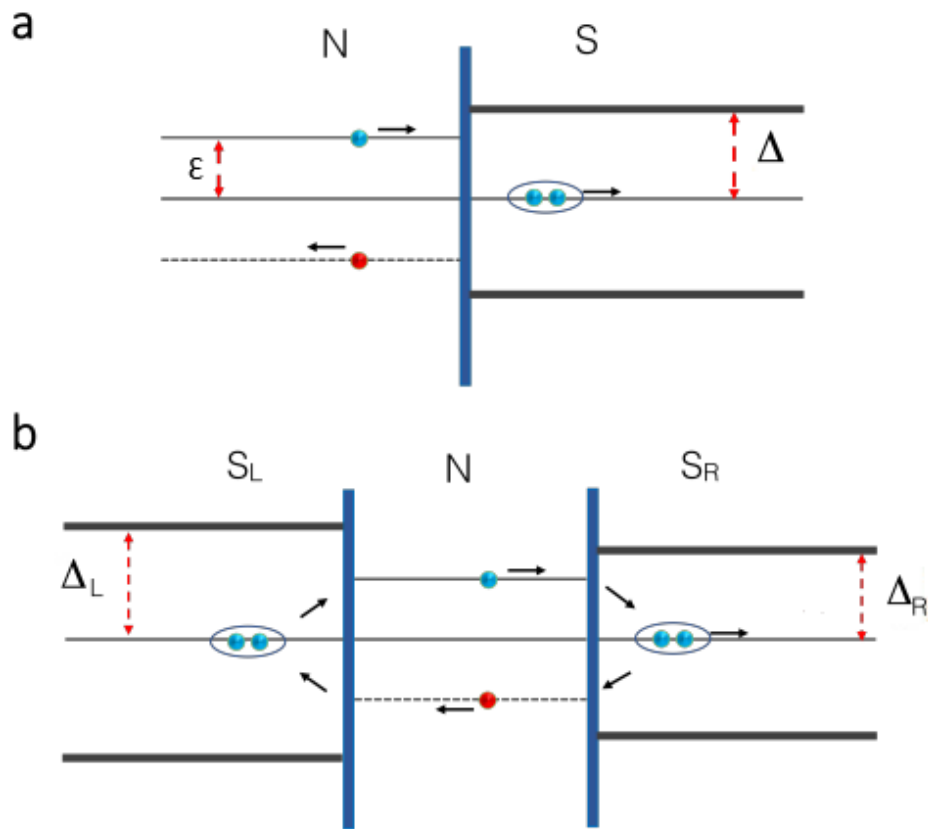


Figure 2.5: Andreev reflection (a) at the S/N interface and (b) in a SNS JJ [1].

There is also Andreev reflection at the SNS interface. An electron approaching one of the interfaces is converted into a hole moving in the opposite direction, creating a Cooper pair in a superconductor. This hole is then reflected at the second interface and converted back into an electron, leading to the destruction of a Cooper pair (Fig. 2.5 b).

The temperature dependence of the critical current for various small weak links in SNS JJs, theoretically predicted by Likharev, as a function of the ratio L/ξ_N [69], where L is the length of the barrier is shown in the figure 2.6. For low values of L/ξ_N , the $I_c(T)$ curve shows a down-ward concavity and is similar to that expected for tunnel JJs.

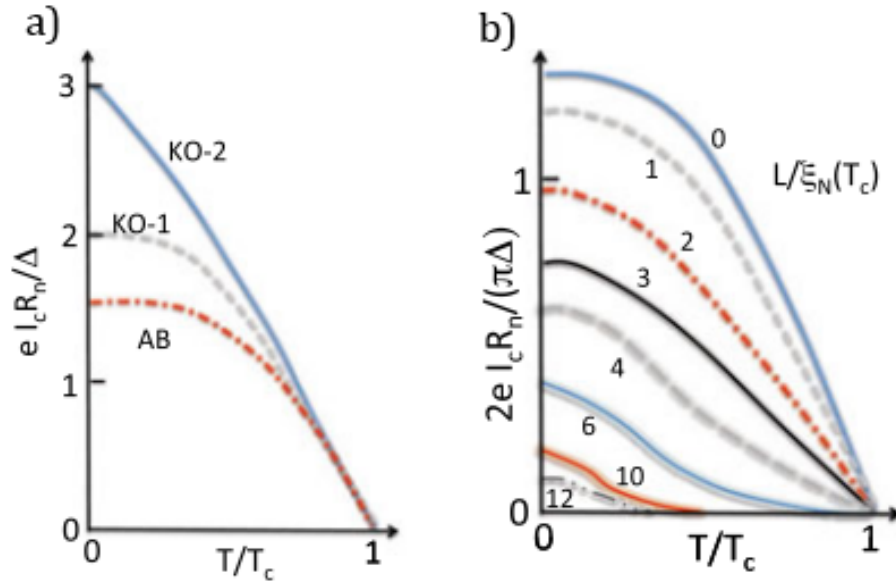


Figure 2.6: (a) $I_c R_N(T)$ in the AB (dashed red line), KO1 (grey dashed line) and KO2 (blue continuous line) limits respectively. (b) $I_c R_N$ is reported in units normalized to the gap value Δ as a function of the temperature T , for different values of the ratio between the barrier length L and ξ_N [69, 1].

In point contacts in the dirty (KO1) and clean limits, the values of I_c at $T = 0$ K are higher than AB value. The KO-1 theory attains its maximum as $T \rightarrow 0$ which is 32% greater than the maximum value of $I_c R_N$ for tunnel junctions. At the lowest T there is a saturation of I_c , while at high T (for $T \approx T_c$) I_c has a characteristic exponential dependence for high values of the ratio L/ξ_N [69, 71, 72]. These two regions are connected at intermediate T by a curve with upward concavity. The tail of the exponential growth and the width of the intermediate region depend essentially on L/ξ_N [17, 69, 71].

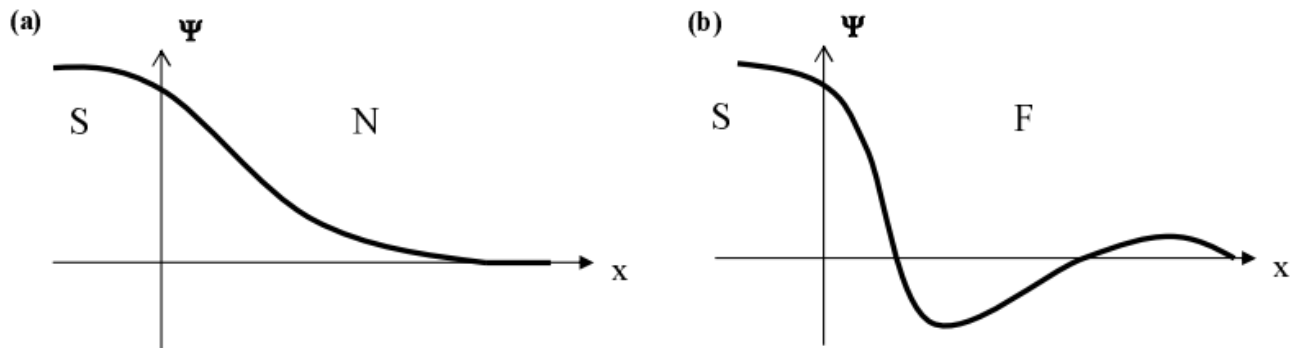


Figure 2.7: Superconducting order parameter at a) S/N interface and b) S/F interface. The exchange field causes an oscillation of the order parameter [73].

2.3 Proximity effect at S/F interface

According to BCS theory, conventional Cooper pairs, which are present in almost all known superconductors, have two electrons with opposite spin and momentum $(+\vec{k}, -\vec{k})$ [74], in ferromagnetic materials, instead, the exchange field promotes the alignment of the electron spins in the same direction. It is clear that these are two states of matter characterized by antagonistic long-range orders. Since the energy gain of ferromagnetic (hundreds of meV or a few eV) is much larger than that of superconductors (a few meV), one would expect a strong suppression of superconductivity in S/F (superconductor/ferromagnet) bilayers. Specifically, in a hybrid S/F junction, the proximity effect can still occur even though the Andreev reflection mechanism is partially suppressed. Since in the metal F the density of states at the Fermi level for spin-up electrons is different from that for spin-down electrons, an electron in the majority spin band has a lower probability of causing the retroreflection of the gap in the minority spin band. Andreev reflection suppression becomes more important as the spin polarization of the metal increases [73, 75]. In addition, the induced electron-hole pair undergoes exchange splitting of the spin bands in the ferromagnet.

It was predicted by Larkin and Ovchinnikov [76] and by Fulde and Ferrel [77] that pairing still can occur when the electron energies and momenta at the Fermi energy are different for the two spin directions, for instance as the result of an exchange field in magnetic superconductors [74]. In fact, when the normal metal is replaced by a ferromagnet, the effects of a non-zero spin polarization and the exchange energy E_{ex} have to be taken into account. The resulting 'FFLO'-state is qualitatively different from the zero-momentum state. In the framework of this model, a non-uniform superconducting state appears with a sinusoidal modulation of the superconducting parameter with a non-zero wave vector on the scale of the superconducting coherence length ξ_S [78]. The spatial modulation of the order parameter is due to the Zeeman splitting of electronic levels in the presence of the exchange field. The spatial variation of the superconducting order parameter in the ferromagnet arises as a response of the Cooper pair to the energy difference between the two spin directions in ferromagnet [74]. In absence of the exchange term a Cooper pair comprises two electrons with opposite spins and momenta. When exchange field is added, the spin up electron (with the spin orientation along the exchange field) decreases its potential energy by E_{ex} and increases its kinetic energy by the same amount, while the down spin electron increases its potential energy and a decrease of the kinetic energy of the same amount E_{ex} . In the result the Cooper pair acquires a center of mass momentum $2\delta k = \frac{\mu_B H_{ex}}{v_F}$, which implies the modulation of the order parameter with the period $\pi v_F / E_{ex}$. The direction of the modulation wave vector must be perpendicular to the interface, because only this orientation is compatible with the uniform order parameter in the superconductor [78]. The FFLO state was never observed in bulk material, but it can be induced in a ferromagnet (F) sandwiched between two superconductors (S). Such an SFS junction can yield a phase shift of π between the superconducting banks [79, 80, 74]. Taking into account all spin states, the order parameter ψ induced in the F-layer, in GL

theory, has the form [81]:

$$\psi = \psi_0 \exp\left(-\frac{x}{\xi_{F1}}\right) \cos\left(\frac{x}{\xi_{F2}}\right) \quad (2.13)$$

where $\xi_{F1} \propto \left(\sqrt{1 + \frac{T-T_{ci}}{T_{ci}-T_{cu}} - 1}\right)^{-1/2}$ and $\xi_{F2} \propto \left(\sqrt{1 + \frac{T-T_{ci}}{T_{ci}-T_{cu}} + 1}\right)^{-1/2}$. T_{cu} is the transition temperature of the system into the uniform superconducting state and T_{ci} the transition temperature of the system into the non-uniform superconducting state [73]. The decay of the order parameter in the F-layer is then accompanied by its oscillation, which is a characteristic feature of the proximity effect in SF systems (Fig. 2.7b).

In real ferromagnets, the exchange field is very large compared with superconducting temperature and energy scales, so the gradients of the superconducting order parameter variations are large too, and can not be treated in the framework of the generalized Ginzburg-Landau functional. To describe the relevant experimental situation we need to use a microscopical approach. The most convenient scheme to do this is the use of the Bogoliubov-de Gennes equations or the Green's functions in the framework of the quasiclassical Eilenberger or Usadel equations [73]. In the diffusive (dirty) limit, the coherence lengths $\xi_{F1(2)}$ are the real and the imaginary part of the complex ferromagnetic coherence length ξ_F ,

$$\xi_F = \sqrt{\frac{\hbar D_F}{2(\pi k_B T + iE_{ex})}}, \quad (2.14)$$

where D_F is the diffusion constant of the ferromagnet [74, 71]. Instead, in the ballistic (clean) limit, the S/F transport is governed by two coherence lengths: ξ_{F1} and ξ_{F2} . The former corresponds to the normal metal coherence length

$$\xi_{F1} = \frac{\hbar v_F}{2\pi k_B T}, \quad (2.15)$$

where the fundamental energy scale is the Boltzman thermal energy. ξ_{F2} , instead, depends on the exchange field in the ferromagnet E_{ex} ,

$$\xi_{F2} = \frac{\hbar v_F}{2\pi E_{ex}}, \quad (2.16)$$

with v_F the Fermi velocity in the ferromagnet [22].

The damped oscillatory behavior of the superconducting order parameter in ferromagnets may produce the commensurability effects between the period of the order parameter oscillation (which is of the order of ξ_F) and the thickness of a F layer. Indeed, for a F layer thickness smaller than ξ_F , the pair wave function in the F layer changes a little and the superconducting order parameter in the adjacent S layers must be the same. In this case the phase difference between the superconducting order parameters in the S layers is absent and the junction is in the 0 phase. On the other hand, if the F layer thickness becomes of the order of ξ_F , the pair wave function may go trough zero at the center of F

layer providing the state with the opposite sign of the superconducting order parameter in the adjacent S layers, in the way to obtain a π phase. A π junction is a Josephson junction with a negative critical current I_c . Thus, the current I_J through a π junction for a given superconducting phase difference across the junction φ , assuming a purely sinusoidal form for the CPR, is given by $I_J(\varphi) = |I_c|\sin\varphi = |I_c|\sin(\varphi + \pi)$, in terms of the magnitude of the critical current $|I_c|$. The minimum energy state of an isolated π junction corresponds to a phase shift of π across the junction, [82] in contrast to an ordinary Josephson junction, or 0 - junction, for which the minimum energy is at zero phase difference [81].

The increase of the thickness of the F layers may provoke the subsequent transitions from 0 - to π -phases, what result in a very special dependence of the critical temperature on the F layer thickness. For the S/F bilayers, the transitions between 0 and π -phases are impossible [73]. Rather, the 0 - π phase transition can manifest itself in a non-monotonic thickness dependence of both the superconducting transition temperature T_c [74, 81, 83] and the critical current I_c in SFS JJs [84, 85, 86, 87].

Usually, the single harmonic current-phase relation (CPR) is adequate for the description of the JJ properties; high order harmonic terms can be omitted. However in the vicinity of the 0- π transition, where the critical current for the first harmonic vanishes, higher-order harmonics in the CPR in Eq. 1.12 become important [88, 89, 90]. Especially at low-temperatures, the presence of higher harmonics at the 0- π transition prevents a complete suppression of the critical current [91, 90, 92]. This influences also the phase-dynamics, the Shapiro steps amplitude and the Fraunhofer pattern periodicity [93, 71, 94, 95, 88, 96], since the washboard potential will change accordingly with the CPR [74, 71, 88]. Indeed, in presence of a second harmonic CPR the washboard potential becomes [88]

$$U(\varphi) = \frac{\hbar I_c}{2e} \left[\frac{I}{I_c} \varphi + (1 - \cos\varphi) + \frac{g}{2}(1 - \cos 2\varphi) \right] \quad (2.17)$$

where g is the ratio between the first and second harmonic critical currents. In this case, the periodic potential has two minima at different φ , depending on the sign of g (fig. 2.8): when the second harmonic is positive (red lines in fig. 2.8), the washboard potential has two non degenerate minima at $\varphi = 0$ and $\varphi = \pi$, so the junction can be in the 0-phase or in the π -phase, with different critical currents, depending on damping conditions and other parameters [59, 88]. If the second harmonic contribution is negative (blue lines in fig. 2.8), the junction has two degenerate minima at $\varphi = \pm\phi_0$, with two different critical currents. This is the case for φ -junctions [88, 97]. One method to realise such junctions is to make ferromagnetic barriers which have a thickness L_0 for one portion of the junction barrier and a thickness L_π for the other portion. By doing this, an extra degree of freedom is obtained, allowing for the ground state of the junction to be set at an intermediate value between 0 and π . This results in an added degree of freedom for adjusting the current phase relationship.

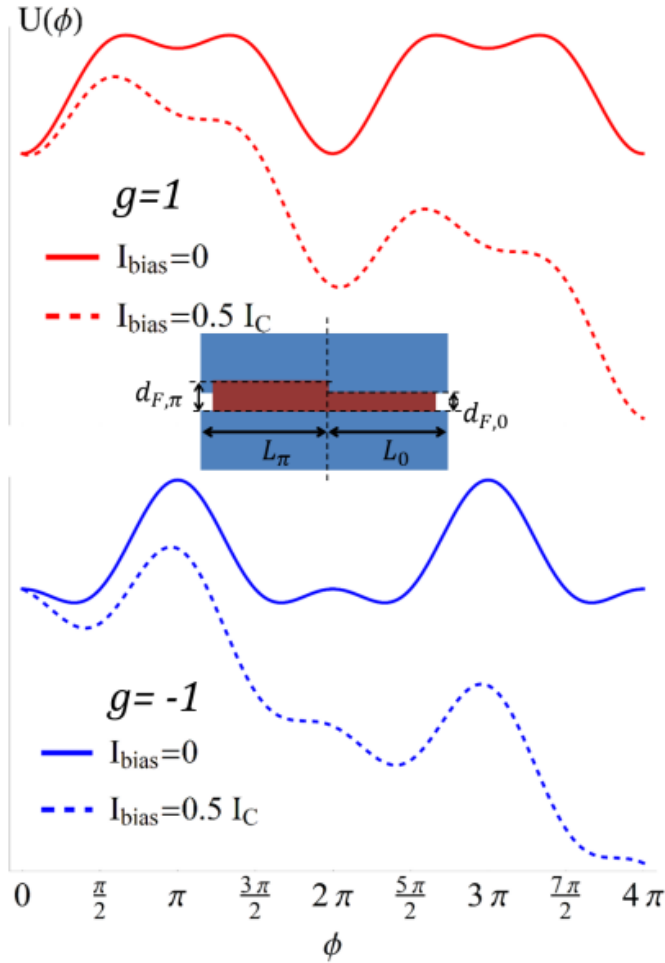


Figure 2.8: Washboard potential for $g = \pm 1$, in absence and in presence of external bias current [1].

2.3.1 SFS junction in magnetic field

As already stated in Section 2.1, the characteristic features of the ferromagnetic materials are domain structures and magnetic hysteresis, i.e., a multivalued dependence of the magnetic induction \vec{B} and magnetization \vec{M} on the external magnetic field H [98]. Indeed, considering that in a ferromagnet the magnetic induction field B is

$$\vec{B} = \mu_0(1 + \chi)\vec{H} \quad (2.18)$$

where $\vec{M}(H) = \chi\vec{H}$ is the hysteretic magnetization of the ferromagnet, Eq. 1.26 reads as

$$I_c(H) = I_c(0) \left| \frac{\sin\left(\pi \frac{\Phi(H) \pm \Phi_F(H)}{\Phi_0}\right)}{\left(\pi \frac{\Phi(H) \pm \Phi_F(H)}{\Phi_0}\right)} \right|. \quad (2.19)$$

where $\Phi(H)$ is the flux generated by the external field and Φ_F is the magnetic flux due to the layer magnetization M_F . In fact, it is well known that in samples containing an F-barrier, to evaluate the total magnetic flux through the junction Φ , the F magnetisation flux Φ_F below the Curie temperature T_{Curie} , which is given by $\Phi_F = \mu_0 M_F L d_F$, where L is the cross-sectional width, has to be considered [98]. Therefore, the total magnetic flux through the junction is

$$\Phi = \mu_0 H L d_m + \mu_0 M_F L d_F, \quad (2.20)$$

where the thickness of the material penetrated by the applied field is $d_m = 2\lambda_L + d_F$ [99]. It is clear from equation 2.20 that the flux due to the magnetization of the F layer is added to that generated by the external field. By subtracting the contribution of the external magnetic field, it is possible to obtain the flux due to the magnetization of the ferromagnet: this gives the $M(H)$ dependence. Because of these properties, SFS JJs are suitable as RAM (Random Access Memories) memories [100].

If a magnetic field is applied to a rectangular junction, its dependence of I_c as a function of H is represented by the Fraunhofer pattern (sec. 1.3.2) [11, 98]. The main difference between the $I_c(H)$ measured for a tunnel junction and a SFS JJ is the hysteretic nature of the SFS Fraunhofer pattern. Indeed, the study of the Fraunhofer modulation of I_c in SFS JJs is a tool to obtain fundamental information about the magnetic nature of the barrier. The measurement of the Fraunhofer pattern in SFS JJs allows, for example, an estimation of the the magnetization curve $M(H)$ of the F-layer. Due to the magnetic hysteresis of the F-layer, the $I_c(H)$ curves are shifted and distorted depending on the direction of the magnetic field sweep (see Figure 2.9). In particular

- by reducing H from positive to negative values, the maximum critical current is shifted to negative values of the magnetic field; we can call this curve as a *down curve* (black curve in Figure 2.9);
- by increasing H from negative to positive values, the maximum critical current is shifted to positive values of the magnetic fields; we can call this curve an *up curve* (red curve in Figure 2.9).

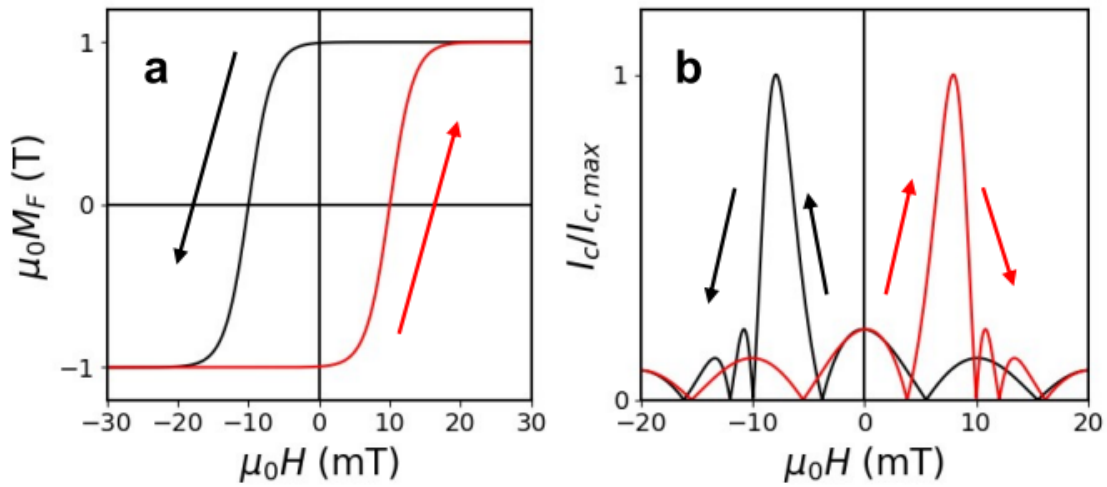


Figure 2.9: a) Hysteretic magnetization loop and corresponding b) $I_c(H)$ curve for an SFS JJ. The $I_c(H)$ curve is shifted in the direction of the swept field. [101].

The resulting Fraunhofer patterns are shifted in the field to a point where the flux due to the external field cancels out the flux due to magnetization. Specifically, we expect that when H is ramped from positive to negative fields (black $I_c(H)$ curves in Fig. 2.9(a)), the global maximum of the Fraunhofer-like pattern should be shifted towards negative fields due to the positive remanence of the F layer (black $I_c(H)$ curves in Fig. 2.9(b)), whereas as H is ramped from negative to positive fields (red curves in Fig. 2.9(a)), it should be shifted towards positive fields (red $I_c(H)$ curve in Fig. 2.9(b)).

2.3.2 SIsFS JJs

Due to the standard metallic nature of the ferromagnetic barrier, SFS JJs are often in the overdamped regime. In SIFS structures with an additional tunnel barrier I, the $I_c R_N$ product is increased in the 0-state [98], but the $I_c R_N$ is still too small in the π -state [102] due to the strong suppression of the superconducting correlations in the ferromagnetic layer. However, it is possible to obtain a JJ of type SIsFS (Figure 2.10), i.e., a serial connection of the SIs tunnel junction and sFS sandwich. Properties of SIsFS structures are controlled by the thickness of the s-layer d_s and by the relationship between the critical currents I_{cSIs} and I_{csFS} of their SIs and sFS parts, respectively. The SIsFS structure has a high characteristic voltage, $I_c R_N$, due to the presence of the tunnel barrier 'I' and the appropriate choice of layer s and F thicknesses and materials. At the same time the whole structure can behave as a single junction with respect to an external magnetic field H_{ext} and magnetic flux Φ penetrating into the structure, since the intermediate layer s is too thin to screen magnetic field. The discussion of the properties of SIsFS JJs assumes the dirty limit for the materials involved and an arbitrary finite transparency for the bilayer interface, which is assumed to be identical for both sF and FS interfaces. This transparency is in turn characterised by

two parameters [103] γ and γ_B :

$$\gamma = \frac{\rho_S \xi_S}{\rho_F \xi_F}, \gamma_B = \frac{R_{BF} A_B}{\rho_F \xi_F}, \quad (2.21)$$

which quantify proximity strength and interface transparency, respectively. Here R_{BF} and A_B are the resistance and area of the sF and FS interfaces, while ρ_S and ρ_F are resistivities of S and F materials, respectively. Under the above conditions the Josephson effect in the SIsFS junctions can be described by solving the Usadel equations with Kupriyanov-Lukichev boundary conditions at Is, sF and FS interfaces and with the bulk pair potential in the depth of S-electrodes [104].

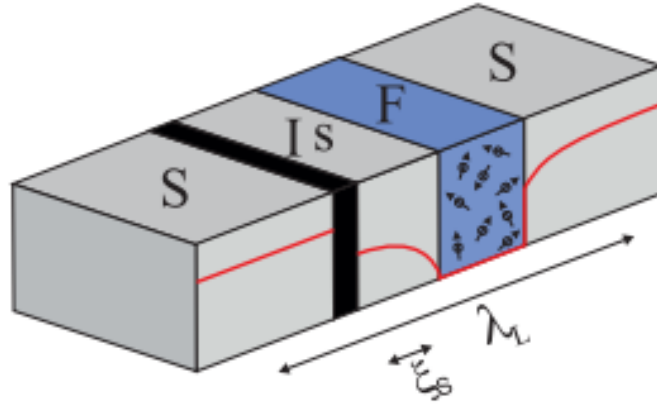


Figure 2.10: Sketch of a SIsFS junction. The red line shows the distribution of pair potential across the structure: it reaches bulk values in both S-electrodes, is suppressed in the superconducting interlayer s and vanishes in the ferromagnetic layer. The black arrows correspond to the London penetration length λ_L and the coherence length of the superconductor ξ_S , respectively [104].

Figure 2.11 shows the dependence of the $I_c R_N$ product on the ratio of the s and F thicknesses, d_s and d_F respectively, over their respective coherence lengths. Here, it is possible to observe different operating modes of the structure, defined according to chosen materials and layer thicknesses, and also according to the thickness of the intermediate layer d_s compared to the critical thickness d_{sc} , i.e., the minimal thickness of the s layer in a sF bilayer above which superconductivity still exists at a given temperature [104].

- **Mode 1:** If $d_s \gg d_{sc}$, the pair potential Δ in the s layer is close to that of bulk material and the SIsFS structure can be considered as a series connection of a tunnel SIs JJ and a ferromagnetic sFS junctions. This mode branches in two different cases depending on the thickness of the ferromagnetic layer:

(a) For small d_F and for the ordinary case in which $I_{c,SIs} \ll I_{c,sFS}$, then the characteristic voltage of an SIsFS device is determined by its SIs part and can reach its

maximum corresponding to a standard SIS junction. At the same time, the difference in phase φ of an SISFS junction's ground state is controlled by its sFS part. This can result in achieving either 0- or π -states, depending on the thickness of the F layer.

(b) At high d_F , the structure becomes a standard SFS junction with no barrier influence.

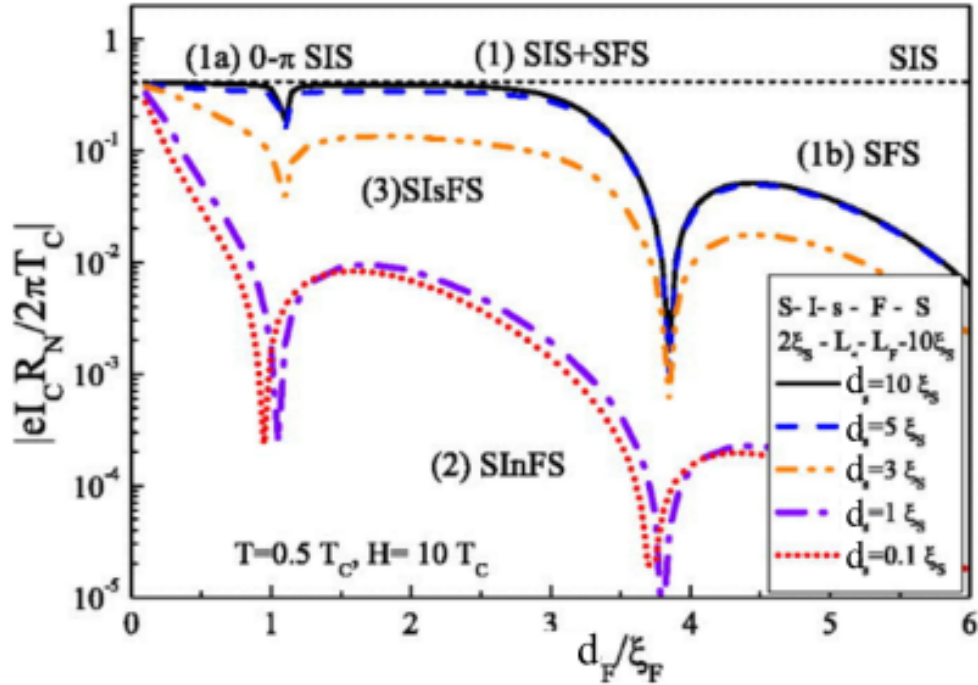


Figure 2.11: Characteristic voltage $I_c R_N$ versus ferromagnetic layer thickness layer d_F for a SIsFS junction for different values of the thickness of the superconducting interlayer d_s at $T = 0.5 T_c$. The dashed black line shows the corresponding behaviour of the $I_c R_N$ product for a SIS JJ. The interface parameters at the sF and FS interfaces are $\gamma_{BI} = 1000$, $\gamma_{BFS} = 0.3$, and $\gamma = 1$ at the sF and FS interfaces [104].

- **Mode 2:** If $d_s < d_{sc}$, The absence of superconductivity in the s-electrode leads to the formation of the complex -InF- weak junction region, where n denotes the intermediate s-film in the normal state. This results in a much smaller critical current value I_c , the magnitude of which is close to that in known SIFS junctions [102]. The dependence of I_c on the thickness d_s is weak due to the large decay length in the n-region with suppressed superconductivity.
- **Mode 3:** If $d_s \sim d_{sc} \sim 3\xi_s$, the properties of the structure are particularly sensitive to d_F and the exchange field of the F layer, since these parameters control the suppression of superconductivity in the sF bilayer. Within the considered intermediate thickness range, the system can transform from mode 1 to mode 2. These structures are characterized by the existence of the effective transition temperature

T_c^* , which corresponds to the appearance of superconductivity in the middle s-layer and, accordingly, to an exponential growth of the current (Fig. 2.12).

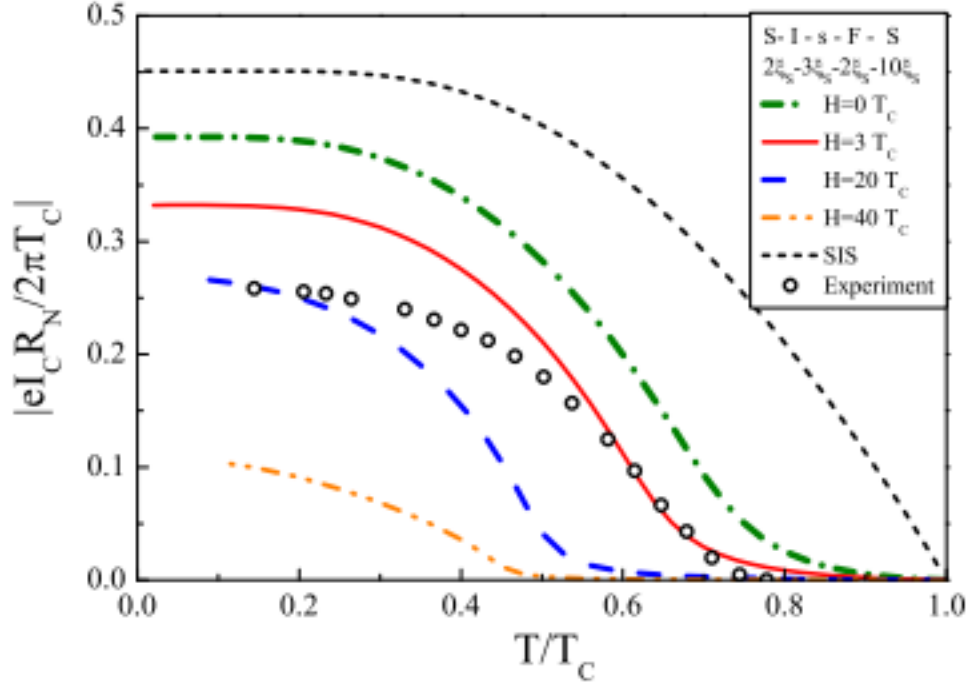


Figure 2.12: The temperature dependence of characteristic voltage $I_c R_N$ of SISFS structure in the mode 3 for different values of exchange field H_{ext} in the F-layer. The short-dashed line shows the dependence characteristic for a conventional tunnel SIS junction. It can be seen how the exchange field shifts the effective critical temperature T_c^* , corresponding to the switching of the s-layer from the superconducting to the normal state. The circles show $I_c R_N$ measured in Nb-Al/AlOx-Nb-Pd_{0.99}Fe_{0.01}-Nb junctions [105], demonstrating the existence of an effective critical temperature T_c^* in these samples [104].

In samples containing a F-barrier, to evaluate the total magnetic flux through the junction Φ , the F magnetization flux Φ_F , which is given by $\Phi_F = \mu_0 M_F L d_F$, with L the cross-section width, has to be considered. Hence, the total magnetic flux through the junction is $\Phi = \mu_0 H L d_m + \mu_0 M_F L d_F$, where the thickness of the material penetrated by the applied field is $d_m = 2\lambda_L + d_s + d_F + d_I$, with d_s the thicknesses of the thin superconductor and d_I the thickness of the insulator [106, 99]. This operating regime opens up the possibility of realizing switchable elements characterised by high quality factor and low dissipation, which can provide additional functionalities in both digital and quantum superconducting electronics [101]. If the interlayer thickness is such that $d_s < \lambda_L$, then the SISFS junction behaves as a single junction with respect to an applied external magnetic field H , because the thickness value is too small to shield the magnetic space.

2.4 MJJs for digital and quantum electronics

A ferromagnetic barrier in a JJ creates novel physics, but also holds the key to technological advances in fields ranging from digital to quantum electronics. Recently, interest in ultra-low-power, high-density cryogenic memory has spurred new efforts to exploit superconducting and magnetic properties simultaneously to create novel switching elements with these two competing ordering parameters [107]. Cryogenic superconducting technology is an excellent candidate for the realization of computing systems energy efficient digital computing. Single flux quantum (SFQ) cryogenic technology logic is based on the specific properties of superconductors and is intended to provide support functions for qubit circuits such as readout, control and error correction [108, 109]. However, the practical applications of these superconducting digital technologies will inevitably be very limited without compatible in speed and signal levels, high-capacity, energy-efficient random access memory (RAM) [100, 110]. Nevertheless combining superconducting elements with ferromagnetic layers and dots was suggested to achieve higher density of superconducting memory [111]. In order to achieve high energy efficiency of MJJ based memories, comparable to that of SFQ-type digital circuits, MJJs have to fulfil two main requirements: fast and low energy F-layer magnetization for *Write* operation and fast SFQ junction switching for *Read* operation [100]. It was already proven that a switching MJJ can be formed as a superconductor-ferromagnetic-superconductor (SFS) junction. In previous work investigating SFS structures, the $I_c(H)$ dependencies for all samples in [74, 86] were monovalent and had the standard Fraunhofer form. This indicated that the domain structure of the ferromagnetic interlayer was quite small scale and its magnetic fields were completely averaged at the scale of the F layer. Moreover, the magnetization of domains in CuNi and PdNi ferromagnetic interlayers used in those works was perpendicular to the plane of the sample [112]. The shift of the $I_c(H)$ dependence for Nb-CuNi-Nb junctions, which was due to the residual magnetization of the interlayer, was observed for the first time in [113]. The possibility of using SFS JJs as unit cells in Random Access Memory (RAM) has been demonstrated in Nb-Pd_{0.99}Fe_{0.01}-Nb junctions [98]. In these memory elements, there are two critical current levels below the saturation field of the F-layer, which can correspond to the two memory states. Specifically, an application of small external magnetic field changed the magnetization of the ferromagnetic layer that in turn changes the junction I_c , allowing the realization of two distinct states with high and low I_c , corresponding to logical '0' and '1' states, respectively. A magnetic field bias is usually applied to determine the optimum operating point, i.e., the field at which the difference between the upper and lower critical current levels ΔI is as large as possible. If the initial state is '0', the memory can be switched to the '1' state by applying a positive magnetic field pulse. On the the rising edge of the pulse, the critical current moves along the up-curve. On the the falling edge of the pulse, the critical current follows the down curves, and after

the pulse, the junction is in the '1' state (Fig 2.13a-d). Read operations are performed with a dc current I_R that lies between the two critical values corresponding to the logic states '0' and '1'. If I_R is greater than the critical current level, then the output signal is a finite voltage, whereas if I_R is less than the critical current level of the logic state, the output signal is a zero voltage (Fig 2.13a-c). Write operations are performed using magnetic field pulses to switch between the two $I_c(H)$ curves [100, 98, 57].

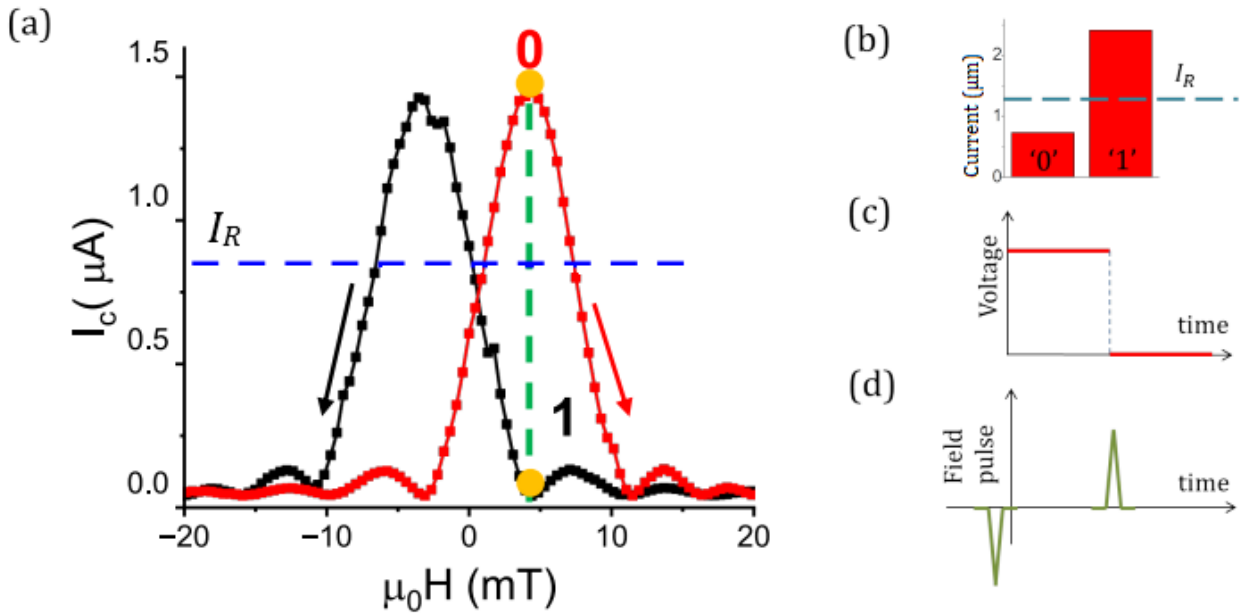


Figure 2.13: MJJ memory element operating scheme. (a) $I_c(H)$ curve: black and red arrows indicate the sweeping direction of the magnetic field to obtain the corresponding curve. Green vertical line corresponds to the field for setting the optimum working point. Blue horizontal line corresponds to the reading current I_R . Orange dots indicate the memory states, (b) Critical current levels and corresponding logical states, blue line is the reading current. (c) Voltage levels corresponding to the two logical states. (d) Diagram of the pulses used to switch between logical states [101, 57]

Therefore, in Ref. [113], a junction bias current ($I_{read} = 240 \mu\text{A}$) was chosen to switch the SFS junction from a superconducting to a resistive state by a weak magnetic field pulse. This experiment provides the first evidence that a superconductor-ferromagnet Josephson junction can be used as a non-volatile memory device with non-destructive readout, potentially scalable to small size and high density. The MJJ critical current can change and maintain its value through the magnetization of the ferromagnetic layer, so a memory element size is defined by the scalable MJJ device, enabling high-density RAM. [113]. However, the characteristic frequency of

a JJ switching process $\omega_c = (2\pi/\Phi_0)I_cR_N$ is determined by the I_cR_N product and it is typically too low in devices based on standard metallic SFS.

Indeed, the characteristic voltage I_cR_N of these SFS devices [100] was in the order of nanovolts, which makes them too slow (\sim MHz rate) to be applicable to prospective memory applications. SFQ logic, the main JJ technology for digital and mixed-signal circuits [114], is mainly based on tunnel SIS JJs whose I_cR_N product is in the range of 0.2 - 0.7 mV, resulting in a high characteristic frequency $\omega_c/2\pi \approx 100 - 350$ GHz [107]. By inserting an additional insulating tunnel layer I in the SFS junction (i.e. by fabricating a superconductor-insulator-ferromagnet-superconductor (SIFS) structure), it should be possible to increase $V_c = I_cR_N$ to 1 mV to achieve a high switching frequency. This should bring the switching speed of the MJJs close to that of the SIS JJs, while retaining the useful memory characteristics of the SFS MJJs [100]. In fact, in order to increase the switching speed of MJJs, in Ref. [113], devices based on Nb-Al/AlOx-Pd_{0.99}Fe_{0.01}-Nb tunnel junctions with V_c from 100 to 400 μ V (ω_c of ~ 50 GHz) are fabricated and demonstrated.

MJJs have mainly been used as passive elements in quantum circuits because of their of their intrinsically high quasi-particle dissipation. However, recent capabilities in ferromagnetic layers with an insulating barrier and in exploiting the intrinsic insulating ferromagnetic materials inside MJJs, have opened up the possibility of implementing JJs in hybrid quantum architectures. Superconducting qubits are one of the most promising paradigms in quantum computing. A wealth of successful experiments have demonstrated how efficiently these devices can be manipulated and read by commercial electronics, how flexible their Hamiltonian is, how precise the control over their quantum state is [115, 116].

When implementing Josephson junctions to realise qubits, it can be advantageous to be able to tune the operating characteristics of the entire system. One common modification used with transmon qubits is to use two similar Josephson junctions in parallel as opposed to using a single junction [117]. The two junctions then form a superconducting loop, i.e., a SQUID (superconducting quantum interference device). The SQUID arrangement allows the effective Josephson energy of the entire circuit to be tuned by the application of an external magnetic flux [117]. By modifying the Josephson energy, the effective inductance of the SQUID loop can be tuned dynamically. This makes unique qubit operations possible that are not achievable with fixed qubits, such as natural atoms or ions [118, 5]. Recently, it has been proposed that the memory properties of MJJs can be alternatively tuned by applying magnetic field pulses in a hybrid superconducting qubit, the so-called *ferro-transmon*. Due to the presence of a ferromagnetic layer, MJJs allow the state of the system to be switched as a function of the applied magnetic field .

In [8] it has been shown that the characteristic hysteretic behaviour of the ferromagnetic barrier provides an alternative and intrinsically digital tuning of the qubit frequency by magnetic field pulses. Considering that superconducting quantum circuits rely almost exclusively on aluminium (Al)-based JJs, [119, 120] the search for novel circuit designs and combinations of novel materials plays a key role in pro-

moting alternative control and readout schemes in superconducting qubits. To this end, the concepts and recipe optimized for SISFS tunnel JJs in Nb were transferred to JJs with aluminium electrodes. This transfer is extremely valuable in broadening the possible solutions for an increasingly versatile Al-based technology [10].

For the realization of ferro-transmon, the SISFS structure can be considered as a series of a standard tunnel SIS JJ and the ferromagnetic sFS JJ [10]. In this way, magnetic effects occur in a junction that is essentially a tunnel, but behaves like a standard junction, with a high quality factor, an underdamped system, very low quasiparticle current, and therefore very low thermal system excitations, all of which are essential prerequisites for the realization of a superconducting quantum bit. Since the ferromagnet is hysteretic, the critical current and thus the Josephson energy of the system can be changed depending on the magnetic field applied to the junction. With standard non-ferromagnetic qubits, when a static magnetic field is applied, it is maintained throughout all operations of the qubit, so if the magnetic field is due to an external current from a generator, it will have its fluctuations, so it will have associated flux noise. In the ferromagnetic qubit, on the other hand, precisely because of hysteretic behaviour, the moment a magnetic pulse is applied, it regulates E_J , but one can continue to perform all operations on the qubit without applying a static field, i.e. the external source of noise is switched off.

–3–

Experimental setup

In order to electrically characterise the manufactured samples, it is necessary to reach temperatures below the critical temperature of the devices. Cryogenic systems are used for this purpose, which not only allow temperatures close to absolute zero to be reached, but also minimise thermal effects during the measurement. In this chapter, we will describe the experimental setup and the measurement techniques used to study the behaviour of junctions in a temperature range between 10 mK and the critical temperature of the superconducting devices. We will focus in particular on the description of the cooling system and filtering system. In addition, we will give an overview of the techniques used to perform DC- measurements for Josephson junctions. Finally, we will describe the samples that have been analyzed.

3.1 Triton Dilution fridge

To perform d.c. measurements down to ~ 10 mK, we employ a *Triton* refrigerator system provided by *Oxford Instruments*. The Triton system is a cryofree cryostat, i.e., it is dry, which does not require cryogenic liquids to reach temperatures in the order of a few milliKelvin. The fridge consists of several stages of progressively lower temperatures, enclosed in a cylindrical high vacuum chamber, referred as the outer vacuum chamber (OVC). High vacuum is required to decouple with the environment, and the pressure inside the chamber is less than 10^{-5} mbar. The stages are made of copper gold- and silver-covered plates, thermally decoupled by stainless steel supports. As illustrated in Fig. 3.1, starting from the top of the cryostat, we have:

- the RT-plate, at room temperature;
- the PT1, at ~ 70 K;
- the PT2, at ~ 4.2 K;

- the still-plate, at ~ 700 mK;
- the IAP-plate, or cold-plate, at ~ 100 mK;
- the MC-plate, at ~ 10 mK.

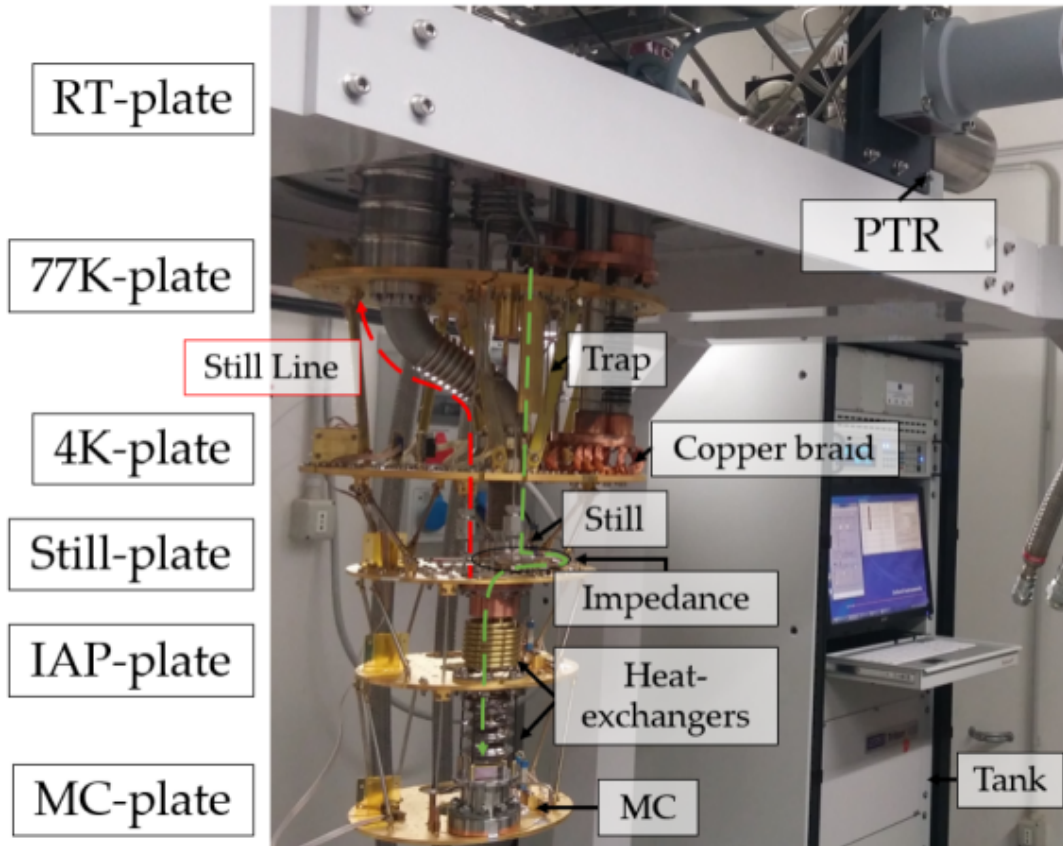


Figure 3.1: Triton system description: the labels indicate the different plates and the minimum temperature that they can reach, the green and red path indicate the dilution unit and the pre-cool unit respectively, which are the basic units of the Triton cooling procedure.

The temperature relative to the plates of the dilution unit was obtained using the method proposed by Heinz and London in 1950s [121], characterized by three main stages, which we will describe in more detail.

The first phase is the *condensation*, where a small amount ${}^3\text{He} - {}^4\text{He}$ mixture gas contained in a sealed volume inside the cryostat is pumped into a liquid nitrogen tank acting as a trap, where it is cooled from room temperature to 77K and purified. Then a pulse Tube Refrigerator (PTR) pre-cools the system down to about 10 K. Vibrations from the PTR can cause noise during the measurement phase, so special

copper braids are used on PT2 to decouple the PTR from the subsequent plates. In this way, the experimental set-up undergoes a Pre-Cooling (PC) phase through a series of heat exchangers located on PT1, PT2, the still plate, the cold plate and the Mixing Chamber (MC).

Once ~ 10 K is reached, the pre-cooling loop is removed from the circuit using a turbo pump and the mixture is compressed at high pressure (~ 2.5 bar) using the KNF ^3He compressor. By using a series of heat exchangers and pressure filters based on the Joule-Thomson expansion principle, temperatures below ~ 2 K are reached at which the ^3He condenses (1.7 K) in the mixing chamber, reducing its temperature to about 1 K.

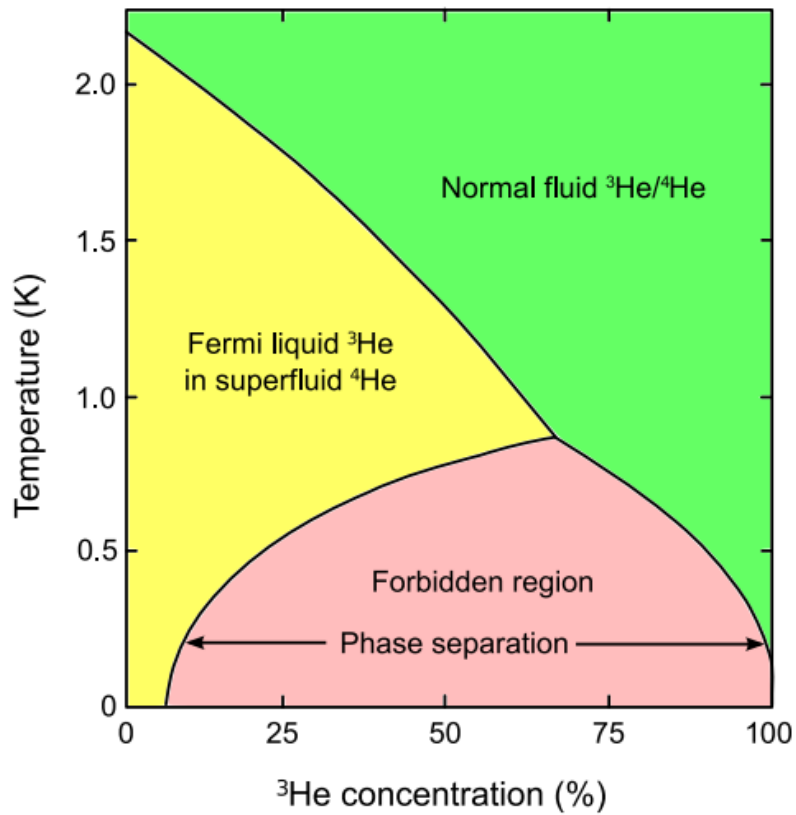


Figure 3.2: Phase diagram of ^3He - ^4He in terms of temperature and concentration of the mixture.

The *dilution phase* uses a thermodynamic process that occurs when a mixture of ^3He and ^4He is cooled appropriately. Below 1.2 K, when ^3He and ^4He are both liquid, a phase transition point is reached at about 800 mK. At this point, as can be seen from the diagram in Figure 3.2, there is a phase separation between a concentrated ^3He phase and a dilute ^3He phase, i.e. a phase with more ^3He molecules and a phase with fewer ^3He molecules. The transfer of ^3He from the MC is an endothermic

process that lowers the temperature to 10 mK.

Finally, the ^3He molecules in the MC are pumped out through the still line and recondensed again (*circulation*). In the still chamber, it is possible to increase the degree of evaporation of the mixture, thereby optimising the circulation process.

Control of the pumps, pressures, temperatures and valves in the cryostats is achieved using an Intelligent Gas Handling (IGH) system controlled by LabVIEW software from Oxford Instruments.

Finally, to protect from external radiation, 70K- and 4K-plates are fitted with aluminium shields.

3.2 Filtering systems and electronics

To make accurate measurements of the transport properties of Josephson junctions, it is necessary to use a special filtering system to minimise noise from thermal and electronic noise.

3.2.1 DC setup

The cryogenic system we use, the Triton, makes it possible to carry out four-contact measurements on several samples at the same time, as it is equipped with 48 DC lines, 24 of which are dedicated to carrying current and 24 of which allow the voltage difference at the ends of the devices to be measured (voltage lines). In particular, half of these lines (12 current and 12 voltage lines) are equipped with different filtering stages, which are essential for the acquisition of very low intensity current and voltage signals [22].

From the RT-plate to the 4K-Plate, copper and constantan twisted pairs are used for current and voltage lines respectively. In particular, for the current it must be a line with low electrical conductivity, because it is current biased. From the 4K-Plate to the MC-plate, instead, to further reduce the resistance of the lines, a superconducting alloy consisting of Nb and Ti is used for the *I*-lines, while the *V*-lines are homemade manganin twisted cables, which have high resistance but do not dissipate too much heat.

The constantan and the manganin are characterized by a low thermal conductivity, and therefore suitable for voltage measurements. The manganin has best performances at low temperatures compared with the constantan [122].

RT to 4K A first filtering stage at room temperature is located on the top of the cryostat, where the low pass EMI filters (*ElectroMagnetic Interference*) connected to the input lines *I* and *V* are positioned. These are RC filters that remove electromagnetic high frequency peaks such as the ones coming from mobile phones. The *I*

and V lines pass through two Electrolytic Tough Pitch (ETP) copper boxes, which are anchored to the 4K-plate. Each copper box contains two electrically isolated chips with six RC filters each, with a common ground to the copper box. 12 twisted I and V pairs pass through the box and are connected directly to the box's RCA output (unfiltered lines), while the other lines are connected to the filters. The reason for using second order RC filters rather than standard RC stages is that the input signal requires different degrees of attenuation at different frequency bands.

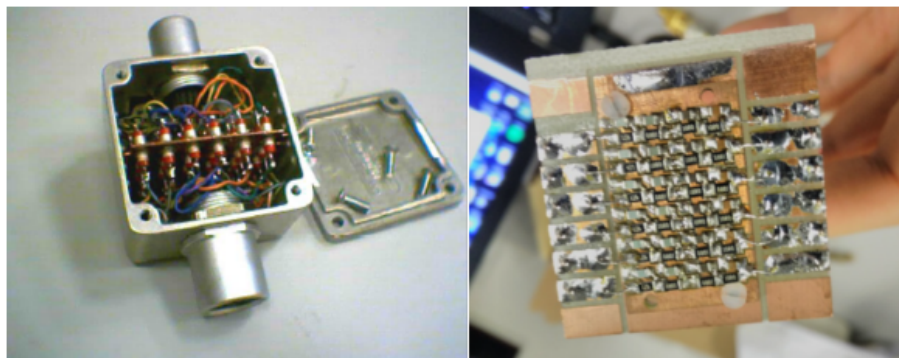


Figure 3.3: Picture of the first two filter systems: left the EMI filters, right the RC filters.

IAP to MC At higher frequencies, the parasitic inductance of the capacitors causes a significant loss of attenuation. To overcome this problem, an additional filter stage consisting of two *brass powder filters* [123] is fitted to the IAP plate in the Triton. The attenuation of high frequency signals is due to the dissipation of the current induced in the grains, depending on the powder material, their size, diameter and length of the wire [123, 124, 125]. With these precautions, high precision and resolution in the microvolt and nanoampere can be achieved [9]. Finally, all signals pass through a battery-powered, low-noise amplifier to avoid other sources of electrical noise.

In the Triton, we have two rows of 12 insulated manganin (for the voltage lines) and copper wires (for the current lines) with a diameter of 0.1 mm encapsulated in a cylindrical paste of resin, hardener and brass powder. In general, mixing the powder with epoxies allows us to obtain a better thermalization of the central wire compared to pure powder filters (Fig. 3.4) [123, 124, 125]. Both manganin and copper wires are shaped into a spiral with a distance between loops of 0.1 mm diameter. The total length of the wires is of the order of 2.5 m. The 24 filtered I and V lines terminate in a RCA connector which is plugged into the sample holder stage, which is thermally and mechanically anchored to the bottom of the MC plate. Inside the sample holder, there is a home-made Cinch-to-Fischer cable made of NbTi (for the current lines) and manganin (for the voltage lines), thermally anchored to the sample holder.



Figure 3.4: Picture of the copper powder filters, in the box on the right a detail of the internal structure of the copper cylinders.

The coldest possible plate, the one at 10 mK, is where the experiments are mounted after the system has cooled down. Figure 3.5 shows the section dedicated to DC measurements, i.e., nanostructures or, as in this case, the Josephson effect.



Figure 3.5: DC-sample stage.

Another aspect to consider when studying JJs is the shielding of the samples from the external magnetic field. For this reason, the Triton sample holders are designed to provide a 1 mm thick external cryoperm screen and a 1 mm thick internal lead screen around the samples.

Finally, the characterization of JJs, and in particular SIsFS JJs, requires the use of

superconducting coils. In the Triton the coil is mechanically anchored to a copper ring centered on the sample stage by means of non-conducting stands. The coil lines are copper from the RT plate to the 4 K plate and superconducting (NbTi) from the 4 K plate to the MC. They are thermalized at the 70 K plate, the 4 K plate and the cold plate (IAP), and otherwise covered with a fibreglass glove.

3.3 Readout electronics

The electronic setup connected to the cryostat allows for different measurements useful to characterize different types of devices. In this section, we will discuss the measurement techniques used for most of the characterisation of superconducting systems in a DC environment, including the ferro-tunnel JJs reported in this thesis.

3.3.1 $I(V)$ measurements

The characterisation of the junctions was carried out using the four-contact technique, because one does not want to measure the resistance at the ends of the lines, but only the resistance at the ends of the junction, so two contacts are needed to give the current (I_+ and I_-) and two contacts to read the voltage (V_+ and V_-) at the ends of the junction. This is extremely advantageous compared to a two-contact measurement, as it excludes the potential drop due to the impedance of filters and lines, which would add to the voltage drop at the ends of the junction. The junctions are current biased by a triangular voltage ramp with frequencies around 10 Hz, emitted by an Agilent 33120A arbitrary waveform generator connected to a variable shunt resistance, generally very high (1 M Ω), chosen to have a value greater than the resistance of the junction and the lines.

The current flowing through the device is

$$I_{bias} = \frac{V_{pp}}{R_{shunt} + R_{line} + R_{junction}} \approx \frac{V_{pp}}{R_{shunt}} \quad (3.1)$$

with a peak-to-peak V_{pp} amplitude that falls on the variable shunt resistance R_{shunt} . The error on the generated voltage is at least one order of magnitude less than V_{pp} . The current passing through the device is pre-amplified by the Stanford SR570 Current Preamplifier, which converts the current signal into a voltage that can be read on the LeCroy Wave Runner 6100A oscilloscope. Finally, the voltage drop measured at the junction electrodes is amplified by a variable gain differential voltage amplifier and then sent to the oscilloscope. This instrument records a series of 100 curves and averages the measured signal to reduce noise effects. The oscilloscope is connected to the computer, where we saved all the measurements.

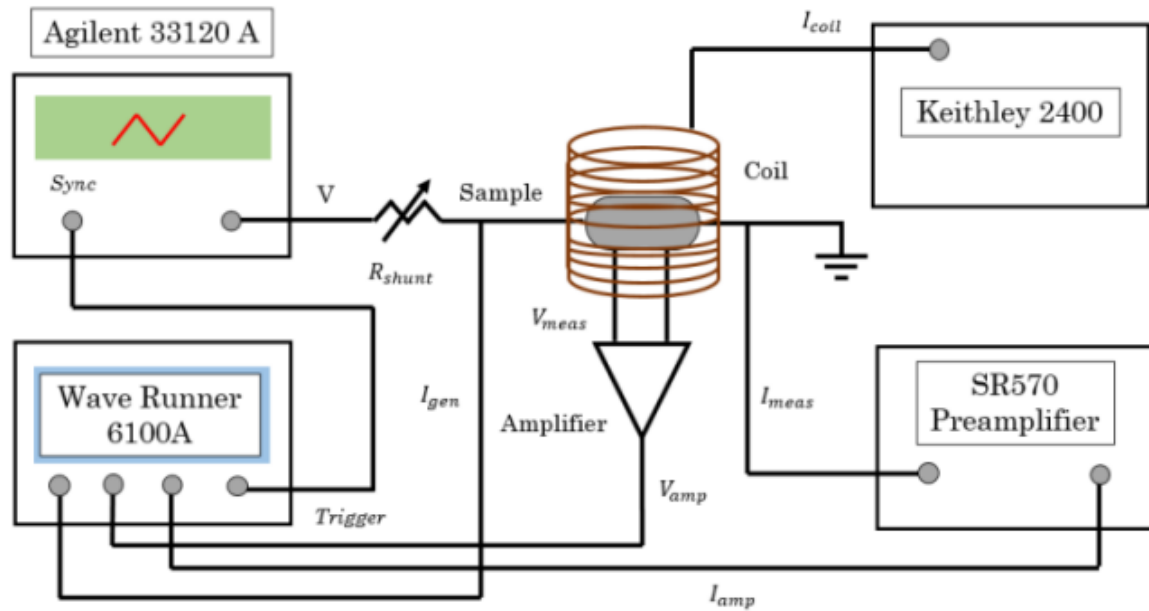


Figure 3.6: Sketch of the DC setup used for current-voltage measurements as a function of temperature [101].

The experiment results can be significantly affected by the complexity of the set-up, along with the presence of filtering and amplification stages, electrical and thermal noise effects, and the number of degrees of freedom of the solid state sample. To accurately define the properties of the junctions being studied, it is crucial to evaluate the associated measurement errors. The temperature of the reservoir where the Josephson junction is thermalized is registered through an electrical measurement of diode resistance. At low temperatures, the sensitivity of the diode resistance is about $1 \times 10^{-4} K$. The voltage measurements associated error mainly arises from the noise signal, while that due to the instruments is negligible compared to the noise. Figure 3.7 displays a zoom of the noise band of an I-V characteristic of a Josephson junction at a temperature of 0.8K.

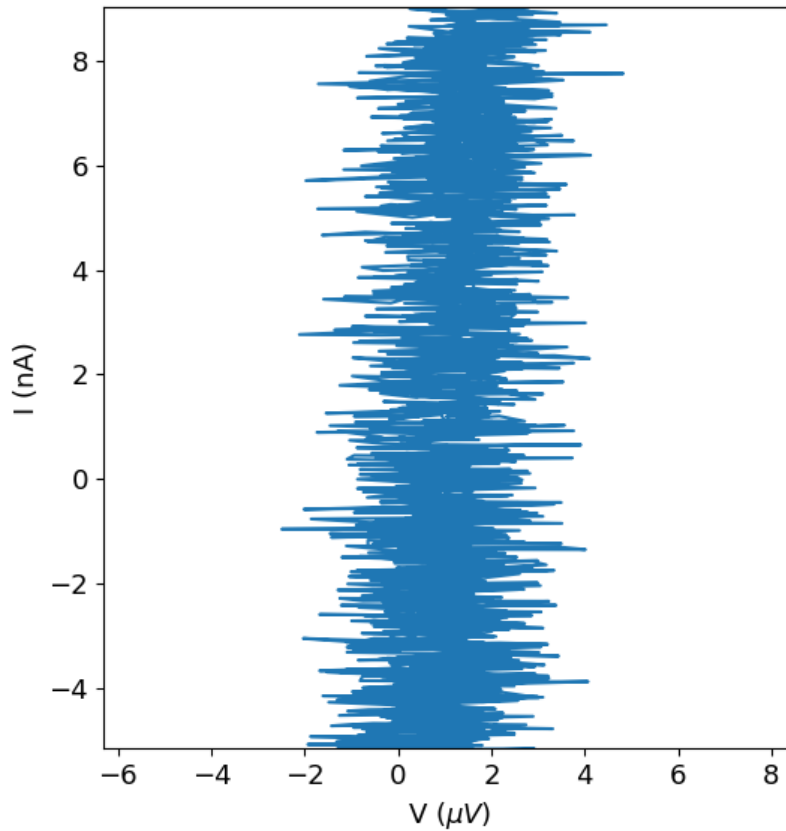


Figure 3.7: Detail of the superconducting branch of a current-voltage curve at $T=0.8\text{K}$ for an Al-based Josephson junction. The voltage noise amplitude is shown to be $4\mu\text{V}$ wide..

The voltage noise band has a width of $\Delta V = 4\mu\text{V}$, enabling the estimation of a relative error of $\Delta V/V = 2\%$ when defining the I_c values using a fixed voltage threshold.

3.3.2 Measurements in magnetic fields

The magnetic field is generated by connecting Source Meter Keithley 2400, used as a current generator, to a superconducting coil of NbTi, which is connected within the system to the plate at $\sim 10\text{mK}$. It is driven by current with a current/magnetic field conversion factor of 0.1 T/A . The error on the generated current is $0.012\% I_{coil}$, as declared in the instrument specifications [126].

In a first moment we applied a magnetic field from zero to an upper value (virgin curves); then we applied a field from a positive value to a negative value (down curves) and back again (up curves). For each value of the magnetic field, we acquired the $I(V)$ characteristics with a step ΔI_{coil} and a waiting time t_w between each acquisition, chosen to obtain accurate measurements; we set the waiting time to $t_w = 1\text{ s}$. The number of average sweeps was set to 20. Source Meter Keithley

2400 is remotely connected to the PC via a GPIB (General Purpose Interface Bus) interface, from which measurements can be initiated using labview programs.

3.3.3 Conductance measurements

Conductance spectra measurements provide information on the density of states of the samples, as the differential conductance dI/dV versus V in a superconductor is proportional to the density of states [15]. In this case, the input current is the sum of two signals: a low frequency (1 mHz) triangular ramp and a small sinusoidal excitation at about 30 Hz. The optimum ratio between the two signal amplitudes is of the order of 10^{-3} . The output dV signal is read from the lock-in amplifier, which is used to compute the conductance dI/dV . The quasi-dc output voltage is read using an Agilent 34401A multimeter with a six digit display. The circuit for such measurements is shown in figure 3.8.

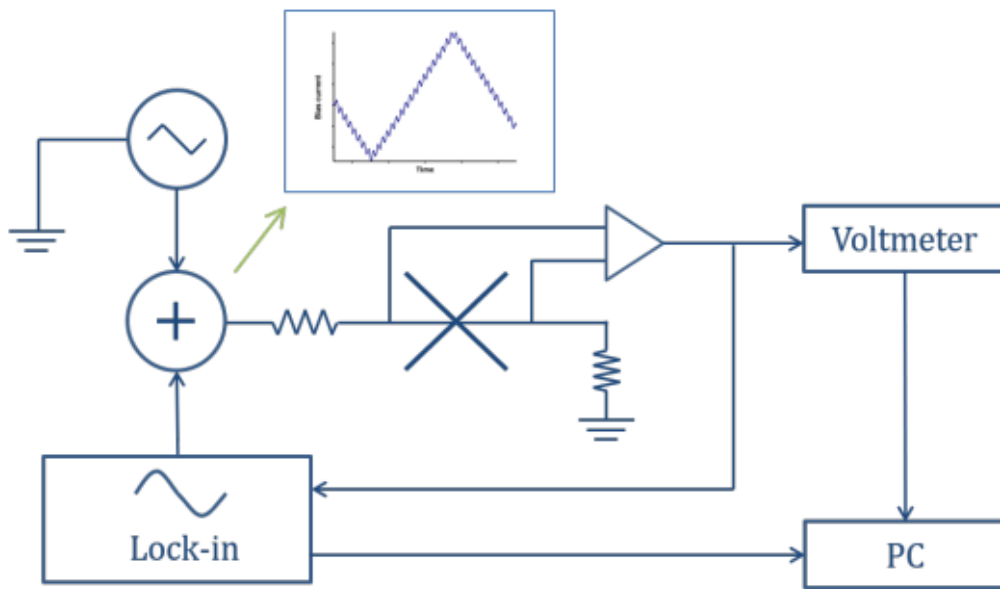


Figure 3.8: Diagram of the circuit used to measure the dI/dV curves [127].

3.3.4 Switching Current Distribution measurements

Finally, switching current distributions (SCDs) were measured, which allow the reconstruction of the electrodynamic properties of Josephson junctions. The evaluation of the probability of the current switching from the superconducting to the finite voltage state is a powerful tool that allows a better understanding of the phase dynamics for the fabricated junctions. In addition, the information obtained from these measurements also provides a means of checking the regime in which the

fabricated junctions operate by estimating the Q factor after the SCDs have been measured.

SCD measurements are performed as follows: first, the voltage at a constant frequency of 5.123 Hz and a peak-to-peak value of 1.8 mV from the waveform generator and the measured current are read on the oscilloscope. A voltage threshold is then fixed close to the switching current value in order to detect the actual switching event and to count it in time: a total of 5×10^3 events are processed for each temperature (see fig. 3.9). This allows a histogram of the switching currents to be generated. The switching current counts $N(I)$ allow the switching current probability density distribution $P(I)$ to be calculated by dividing the $N(I)$ histogram by the area of the distribution, which is given by the integral of the switching current counts. The mean switching current value I_{mean} , its variance σ^2 as the second moment and the third momentum of the distribution m_3 are

$$I_{mean} = \sum_i \frac{N(I_i)}{N_{tot}} I_i \quad (3.2)$$

$$\sigma^2 = \sum_i \frac{N(I_i)}{N_{tot}} (I_i - I_{mean})^2 \quad (3.3)$$

$$m_3 = \sum_i \frac{N(I_i)}{N_{tot}} (I_i - I_{mean})^3 \quad (3.4)$$

where N_{tot} is the total number of counts and I_i are the switching current values. The standard deviation σ and the skewness γ are calculated as:

$$\sigma = \sqrt{\sigma^2} \quad (3.5)$$

$$\gamma = \frac{m_3}{\sigma^3} \quad (3.6)$$

The error on I_{mean} is the standard deviation σ , while the error on σ taking into account the propagation of the error

$$\Delta\sigma = \frac{1}{2\sigma} \sqrt{\sum_i ((I_i - I_{mean}^2) \Delta N_i)^2}, \quad (3.7)$$

where ΔN_i is the Poisson error on the counts $\Delta N_i = \frac{\sqrt{N_i}}{N_{tot}}$.

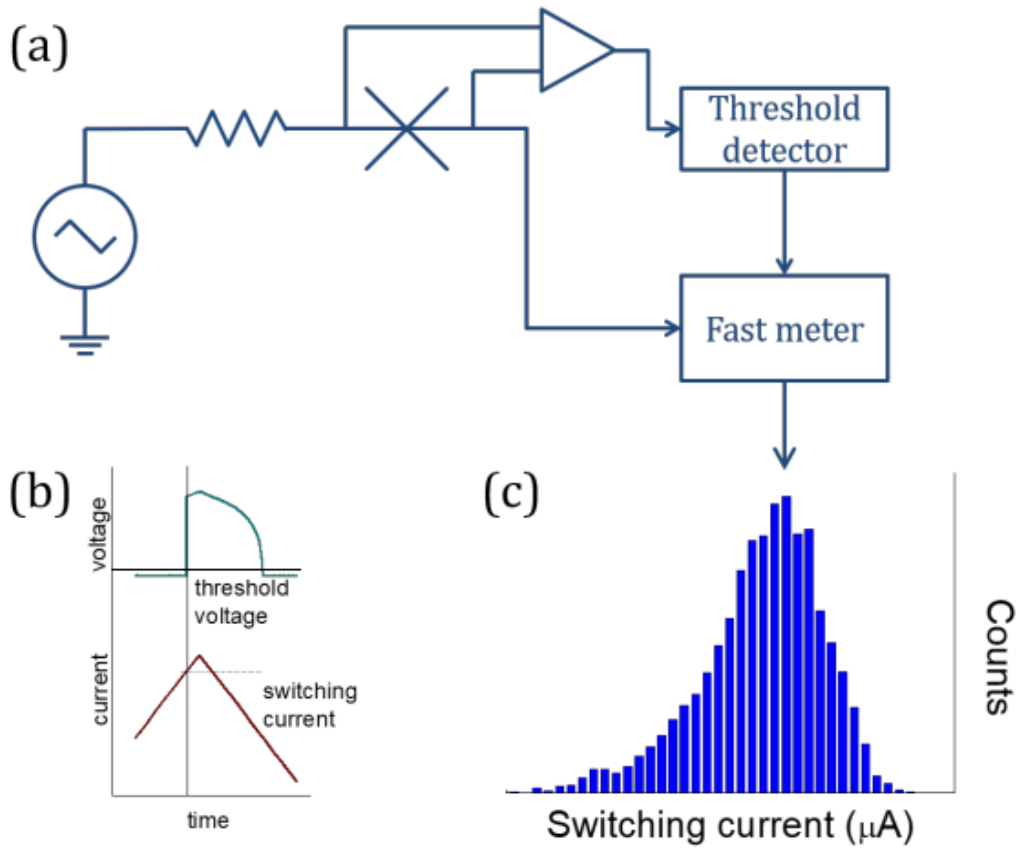


Figure 3.9: (a) Circuit diagram for SCD measurements. (b) Junction output signals and threshold voltage (black dashed line) set for SCD measurements. (c) Histogram of switching current distribution [127].

3.4 Samples scheme

In this work, hybrid aluminium-based SIsFS Josephson junctions (JJs) have been investigated: the samples were fabricated at the CNR-ISASI in Pozzuoli and the Physics Department of the University of Naples. An innovative fabrication process inspired by niobium-based technology, already well known for the production of high quality hybrid junctions widely used as magnetic switches for cryogenic RAM [128], has been used to obtain very high quality hybrid aluminium Josephson junctions, supporting the use of ferromagnetic Josephson junctions in advanced quantum circuits. Figure 3.10 shows an image of a junction set using a SEM and a detail showing a circular junction with an area of about $7 \mu\text{m}^2$ using both a SEM and an AFM.

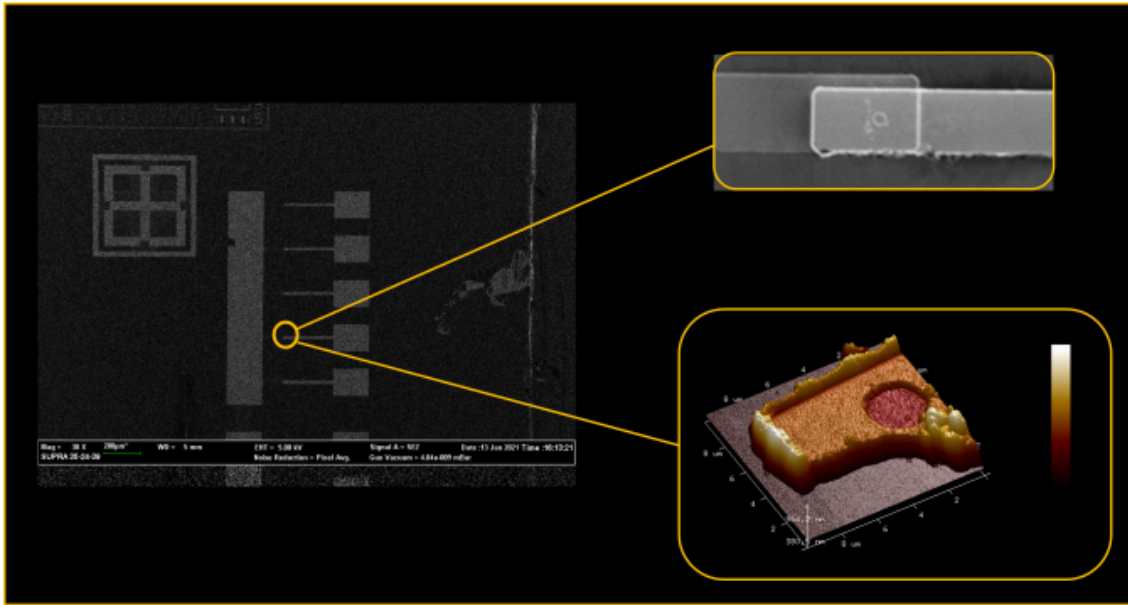


Figure 3.10: SEM image of a set of circular SISFS with diameters ranging from 2 to 10 μm . Upper inset: magnification of a circular junction with a diameter of 3 μm . Bottom inset: AFM image of a circular junction with a diameter of 3 μm .

In addition to the choice of a different superconducting material, another novelty for the junctions investigated is the use of a ferromagnetic material. In fact, until recently, the ferromagnetic material used for SISFS junctions was $\text{Pd}_{0.99}\text{Fe}_{0.01}$, which is a weak ferromagnet: however, this material, as already expressed in section 2.4.1, is not suitable for the next generation of nanoscale JJs.

Thus, in recent years, PdFe has been replaced by a strong ferromagnetic $\text{Ni}_{80}\text{Fe}_{20}$ interlayer alloy (Permalloy), which is more suitable for the realization of small area JJs and allows the realization of SISFS JJs down to $7\mu\text{m}^2$ [11]. Compared to other superconducting materials such as niobium, aluminium turns out to be a nonrefractory material, cannot withstand strong magnetic fields and has a rather low critical temperature. Nevertheless, aluminium was used for these JJs, as it is the state-of-the-art material for the fabrication of modern qubits, due to the coherence times achieved for qubits made of Al [129].

The fabrication of these high quality micron-sized aluminium (Al) JJs uses the concepts and recipe optimised for Nb tunnel junctions, which is based on the anodization of the Al top layer and an additional silicon dioxide insulating layer [130, 131]. This provides a reliable and reproducible process to obtain high quality JJs with Al electrodes down to $12\mu\text{m}^2$ by standard optical lithography, with E_J values suitable for integration into a transmon quantum architecture. Furthermore, the process allows the deposition of additional layers, in particular the ferromagnetic (F) layer, after the definition of the junction. These JJs appear to be the smallest SISFS memory elements ($\sim 7\mu\text{m}^2$) compatible in speed and power dissipation with

single flux quantum (SFQ) circuits. Furthermore, given the stability of the of the magnetic properties of Py, there is in principle no limitation to further reducing the cross section of the JJs down to submicron dimensions [101, 99]. The figure 3.11 shows the finished samples with the different layers.

To examine the tunneling characteristics of SISFS JJs with Al as the S layer, two sets of SISFS JJs with three different types of ferromagnetic layer were prepared:

1. Al (200 nm)/AlO_x (3 nm)/Al (30 nm)/Py (3 nm)/Al (400 nm) JJs,
2. Al (200 nm)/AlO_x (3 nm)/Al (30 nm)/Py-Gd (3 nm)/Al (400 nm) JJs,
3. Al (200 nm)/AlO_x (3 nm)/Al (30 nm)/Py-Gd-Nb (3 nm)/Al (400 nm) JJs.

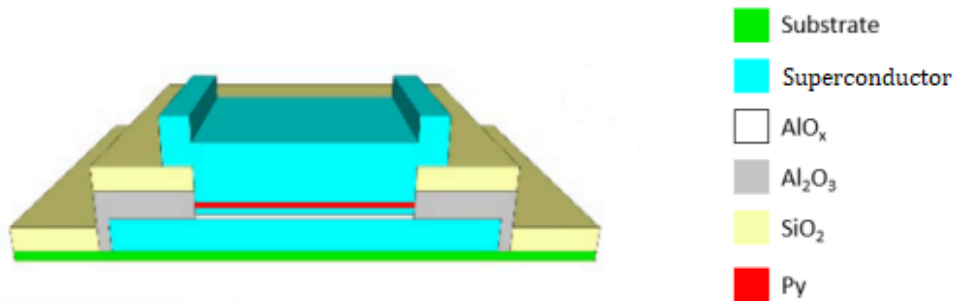


Figure 3.11: Schematic of a finished sample [129].

Figure 3.12 shows an optical image of a set of junctions and a circular junction with an area of about $12 \mu\text{m}^2$ in the inset.

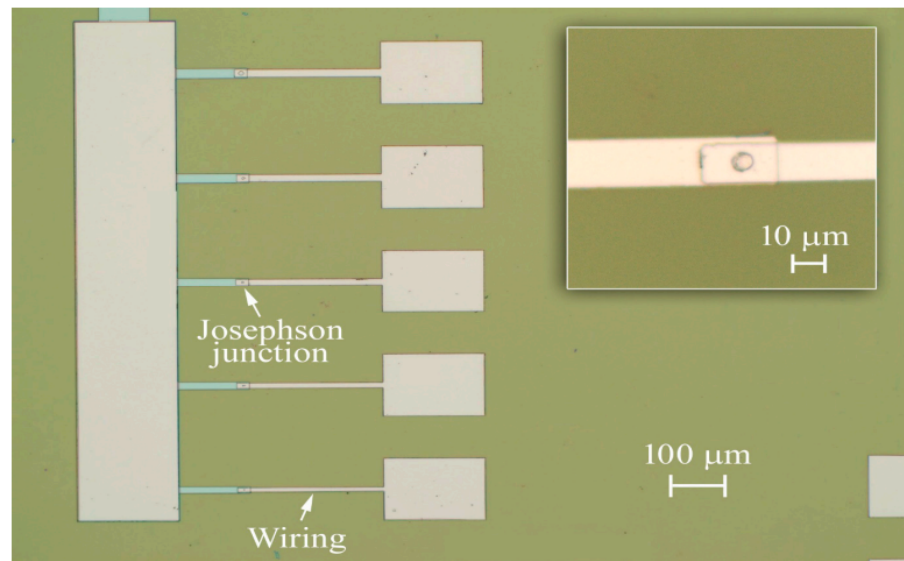


Figure 3.12: Optical microscope image of a set of circular SIsFS with a diameter D ranging from 2 to 10 μm . The inset shows the magnification of a circular junction with $D = 5\mu\text{m}$ [129].

–4–

Data analysis

A detailed analysis of the measurements performed on SISFS junctions is presented in this chapter. Measurements on the fabricated samples have been carried out at the QT Lab of the Università degli Studi di Napoli "Federico II". The former part focuses on their behaviour as a function of temperature and magnetic field. Next, conductance measurements are taken on two specific junctions, with and without the ferromagnetic interlayer. The latter half of this chapter is concerned with the measurements of switching current distributions (SCDs) which are a powerful tool for studying the phase dynamics of JJs.

4.1 Characterization of the samples

In order to identify the best samples, a first pre-selection was carried out using a probe station (Figure 4.1) at room temperature. Room temperature resistance was measured by connecting the Python software to Keithley via GPIB. In this way, this tool enabled the working junctions to be distinguished from the damaged ones.

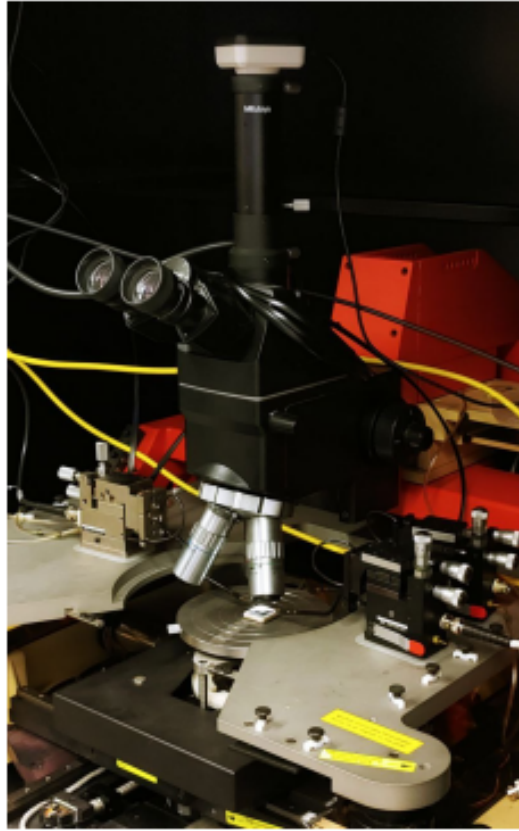


Figure 4.1: The probe station used for the initial selection of the junctions. Measurements were made at room temperature.

Circular hybrid SISFS and circular tunnel SIS Josephson devices with different junction areas and the same tunnel barrier thickness have been measured.

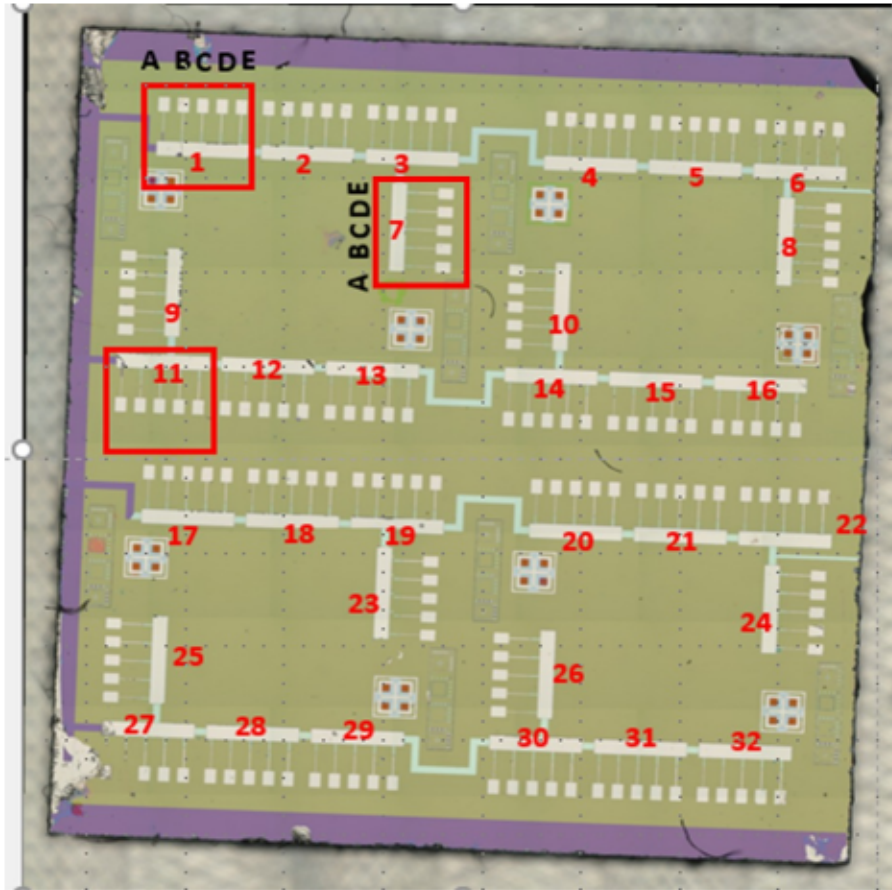


Figure 4.2: Chip layout of the fabricated samples. The individual junctions are with a number representing the specific pad they are from and a letter representing their diameter. The diameters are $2\mu\text{m}$, $3\mu\text{m}$, $4\mu\text{m}$, $5\mu\text{m}$ and $10\mu\text{m}$ respectively: the junctions are labelled with the letters A to E - starting with the smallest - according to their diameter.

4.1.1 Current-Voltage characteristics and Conductance

The analysis of temperature dependence of a Josephson junction is an essential part of its characterisation. This analysis yields certain parameters that assess the quality of a fabricated JJ. Figures 4.3 a) and b) show the IV characteristics for the SIS and SISFS JJs based on a Aluminum technology, at $T = 10\text{mK}$, in short and long range respectively. The acquisition of IV curves, divided into two data sets, short-range and long-range, allows us to obtain all the necessary information about these samples. The former allows a better investigation of the critical current of the device. The latter is useful for determining R_N , but it is also used to derive the gap voltage V_{gap} , which is evaluated experimentally from the graph as the point before the subgap branch begins to bend, i.e., before the ohmic branch. As the curve in Fig. 4.3 shows points with both negative and positive values of I and V, the

mean value $(I_{c+} + I_{c-})/2$ was found to estimate I_c , where I_{c+} and I_{c-} are the positive and negative critical current of the IV. The margin of error on the critical current, I_c , was assessed using formulas 3.3 and 3.5, based on the width of the probability distribution of the values of I_c at the base temperature (Figures 4.9-4.10). A linear fit on the ohmic branch of the IV curve in the long range allowed us to determine the parameter R_N by the inverse of the angular coefficient of the linear regression line, with the corresponding error.

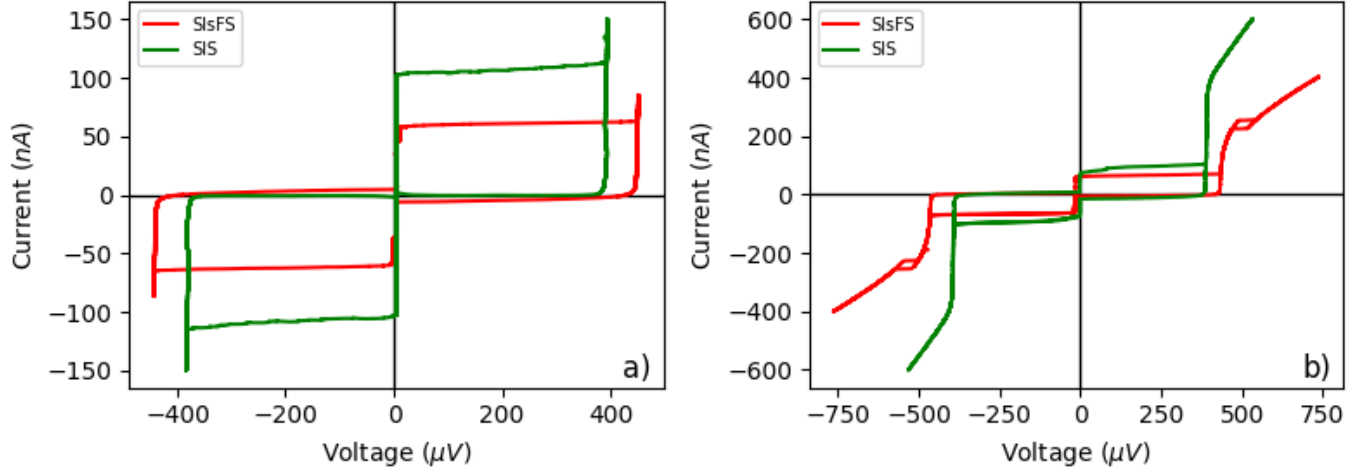


Figure 4.3: Current - Voltage characteristic at a) short range and b) long range for circular JJs with $R = 2\mu\text{m}$: Al (200 nm)/AlO_x (3 nm)/Al (400 nm) and Al (200 nm)/AlO_x (3 nm)/Al (30 nm)/Py (3 nm)/Al (400 nm).

According to the established empirical relation [132]

$$\frac{1}{C_s} \left(\frac{\text{cm}^2}{\mu\text{F}} \right) = 0.20 - 0.043 \log_{10} J_c (\text{kA}/\text{cm}^2), \quad (4.1)$$

it's possible to estimate the capacitance for all samples by multiplying the specific capacitance C_s for the junction area. This provides a geometrical estimate C of the capacitance of JJ, which allows us to calculate, by eq. 1.51, the corresponding Q factors for the samples.

$$Q = \sqrt{\frac{2eI_c R_N^2 C}{\hbar}} \quad (4.2)$$

An overview of all the parameters calculated at the temperature T_{base} is shown in Table 4.1

Table 4.1: Parameters of circular JJs Al/AlO_x/Al and Al/AlO_x/Al/Py/Al at T = T_{base}.

JJs	A (μm^2)	J_c (A/cm ²)	V_{gap} (μV)	R_N (k Ω)	$I_c R_N$ (μV)	E_J (μeV)	C (fF)	Q
SIS 19C	13	0.72 ± 0.06	390 ± 2	0.7	60 ± 2	184 ± 8	376	7
SIsFS 18C	13	0.48 ± 0.04	449 ± 15	1.4	90 ± 3	134 ± 4	367	12
SIsFS 23B	7	0.36 ± 0.03	449 ± 5	2.6	70 ± 3	55 ± 2	202	11

The values of the Q factor indicate that all junctions are in the undamped regime: a more accurate estimate of this parameter is derived at the end of this chapter.

Typical conductances and I-V curves for SIS and SIsFS junctions at T = 10 mK are shown in Figures 4.4. The critical current density was derived for both junctions. The tunnel junction was found to have $J_c = (0.31 \pm 0.03)\text{A}/\text{cm}^2$, the ferromagnetic one $J_c = (0.33 \pm 0.03)\text{A}/\text{cm}^2$. These values demonstrate consistency with each other as the discrepancy between them is lower than measurement error. This result indicates almost independence of the critical current density from the junction area.

SIsS JJs shows the high-quality of the tunnel barrier that is evident from the shape of the subgap branch. In ref [10] and this behavior has been described in the frame of the TJM model. By fitting the I-V characteristics in Fig. 4.4 a) with the TJM model, it has been estimated a subgap resistance R_{sg} of the order of a few $M\Omega$ for both the SIS JJs. Since the normal resistance of the I-V characteristic reported in Figure 4.4 a) is $R_N = (1.70 \pm 0.03)\text{k}\Omega$, the ratio R_N/R_{sg} is about 10^{-3} . This estimation is in agreement with the very low values of the measured leakage currents, lower than 0.5 nA, which is the resolution limit of the experimental setup [99]. The R_{sg} values are in the same order of magnitude as those of conventional SIS junctions, which are commonly used as components in quantum circuits [133]. The subgap resistance of the I-V characteristic reported, referred to instead in figure (b), was evaluated experimentally from the graph and found to be of the order of $10^5\Omega$, which is exactly the inverse of the conductance. SIsFS (fig. 4.4 b)) shows normal resistance of the order of $(1.14 \pm 0.02)\text{k}\Omega$, while the ratio R_N/R_{sg} is about 10^{-2} .

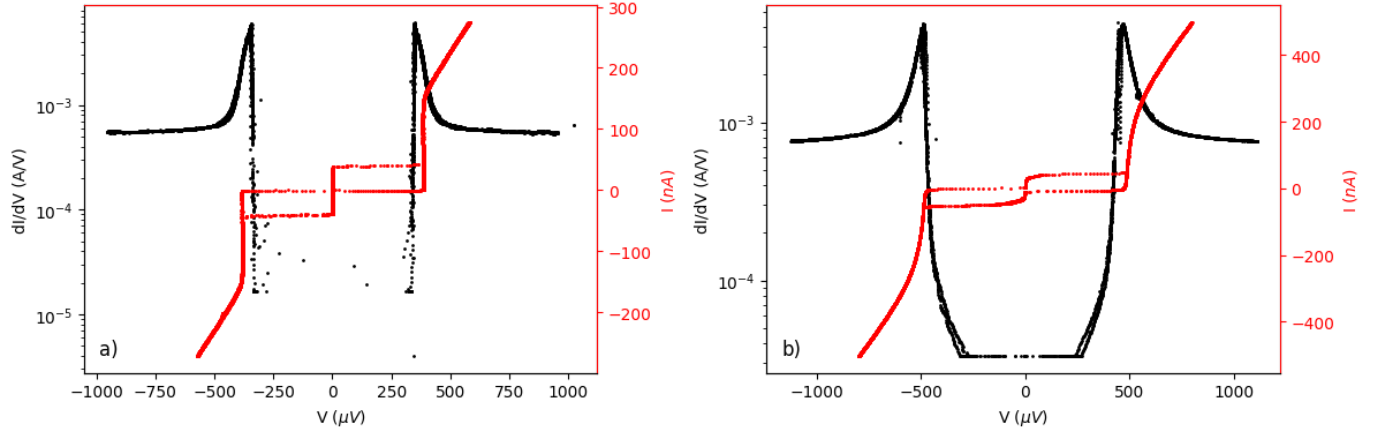


Figure 4.4: a) Conductance dI/dV measurement and I–V curve for the SIS junction with a diameter of $4\mu\text{m}$; b) conductance measurement and I–V curve for the SIFS junction with a diameter of $4\mu\text{m}$. The conductance measurements were performed by applying a magnetic field of 7.4 mT to suppress the Josephson supercurrent.

4.2 Magnetic field dependence

As explained in Section 1.3.2, the relationship between the critical current of a Josephson junction and an externally applied magnetic field reflects diffractive phenomena. This is due to the presence of an external field, H , causing a phase variation in the macroscopic wave function of bulk superconductors, with a direct impact on the critical current.

Using a current-polarized $NbTi$ superconducting coil (sec. 3.3.2), a magnetic field H orthogonal to the supercurrent flowing through the studied junctions was generated. For each of them, IV characteristics were then measured at the base temperature $T = 10\text{mK}$ as a function of the magnetic field. The $IV(H)$ measurements for the three different sets of investigated junctions are shown and discussed below. This has been found by looking at the sample IV characteristics for different values of the magnetic field sweep. After sampling the IV curves, we needed to obtain the $I_c(H)$ values for the critical current. We accomplished this by focusing solely on the superconductive section of the $IV(H)$ curves and setting two thresholds, V_- (negative) and V_+ (positive). We then evaluated the corresponding critical current values within these thresholds for the $IV(H)$ curves. Before proceeding with the magnetic measurements, it is necessary to verify that the structural parameters of the JJs are such that hysteretic behaviour can be expected. This is achieved by calculating the London penetration depth λ_L and comparing it to the interlayer's thickness d_s . Indeed, in order to realize a magnetic switching device with hysteretic behavior of the critical current, it is crucial that $d_s < \lambda_L$ [100, 104, 98]. It is possible

to find out the London penetration length by using a simplified version of Eq. (2.20) with $M_F = 0$ because there is no F layer in the chosen sample, $\Phi = \mu_0 H L d_m$, where $\mu_0 H$ represents the first minimum of the pattern. It must correspond to the magnetic flux quantum, $\Phi = \Phi_0$. L has to be replaced with the diameter of the junctions since all the samples are circular JJs, and additionally d_m represents the magnetic thickness of the sample and has a simplified expression for a tunnel JJ, $d_m = 2\lambda_L + d_I$. The dependence of I_c as a function of H at the base temperature of about $10mK$ is shown in Fig. 4.5 for a SIS JJs with diameter $D = 4\mu m$, from which the Al London penetration depth can be determined $\lambda_L \sim 39nm > d_s$. Thus, when the junction is placed in an external magnetic field, it behaves as a single junction and hysteretic behaviour of the $I_c(H)$ curves is expected. The shape of the magnetic pattern further confirms the high quality of the tunnel barrier [10].

Since the junction under investigation has a circular geometry, as reported in sec. 1.3.2, its critical current dependence on the applied magnetic field follows the Airy relation, that allows to estimate the junction parameters, like the radius and the London penetration depth λ_L . Using the relation 4.3, parameters such as $R = (2.1 \pm 0.2)\mu m$, $\lambda_L = (40 \pm 1)nm$ have been estimated and the obtained values are compatible with others found in literature [134]. Thus, the penetration lengths of London obtained by the two different methods exhibit consistency.

$$\frac{I_c}{I_{c,max}}(H; R, d) = \left| 2 \frac{J_1\left(\frac{\pi\Phi}{\Phi_0}\right)}{\frac{\pi\Phi}{\Phi_0}} \right| \quad (4.3)$$

where R corresponds to the radius of the junction, and $d = 2\lambda_L + d_I$, to the length of magnetic penetration.

Since the red fit line presented in Figure 4.5 is well adapted to the experimental data, it indicates a good uniformity of the current distribution in the junction [134]. For the first junctions with Py as the ferromagnetic layer, the magnetic field is first increased from $0mT$ to $22mT$. The external field is then swept through the range ($22mT, -22mT$) in an attempt to magnetise the ferromagnetic layer. Finally, it was returned to a value of $22mT$. No hysteresis was seen because the strength of the magnetic field was not sufficient to magnetize the ferromagnet. The position of the maximum does not shift.

At this point, the field was switched off and the temperature was raised above the critical temperature of aluminium ($\sim 1.2K$). This high temperature is needed to ensure that the aluminium is no longer a superconductor and that the the magnetic field can magnetise the F layer and no magnetic flux gets trapped in any of the S layers. As a result, the coil is supplied with a current of $45mT$ via Keithley 2400 Source Meter, then the field is switched off again and the base temperature is reached. To ensure that there is a shift in the critical current after magnetisation of the F-layer, the field is manually adjusted to $-22mT$. Thus, up ($-22mT, 22mT$) and down ($22mT, -22mT$) curves were acquired. In a similar manner, magnetisation was carried out on the negative side. So the field was switched off, the temperature

was raised to $1.6K$, to apply a magnetic field by giving a bias current of $-45mT$ to the coil, and then the field was switched off again. At $T \sim 20mK$, a magnetic field of $22mT$ was applied manually and up and down curves were acquired.

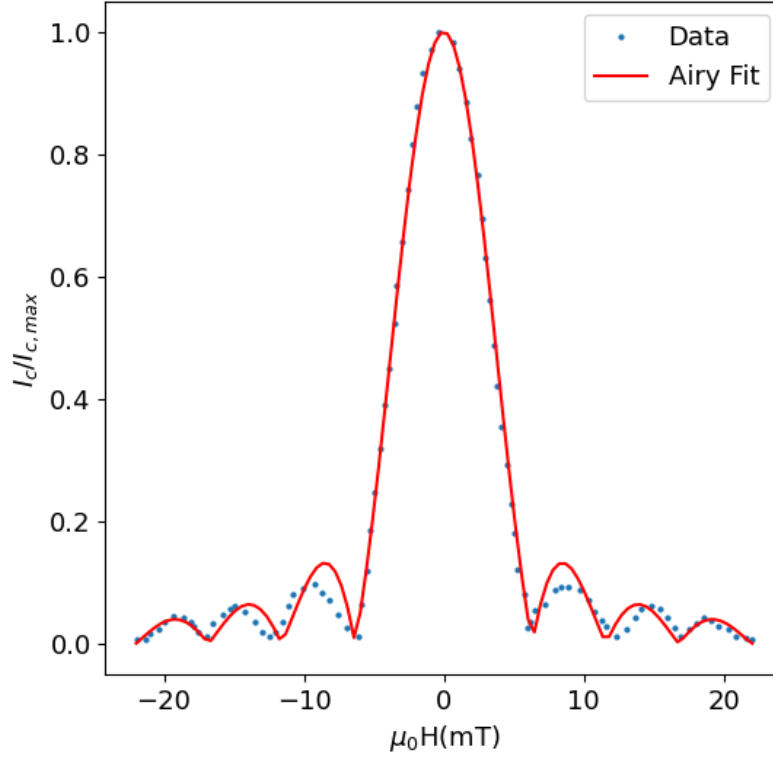


Figure 4.5: The scattered points represent the experimental data of $I_c(H)$ characteristic for a circular ($R = 2\mu m$) Josephson junction of the SIS type: Al(200nm)/AlO_x(3 nm)/Al(400nm) while red line represents the curve predicted by Airy model.

Magnetic field measurements were taken for the subsequent set of measurements, in which the ferromagnetic layer is Ni₈₅Fe₁₂Gd₃. Therefore fig. 4.6 shows $I_c(H)$ curves for Al (200 nm)/AlO_x (3 nm)/Al (30 nm)/Py-Gd (3 nm)/Al (400 nm) junction with a diameter of $4\mu m$. Small field sweeps from $(-5mT, 5mT)$ to $(-30mT, 30mT)$ were applied. Again, this range applied field is not sufficient to shift the maximum of the I_c curve. To do this, we supplied the coil with a current of $-45mT$ before and $45mT$ after and acquired up and down curves in a magnetic field range between $-15mT$ and $15mT$. In fig. 4.6, $I_c(H)$ for the SIsFS JJ is shown in the downward direction of the magnetic field sweep (black points) and in the upward direction (red squares). Two sets of data show a distinctive shift of the absolute maximum of I_c from about 6 to $-6mT$, respectively, arising from the hysteretic reversal of the ferromagnetic barrier.

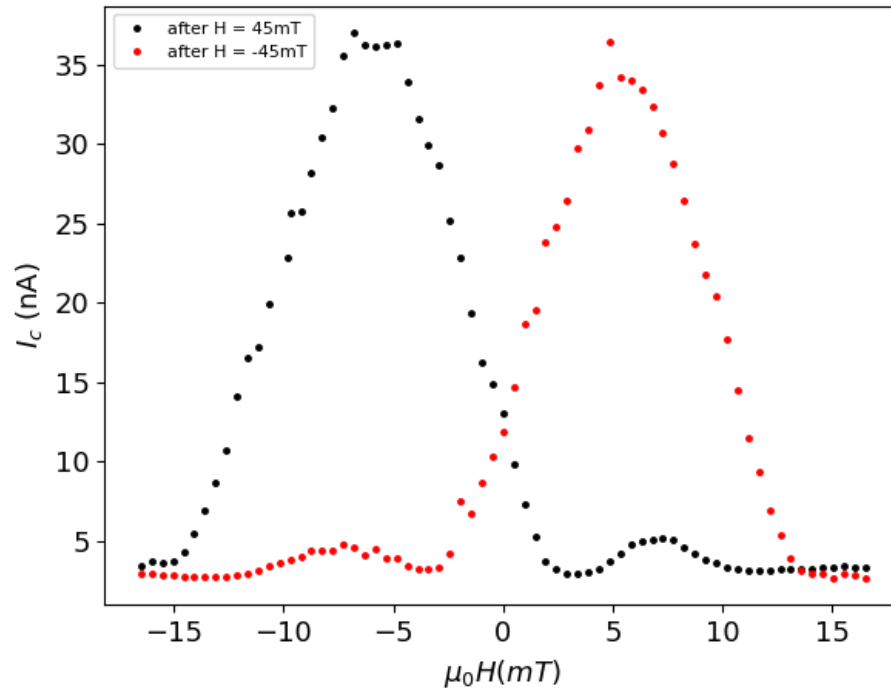


Figure 4.6: $I_c(H)$ curve for sample Al (200 nm)/AlO_x (3 nm)/Al (30 nm)/Py-Gd (3 nm)/Al (400 nm) JJs.

In the third set of measurements, Py doped not only with Gd but also with Nb was used as a ferromagnetic barrier. However, the plot of the critical current as a function of the magnetic field is the same as in Figure 4.6.

The proposed junction configuration is highly advantageous for very useful for potential applications in both classical and quantum circuits. The critical thickness L_{SC} can be defined as the minimum thickness of the s layer in an sF bilayer at a given temperature, above which superconductivity still exists [10]. As discussed earlier in the section 2.3.2, for d_s much larger than $3\xi_s$, where ξ_s is the coherence length of the superconductor, the device behaves as two Josephson junction in series, a standard tunnel junction and a metallic ferromagnetic junction. The overall properties are dominated by the junction with lower critical current, which is usually the SIs tunnel junction [127]. Thus, the transport properties [10] are determined by the SIs junction with a smaller critical current if the F-layer thickness is sufficiently small. This kind of configuration ensures easy integration of SIsFS JJs into a variety of digital and quantum circuits using standard fabrication procedures, since the F layer can be deposited subsequently without affecting the quality of the tunnel barrier. An alternative explanation for the similar behavior observed in magnetic and nonmagnetic JJs involves the Al interlayers, which are not affected by any exchange field due to a thin natural AlO_x barrier that decouples Al from the ferromagnetic layer and eliminates exchange coupling at the interface [10]. This phenomenon has been previously studied through tunneling conductance of junctions formed on

thin Al films in contact with films of the ferromagnetic semiconductors europium oxide (EuO) and europium sulfide (EuS) [10, 135, 136].

4.3 Switching current distributions (SCDs)

For a better comprehension of the phase dynamics, additional measurements were taken on the fabricated samples with regard to the switching current distributions (SCDs). The evaluation of the the distributions of probability of the switching currents from the superconducting to the finite voltage state is a powerful tool that allows a better understanding of the phase dynamics for the fabricated junctions [36]. Indeed, these measurements provide an opportunity to determine the operating regime of the fabricated junctions by estimating the Q factor.

The switching current distributions for the fabricated samples are shown, in Figures 4.7 and 4.8, for different values of temperature in the range between 0.10K and 1.10K.

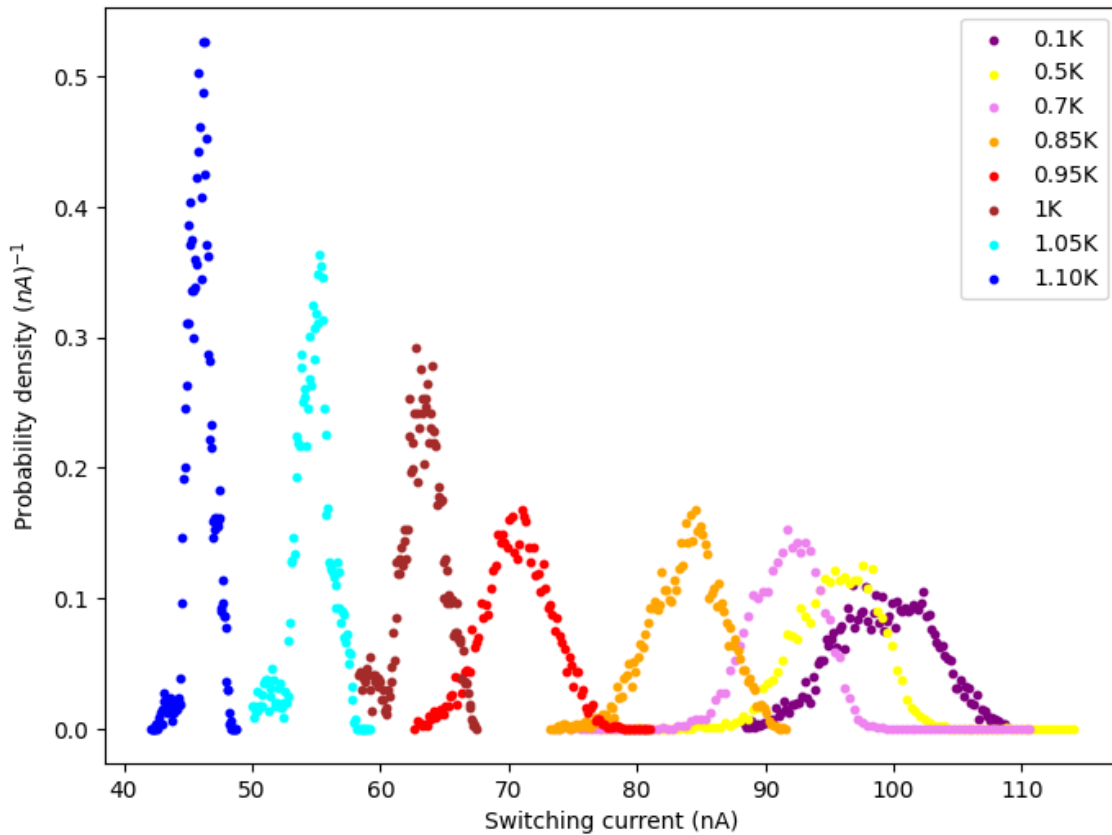


Figure 4.7: Switching current distributions for the tunnel Al/AlO_x/Al JJ.

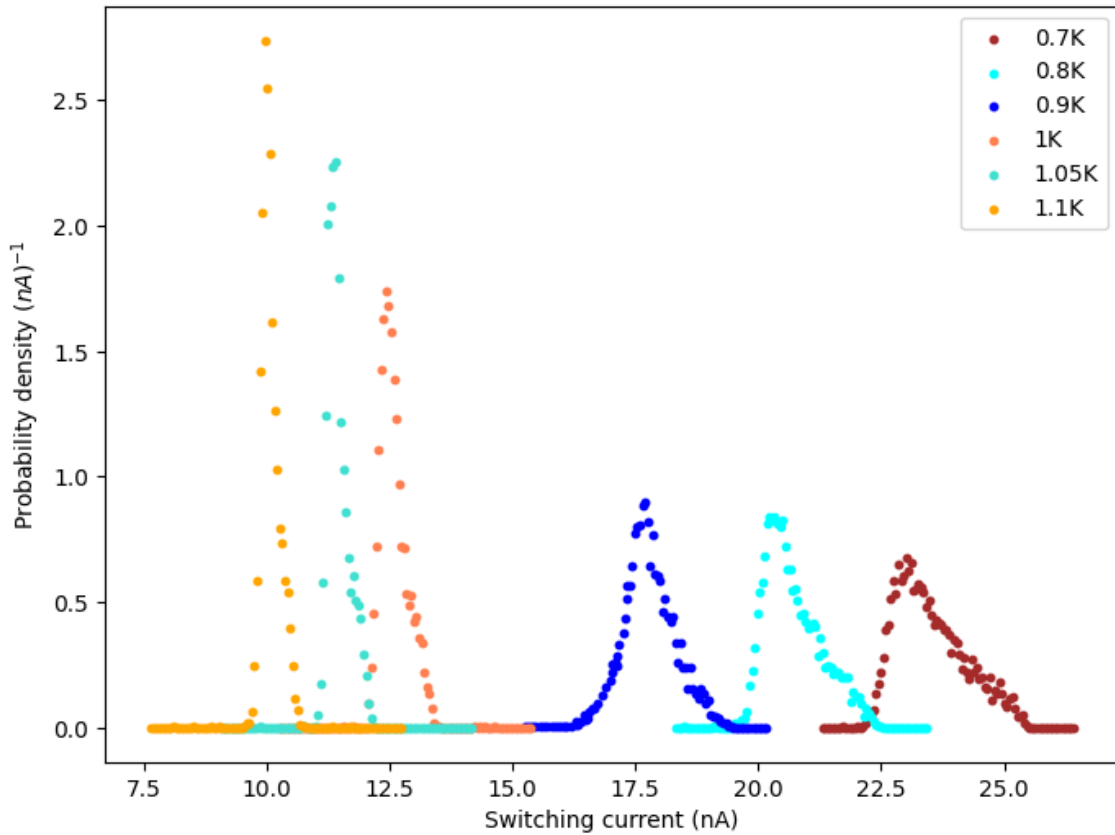


Figure 4.8: Switching current distributions for the ferromagnetic Al/AlO_x/Al/Py/Al JJ.

Differently from the low dissipation case, the SCDs broaden when lowering the T and correspondingly the peak intensity decreases [37]. This could be attributed to the phase diffusion (PD) regime.

For each considered temperature, the first moment and the standard deviation σ of the switching distributions have been calculated, and their temperature dependence, shown in Figures 4.9 and 4.10, is typical of a phase diffusion regime. Based on the measurements, it is confirmed that the standard deviation is highest at low temperatures and progressively decreases as the temperature rises.

The trend obtained for I_c as a function of temperature reproduces the standard JJ behaviour that occurs in each regime. Especially for the tunnel junction, considering that the superconducting gap decreases with increasing temperature according to the approximation BCS, the critical current follows the temperature dependence of the superconducting gap as the temperature varies according to the Ambegaokar-Baratoff relation (eq. 1.18). In fact, the critical current tends to have a constant value up to a temperature $T_c/2$ ($T_c \approx 1.3K$) and then decreases approximately for temperatures greater than $T_c/2$ until it is zero for $T \sim T_c$. This phenomenon can also be seen in the SISFS junction.

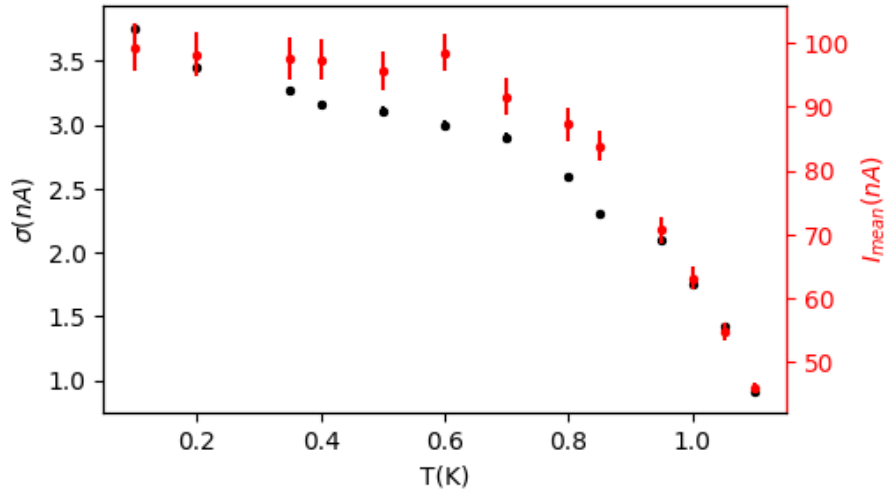


Figure 4.9: Mean switching current I_{mean} (red spheres) with error determined by formula 3.5 and standard deviation σ (black spheres) with error determined by formula 3.7 are shown as a function of T in relation to the tunnel junction Al/AIO_x/Al.

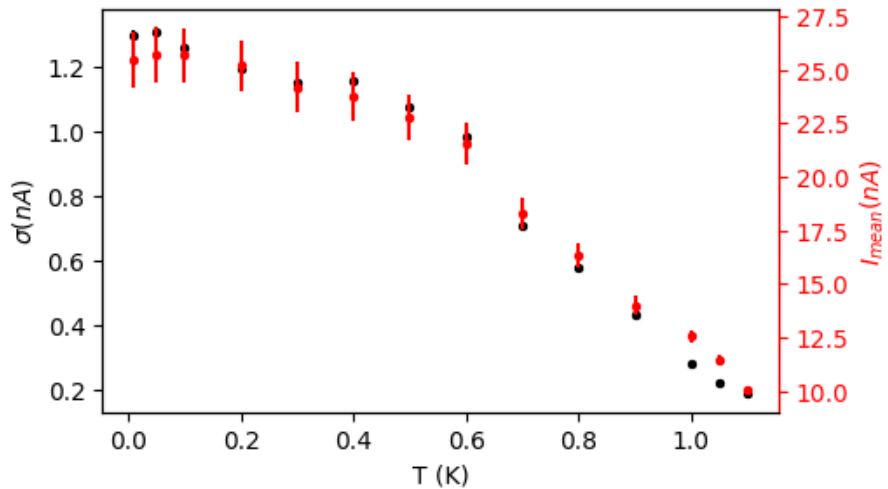


Figure 4.10: Mean switching current I_{mean} (red spheres) with error determined by formula 3.5 and standard deviation σ (black spheres) with error determined by formula 3.7 are shown as a function of T in relation to the ferromagnetic junction Al/AIO_x/Al/Py/Al.

Figures 4.11 and 4.12 shows the experimental value of the skewness γ , defined in 3.6, of the switching distributions as function of the temperature. For negative values of skewness in Figure 4.11, it is apparent that the corresponding distributions show a tail to the left (Figure 4.7). On the other hand, for values of skewness that are zero or otherwise close to zero, there is a sharper symmetrization of the distributions.

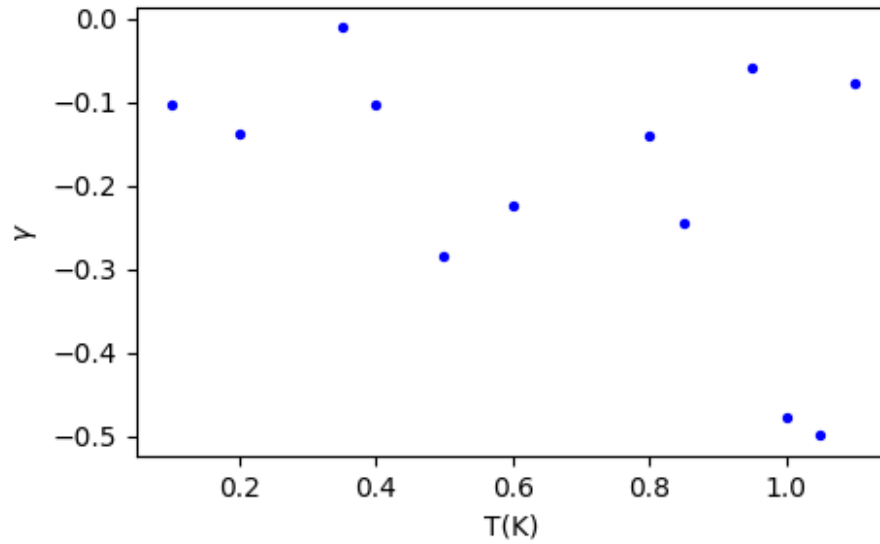


Figure 4.11: Skewness γ as a function of T for tunnel Al/AlO_x/Al JJ.

Regarding the distributions of the SISFS junctions, they have a positive skewness and thus show a tail to the right.

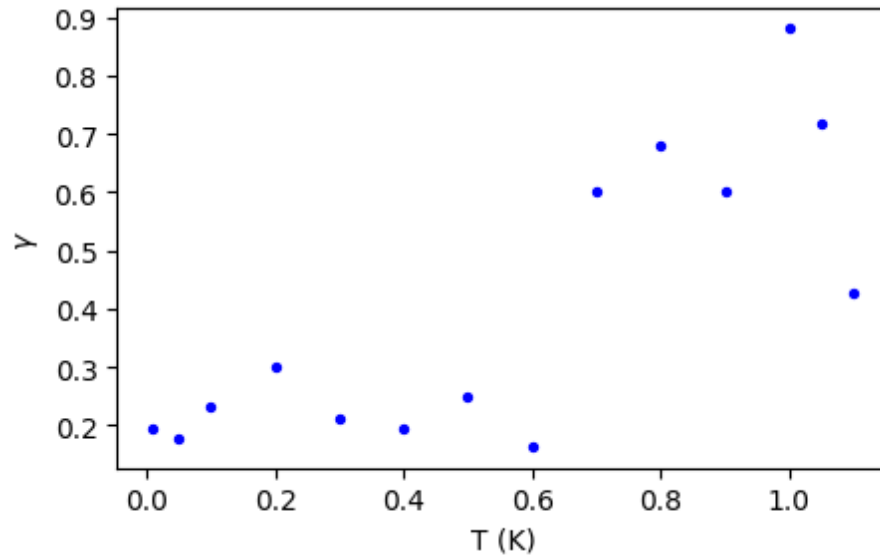


Figure 4.12: Skewness γ as a function of T for ferromagnetic Al/AlO_x/Al/Py/Al JJ.

It is observed that there is a moderately damped regime (MDR) in the considered superconducting JJs. This regime is quite distinct from the case of underdamped systems ($Q > 10$), and is common in junctions characterized by low I_c or by larger dissipation, intrinsic of the nature of the junction. In the MDR regime, the

phase dynamics is quite modified: following an event of escape, the particle may travel down the potential for a few wells and then may be retrapped in one of the following minima. A decrease of the Josephson energy E_J and of the quality factor Q enhances the retrapping rate Γ_R (eq. 1.62) causing multiple retrapping phenomena in the switching dynamics. At low bias, the process of escape and retrapping of the phase particle in the washboard potential (Figure 1.11 b)) can occur several times, producing extensive diffusion of the phase, until an increase of the tilt of the potential due to a change in the bias current increases the velocity of the particle and the junction can switch to the running state [1]. PD manifests itself as an unexpected collapse of switching current fluctuations with increasing T due to the interplay of two counteracting consequences of thermal fluctuations [137]. On one hand, thermal fluctuations assist in premature switching into the running state and, on the other hand, help in retrapping back to the superconducting state [137]. In other words, temperature does not only provide energy for excitation of a system from equilibrium state but also enhances the rate of relaxation back to the equilibrium [1].

The investigated junctions have been fabricated with the aim of being employed in a new architecture of transmon qubits [8], which requires junctions with low critical currents [138]. Typically, the main operating frequencies of transmons range from a few GHz to 10 GHz [5]. Therefore, the ratio E_J/E_c must be limited in such a way that the frequency of the qubit does not deviate from the standard range of 4-8 GHz, i.e. the microwave range [139]. This particular qubit architecture is a development of the archetypal charge qubit, the Cooper pair box [140]. Thus, since it is not a phase- or flux-oriented qubit architecture, no MQT event can be observed as the structural parameters do not allow it and the usual junctions for exploring quantum-activated effects are fabricated to have high T_{cr} values. If this condition is met, it is possible to observe quantum activated escape events in all types of junctions, from classical tunnel JJs to more exotic and unusual HTS JJs [37]. Thus, the fabricated junctions are in the PD regime, with a transition temperature $T^* \leq T_{base} = 10mK$ [141], i.e. lower than the temperatures achievable with the dilution cryostat.

Since the frequency dependent quality factor $Q(\omega) = \omega_p R(\omega) C$ is a measure of dissipation in the JJ, while the critical current I_c is an easily accessible parameter, the dissipative essence strongly depends on the value of the effective frequency dependent resistance $R(\omega)$ and of shunting capacitance C , which in turn depend on several interplaying effects, such as circuit impedance, subgap resistance and stray capacitance. Since these parameters are not easily accessible, a reliable way able to estimate the frequency dependent quality factor $Q(\omega)$ is of great interest [37]. Among other things, the SCD measurements indicate a clear PD regime, which contrasts sharply with the Q damping factors estimated in the first section of this chapter. Therefore, a more accurate determination of the damping parameters is required. Specifically, a method is needed to estimate the damping factor that does not depend on any geometrical parameter, but only on the experimental data.

For this purpose, the damping parameters can be obtained with greater precision by referring to the phase diagram displayed in Figure 4.13.

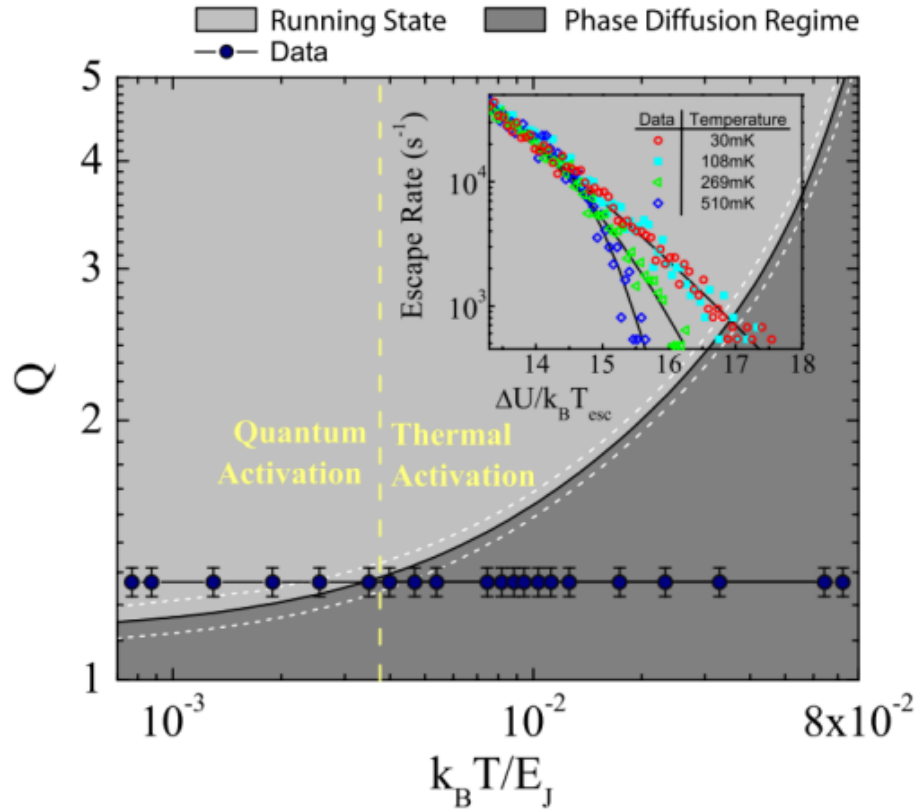


Figure 4.13: $(Q, k_B T/E_J)$ parameter space shows different regimes. The transition curve between the PD regime and the running state has been extrapolated by Monte Carlo simulations [36]. The transition curve varies depending on the ratio of $E_J/k_B T$ and the damping factor Q , resulting in a universal phase diagram that is independent of the sample [59, 1]. In the inset is shown the experimental escape rates (symbols) as function of barrier height to escape energy ratio along with the theoretical fits at different T [36].

Indeed, by calculating the $k_B T/E_J$ ratio, we were able to estimate the Q factors for the JJs by analyzing the Y-axis. These outcomes are displayed in tab. 4.2: values for the damping factor are reasonably consistent with what is expected for moderate damping.

Table 4.2: Table showing newly estimated Q values obtained by extrapolating data from Figure 4.13. These values are consistent with the junctions observed in the MDR and confirm the PD behavior of the fabricated samples

JJs	Q_0	Q_1
SIS 19C	7	1.3
SIsFS 23B	11	1.9

Q_1 values confirm that the way the phases behave in the SCDs is caused by phase diffusion.

In terms of the phase dynamics in the tilted washboard potential, the phase particle in the supercurrent branch oscillates in one well of the potential at the plasma frequency ω_p , while the voltage state involves steady motion of the phase particle ($\omega \sim 0$) [46, 9]. High-frequency, $\omega \sim \omega_p$ (usually ω_p is of the order of 10 GHz), dissipation at the switching from the superconducting to the resistive state is determined by the high-frequency damping Q_1 and is mainly affected by the environment, i.e., the circuit in which the junction is embedded [142, 9]. Low-frequency dissipation in the subgap branch of the I-V curves ($\omega \sim 0$) and the corresponding low-frequency damping Q_0 are mostly determined by the subgap resistance of the junction. The study of the electrodynamics of these junctions has therefore allowed the determination of both low-frequency and high-frequency quality factors. So, the values in tab. 4.2 represent the physical parameters of the same junction, which exhibits distinct behaviors.

Finally, after estimating the T_{cr} using formula 1.60 and utilizing Q_1 as the quality factor value, a value of $4mK$ was attained. This result confirms the lack of macroscopic quantum tunneling events in the measured junctions.

Conclusions

In this thesis, a comprehensive study has been carried out on Josephson junctions (JJ) in SIS and SIsFS configuration, based on Al technology and using Permalloy as ferromagnetic layer F. The ferromagnetic JJs were fabricated by a combination of deposition, etching and optical lithography steps, optimised in collaboration with the CNR-ISASI in Pozzuoli. Junction characterisation was performed by cryogenic magnetic transport measurements down to 10mK. The purpose of characterisation is to obtain a deeper comprehension of the physics underlying these devices, with a special focus on the dissipation of these junctions and on the control of its behavior as a function of an externally applied magnetic field. It was observed that when comparing the I-V characteristics and conductances of tunnel and SIsFS type junctions, the presence of the Py layer does not affect tunnel nature of the barrier while adding special functionalities.

The magnetic field dependence was then investigated by applying a such as magnetic field to magnetise the F-layer, which allowed us to observe a shift in the critical current maximum. The direction of this shift varied depending on the sign of the applied magnetic field. For a magnetic field of 45 mT, the maximum critical current shifted towards negative values of the field. In contrast, for a magnetic field of -45 mT, the critical current maximum shifted towards positive values. The magnetic nature of the SIsFS junction, guaranteed by the F layer, is confirmed by the hysteretic behaviour of the magnetic field pattern, while maintaining the high quality of the tunneling behaviour guaranteed by the Al oxide barrier. This technology can be extended to most ferromagnetic materials in order to develop ad hoc switchable elements, and ensures easy integration of MJJs into a wide variety of digital and quantum circuits using standard optical lithography [10]. Furthermore, the developed fabrication approach is reproducible and adaptable to a wide class of fabrication protocols, since ferromagnetic materials can be deposited ex situ without affecting the tunneling properties of the of the overall device.

The main result is the demonstration of the magnetic hysteretic behaviour of the critical current and, at the same time, the preservation of the high quality transport properties of Al tunnel junctions. These MJJs exhibit very low damping and a Josephson coupling energy value that is appropriate for integration into the ferro-transmon architecture [10, 129].

A complete low-temperature characterisation of the tunnel and ferromagnetic junc-

tions was also carried out. For future use in transmon qubit architecture, a complete characterization of the phase dynamics of such junctions using SCDs is required, as well as a reliable estimation of the junction parameters such as the critical current and the quality factor. In fact, the SCDs and their I_{mean} and standard deviation σ are unique indicators of the phase dynamics of the junctions. The characteristic collapse of σ is observed with increasing T , and the maximum amplitudes of the SCDs increase in this temperature range [1]. This leads to the SISFS JJs escape mechanism being phase diffusion (PD), which is a characteristic of a moderately damped regime (MDR). In this case, after the first escape process, the particle can be retrapped in one of the next wells and then released again, and this is visible through distinctive features in SCDs measurements [1]. Specifically, studying the PD regime provided an effective means of estimating dissipation levels in the junction. This enabled a more precise estimation of the damping factor, which was found to be greater than 1, in agreement with the MDR regime.

Bibliography

- [1] Francesco Tafuri. *Fundamentals and frontiers of the Josephson effect*. Vol. 286. Springer Nature, 2019.
- [2] P. Krantz et al. “A quantum engineer’s guide to superconducting qubits”. In: *Applied Physics Reviews* (2019). DOI: [10.1063/1.5089550](https://doi.org/10.1063/1.5089550). URL: <https://doi.org/10.1063/1.5089550>.
- [3] Erik Lucero et al. “Computing prime factors with a Josephson phase qubit quantum”. In: *Nature Physics* (2012). DOI: [10.1007/BF02650179](https://doi.org/10.1007/BF02650179). URL: <https://doi.org/10.1007/BF02650179>.
- [4] Richard P. Feynman. “Simulating physics with computers”. In: *International Journal of Theoretical Physics* (1982). DOI: [10.1007/BF02650179](https://doi.org/10.1007/BF02650179). URL: <https://doi.org/10.1007/BF02650179>.
- [5] Thomas E. Roth et al. “An Introduction to the Transmon Qubit for Electromagnetic Engineers”. In: (2021). arXiv: [2106.11352](https://arxiv.org/abs/2106.11352) [quant-ph].
- [6] D. Rosenberg et al. “3D integrated superconducting qubits”. In: *npj Quantum Information* (2017). DOI: [10.1038/s41534-017-0044-0](https://dx.doi.org/10.1038/s41534-017-0044-0). URL: <http://dx.doi.org/10.1038/s41534-017-0044-0>.
- [7] Ramón Aguado. “A perspective on semiconductor-based superconducting qubits”. In: *Applied Physics Letters* (2020). DOI: [10.1063/5.0024124](https://pubs.aip.org/aip/apl/article-pdf/doi/10.1063/5.0024124/13863017/240501_1_online.pdf). eprint: https://pubs.aip.org/aip/apl/article-pdf/doi/10.1063/5.0024124/13863017/240501_1_online.pdf. URL: <https://doi.org/10.1063/5.0024124>.
- [8] Halima Giovanna Ahmad et al. “Hybrid ferromagnetic transmon qubit: Circuit design, feasibility, and detection protocols for magnetic fluctuations”. In: *Phys. Rev. B* 105 (21 2022), p. 214522. DOI: [10.1103/PhysRevB.105.214522](https://link.aps.org/doi/10.1103/PhysRevB.105.214522). URL: <https://link.aps.org/doi/10.1103/PhysRevB.105.214522>.
- [9] H.G. Ahmad et al. “Electrodynamics of Highly Spin-Polarized Tunnel Josephson Junctions”. In: *Phys. Rev. Appl.* 13 (1 Jan. 2020), p. 014017. DOI: [10.1103/PhysRevApplied.13.014017](https://link.aps.org/doi/10.1103/PhysRevApplied.13.014017). URL: <https://link.aps.org/doi/10.1103/PhysRevApplied.13.014017>.

-
- [10] A. Vettoliere et al. “Aluminum-ferromagnetic Josephson tunnel junctions for high quality magnetic switching devices”. In: *Applied Physics Letters* 120.26 (2022), p. 262601. ISSN: 0003-6951. DOI: [10.1063/5.0101686](https://doi.org/10.1063/5.0101686). eprint: https://pubs.aip.org/aip/apl/article-pdf/doi/10.1063/5.0101686/16450324/262601\1\1_online.pdf. URL: <https://doi.org/10.1063/5.0101686>.
- [11] Loredana Parlato et al. “Characterization of scalable Josephson memory element containing a strong ferromagnet”. In: *Journal of Applied Physics* 127.19 (2020). DOI: [10.1063/5.0004554](https://doi.org/10.1063/5.0004554). eprint: https://pubs.aip.org/aip/jap/article-pdf/doi/10.1063/5.0004554/15244693/193901\1\1_online.pdf. URL: <https://doi.org/10.1063/5.0004554>.
- [12] Kristian Fossheim and Asle Sudbø. *Superconductivity: physics and applications*. John Wiley & Sons, 2004.
- [13] Fritz London and Heinz London. “The electromagnetic equations of the supraconductor”. In: *Proceedings of The Royal Society A: Mathematical, Physical and Engineering Sciences* 149 (1935), pp. 71–88. URL: <https://api.semanticscholar.org/CorpusID:122556407>.
- [14] W. Meissner and R. Ochsenfeld. “Ein neuer Effekt bei Eintritt der Supraleitfähigkeit”. In: *Naturwissenschaften* (1933). DOI: [10.1007/BF01504252](https://doi.org/10.1007/BF01504252). URL: <https://doi.org/10.1007/BF01504252>.
- [15] Michael Tinkham. *Introduction to superconductivity*. Courier Corporation, 2004.
- [16] V. V. Val’kov and A. O. Zlotnikov. “Microscopic Derivation of the Ginzburg–Landau Equations for the Periodic Anderson Model in the Coexistence Phase of Superconductivity and Antiferromagnetism”. In: *Journal of Low Temperature Physics* 185.5–6 (2016), pp. 439–445. ISSN: 1573-7357. DOI: [10.1007/s10909-015-1410-y](https://doi.org/10.1007/s10909-015-1410-y). URL: <http://dx.doi.org/10.1007/s10909-015-1410-y>.
- [17] Antonio Barone, Gianfranco Paternò, et al. *Physics and applications of the Josephson effect*. 1982.
- [18] Giuseppe Grosso and Giuseppe Pastori Parravicini. *Solid state physics*. Academic press, 2013.
- [19] Sidney Shapiro. “Josephson Currents in Superconducting Tunneling: The Effect of Microwaves and Other Observations”. In: *Phys. Rev. Lett.* 11 (2 July 1963), pp. 80–82. DOI: [10.1103/PhysRevLett.11.80](https://doi.org/10.1103/PhysRevLett.11.80). URL: <https://link.aps.org/doi/10.1103/PhysRevLett.11.80>.
- [20] Vinay Ambegaokar and Alexis Baratoff. “Tunneling Between Superconductors”. In: *Phys. Rev. Lett.* 10 (11 June 1963), pp. 486–489. DOI: [10.1103/PhysRevLett.10.486](https://doi.org/10.1103/PhysRevLett.10.486). URL: <https://link.aps.org/doi/10.1103/PhysRevLett.10.486>.

- [21] G Wild et al. “Josephson coupling and Fiske dynamics in ferromagnetic tunnel junctions”. In: *The European Physical Journal B* 78.4 (2010), pp. 509–523.
- [22] Halima Giovanna Ahmad. “Physics of the Josephson effect in junctions with ferromagnetic barriers towards quantum circuits and RF applications”. PhD thesis. 2021.
- [23] Rudolf Gross and Achim Marx. *Applied Superconductivity : Josephson Effect and Superconducting Electronics*. 2009. URL: <https://api.semanticscholar.org/CorpusID:40822874>.
- [24] W. C. Scott. “HYSTERESIS IN THE dc SWITCHING CHARACTERISTICS OF JOSEPHSON JUNCTIONS”. In: *Applied Physics Letters* 17.4 (Oct. 2003), pp. 166–169. DOI: [10.1063/1.1653350](https://doi.org/10.1063/1.1653350). eprint: https://pubs.aip.org/aip/apl/article-pdf/17/4/166/7728915/166_1_online.pdf. URL: <https://doi.org/10.1063/1.1653350>.
- [25] N.F. Pedersen and K. Saermark. “Analytical solution for a Josephson-Junction model with capacitance”. In: *Physica* 69 (1973). DOI: [https://doi.org/10.1016/0031-8914\(73\)90089-X](https://doi.org/10.1016/0031-8914(73)90089-X). URL: <https://www.sciencedirect.com/science/article/pii/003189147390089X>.
- [26] N. R. Werthamer. “Nonlinear Self-Coupling of Josephson Radiation in Superconducting Tunnel Junctions”. In: *Phys. Rev.* 147 (1 July 1966), pp. 255–263. DOI: [10.1103/PhysRev.147.255](https://doi.org/10.1103/PhysRev.147.255). URL: <https://link.aps.org/doi/10.1103/PhysRev.147.255>.
- [27] Konstantin K Likharev. *Dynamics of Josephson junctions and circuits*. Routledge, 2022.
- [28] J. R. Kirtley et al. “Measurement of the Intrinsic Subgap Dissipation in Josephson Junctions”. In: *Phys. Rev. Lett.* 61 (20 Nov. 1988), pp. 2372–2375. DOI: [10.1103/PhysRevLett.61.2372](https://doi.org/10.1103/PhysRevLett.61.2372). URL: <https://link.aps.org/doi/10.1103/PhysRevLett.61.2372>.
- [29] R. Cristiano et al. “The effective dissipation in Nb/AlO_x/Nb Josephson tunnel junctions by return current measurements”. In: *Journal of Applied Physics* 81.11 (1997), pp. 7418–7426. ISSN: 0021-8979. DOI: [10.1063/1.365282](https://doi.org/10.1063/1.365282). eprint: https://pubs.aip.org/aip/jap/article-pdf/81/11/7418/10582105/7418_1_online.pdf. URL: <https://doi.org/10.1063/1.365282>.
- [30] K. Serniak et al. “Hot Nonequilibrium Quasiparticles in Transmon Qubits”. In: *Physical Review Letters* 121.15 (Oct. 2018). DOI: [10.1103/physrevlett.121.157701](https://doi.org/10.1103/physrevlett.121.157701). URL: <https://doi.org/10.1103%2Fphysrevlett.121.157701>.

-
- [31] Alexander Bilmes et al. “Resolving the positions of defects in superconducting quantum bits”. In: *Scientific Reports* 10 (2020). DOI: [10.1038/s41598-020-59749-y](https://doi.org/10.1038/s41598-020-59749-y).
- [32] Alessio Rettaroli. “Study of devices based on Josephson junctions for galactic axion search”. PhD thesis. PhD Thesis, Università degli Studi Roma Tre, 2021.
- [33] YC Chen, Matthew PA Fisher, and AJ Leggett. “The return of a hysteretic Josephson junction to the zero-voltage state: I-V characteristic and quantum retrapping”. In: *Journal of applied physics* 64.6 (1988), pp. 3119–3142.
- [34] W. J. Johnson. “Non linear propagation on superconducting tunneling junctions.” PhD thesis. PhD Thesis, Madison: University of Wisconsin, 1968.
- [35] T. A. Fulton and L. N. Dunkleberger. “Lifetime of the zero-voltage state in Josephson tunnel junctions”. In: *Phys. Rev. B* 9 (11 June 1974), pp. 4760–4768. DOI: [10.1103/PhysRevB.9.4760](https://doi.org/10.1103/PhysRevB.9.4760). URL: <https://link.aps.org/doi/10.1103/PhysRevB.9.4760>.
- [36] Luigi Longobardi et al. “Direct Transition from Quantum Escape to a Phase Diffusion Regime in YBaCuO Biepitaxial Josephson Junctions”. In: *Phys. Rev. Lett.* 109 (5 Aug. 2012), p. 050601. DOI: [10.1103/PhysRevLett.109.050601](https://doi.org/10.1103/PhysRevLett.109.050601). URL: <https://link.aps.org/doi/10.1103/PhysRevLett.109.050601>.
- [37] Davide Massarotti et al. “Escape dynamics in moderately damped Josephson junctions”. In: *Low Temperature Physics* 38.4 (2012), pp. 263–272.
- [38] M. Büttiker, E. P. Harris, and R. Landauer. “Thermal activation in extremely underdamped Josephson-junction circuits”. In: *Phys. Rev. B* 28 (3 Aug. 1983), pp. 1268–1275. DOI: [10.1103/PhysRevB.28.1268](https://doi.org/10.1103/PhysRevB.28.1268). URL: <https://link.aps.org/doi/10.1103/PhysRevB.28.1268>.
- [39] Michel H. Devoret, John M. Martinis, and John Clarke. “Measurements of Macroscopic Quantum Tunneling out of the Zero-Voltage State of a Current-Biased Josephson Junction”. In: *Phys. Rev. Lett.* 55 (18 Oct. 1985), pp. 1908–1911. DOI: [10.1103/PhysRevLett.55.1908](https://doi.org/10.1103/PhysRevLett.55.1908). URL: <https://link.aps.org/doi/10.1103/PhysRevLett.55.1908>.
- [40] Luigi Longobardi et al. “Effects of Capacitance on Phase Dynamics of YBa₂Cu₃O_{7-x} Josephson Junctions”. In: *IEEE Transactions on Applied Superconductivity* 25.3 (2015), pp. 1–5. DOI: [10.1109/TASC.2014.2375854](https://doi.org/10.1109/TASC.2014.2375854).
- [41] Hermann Grabert, Peter Olschowski, and Ulrich Weiss. “Quantum decay rates for dissipative systems at finite temperatures”. In: *Phys. Rev. B* 36 (4 Aug. 1987), pp. 1931–1951. DOI: [10.1103/PhysRevB.36.1931](https://doi.org/10.1103/PhysRevB.36.1931). URL: <https://link.aps.org/doi/10.1103/PhysRevB.36.1931>.

- [42] H.Devoret M.Martinis and J.Clarke. “Experimental tests for the quantum behaviour of a macroscopic degree of freedom: The phase difference across a Josephson junction”. In: *Physical Review B* (1987).
- [43] John M. Martinis, Michel H. Devoret, and John Clarke. “Energy-Level Quantization in the Zero-Voltage State of a Current-Biased Josephson Junction”. In: *Phys. Rev. Lett.* 55 (15 Oct. 1985), pp. 1543–1546. DOI: [10.1103/PhysRevLett.55.1543](https://doi.org/10.1103/PhysRevLett.55.1543). URL: <https://link.aps.org/doi/10.1103/PhysRevLett.55.1543>.
- [44] JC Fenton and PA Warburton. “Monte Carlo simulations of thermal fluctuations in moderately damped Josephson junctions: Multiple escape and retrapping, switching-and return-current distributions, and hysteresis”. In: *Physical Review B* 78.5 (2008), p. 054526.
- [45] Luca Galletti, Francesco Tafuri, and Floriana Lombardi. “Coherence Effects in Superconducting Hybrid Devices”. PhD thesis. PhD Thesis, Università degli Studi di Napoli Federico II, 2014.
- [46] R. L. Kautz and John M. Martinis. “Noise-affected I-V curves in small hysteretic Josephson junctions”. In: *Phys. Rev. B* 42 (16 Dec. 1990), pp. 9903–9937. DOI: [10.1103/PhysRevB.42.9903](https://doi.org/10.1103/PhysRevB.42.9903). URL: <https://link.aps.org/doi/10.1103/PhysRevB.42.9903>.
- [47] John M Martinis and Richard L Kautz. “Classical phase diffusion in small hysteretic Josephson junctions”. In: *Physical review letters* 63.14 (1989), p. 1507.
- [48] E. Ben-Jacob, D. J. Bergman, B. J. Matkowsky, and Z. Schuss. “Lifetime of oscillatory steady states”. In: *Phys. Rev. A* 26 (5 Nov. 1982), pp. 2805–2816. DOI: [10.1103/PhysRevA.26.2805](https://doi.org/10.1103/PhysRevA.26.2805). URL: <https://link.aps.org/doi/10.1103/PhysRevA.26.2805>.
- [49] D Massarotti et al. “Study of Phase Dynamics in Moderately Damped Josephson Junctions”. In: *Journal of superconductivity and novel magnetism* 26 (2013), pp. 835–838.
- [50] Davide Massarotti et al. “Macroscopic quantum tunneling and retrapping processes in moderately damped YBaCuO Josephson junctions”. In: *Low Temperature Physics* 39.3 (2013), pp. 294–298.
- [51] Morten Kjaergaard et al. “Superconducting Qubits: Current State of Play”. In: *Annual Review of Condensed Matter Physics* (2020). DOI: [10.1146/annurev-conmatphys-031119-050605](https://doi.org/10.1146/annurev-conmatphys-031119-050605). URL: <https://doi.org/10.1146/annurev-conmatphys-031119-050605>.
- [52] Joel I-Jan Wang et al. “Coherent control of a hybrid superconducting circuit made with graphene-based van der Waals heterostructures”. In: *Nature Nanotechnology* (2019). DOI: [10.1038/s41565-018-0329-2](https://doi.org/10.1038/s41565-018-0329-2). URL: <https://doi.org/10.1038/s41565-018-0329-2>.

-
- [53] Jens Koch et al. “Charge-insensitive qubit design derived from the Cooper pair box”. In: *Phys. Rev. A* (2007). DOI: [10.1103/PhysRevA.76.042319](https://doi.org/10.1103/PhysRevA.76.042319). URL: <https://link.aps.org/doi/10.1103/PhysRevA.76.042319>.
- [54] C. Barthel et al. “Rapid Single-Shot Measurement of a Singlet-Triplet Qubit”. In: *Phys. Rev. Lett.* (2009). DOI: [10.1103/PhysRevLett.103.160503](https://doi.org/10.1103/PhysRevLett.103.160503). URL: <https://link.aps.org/doi/10.1103/PhysRevLett.103.160503>.
- [55] Gunta Kunakova et al. “Topological insulator nanoribbon Josephson junctions: Evidence for size effects in transport properties”. In: *Journal of Applied Physics* (2020). URL: <https://api.semanticscholar.org/CorpusID:226290123>.
- [56] G. de Lange et al. “Realization of Microwave Quantum Circuits Using Hybrid Superconducting-Semiconducting Nanowire Josephson Elements”. In: *Phys. Rev. Lett.* (2015). DOI: [10.1103/PhysRevLett.115.127002](https://doi.org/10.1103/PhysRevLett.115.127002). URL: <https://link.aps.org/doi/10.1103/PhysRevLett.115.127002>.
- [57] R. Caruso et al. “RF assisted switching in magnetic Josephson junctions”. In: *Journal of Applied Physics* 123.13 (Apr. 2018), p. 133901. ISSN: 0021-8979. DOI: [10.1063/1.5018854](https://doi.org/10.1063/1.5018854). eprint: https://pubs.aip.org/aip/jap/article-pdf/doi/10.1063/1.5018854/13972299/133901_1_online.pdf. URL: <https://doi.org/10.1063/1.5018854>.
- [58] Halima Giovanna Ahmad et al. “Coexistence and tuning of spin-singlet and triplet transport in spin-filter Josephson junctions”. In: *Communications Physics* (2022). DOI: [10.1038/s42005-021-00783-1](https://doi.org/10.1038/s42005-021-00783-1). URL: <https://doi.org/10.1038/s42005-021-00783-1>.
- [59] Davide Massarotti et al. “Macroscopic quantum tunnelling in spin filter ferromagnetic Josephson junctions”. In: *Nature Communications* 6 (2015). URL: <https://api.semanticscholar.org/CorpusID:8477836>.
- [60] M. Weides. “Magnetic anisotropy in ferromagnetic Josephson junctions”. In: *Applied Physics Letters* 93.5 (Aug. 2008). DOI: [10.1063/1.2967873](https://doi.org/10.1063/1.2967873). URL: <https://doi.org/10.1063/1.2967873>.
- [61] Halima Giovanna Ahmad. “Master Thesis: Physics of the Josephson effect in junctions with ferromagnetic barriers.” In: ().
- [62] Charles Kittel. *Introduction to solid state physics / by Charles Kittel*. 4th ed. Wiley, 1971.
- [63] M. Alagiri, C. Muthamizhchelvan, and S. Ponnusamy. “Structural and magnetic properties of iron, cobalt and nickel nanoparticles”. In: *Synthetic Metals* (2011). DOI: <https://doi.org/10.1016/j.synthmet.2011.05.030>. URL: <https://www.sciencedirect.com/science/article/pii/S0379677911002268>.
- [64] Sōshin Chikazumi. *Physics of ferromagnetism*. 94. Oxford university press, 1997.

- [65] Bernard Dennis Cullity and Chad D Graham. *Introduction to magnetic materials*. John Wiley & Sons, 2011.
- [66] Stephen Blundell. *Magnetism in condensed matter*. OUP Oxford, 2001.
- [67] Roberta Satariano. “Magnetic tunnel Josephson Junctions towards hybrid quantum architectures”. PhD thesis.
- [68] S. Guéron et al. “Superconducting Proximity Effect Probed on a Mesoscopic Length Scale”. In: *Phys. Rev. Lett.* 77 (14 Sept. 1996), pp. 3025–3028. DOI: [10.1103/PhysRevLett.77.3025](https://doi.org/10.1103/PhysRevLett.77.3025). URL: <https://link.aps.org/doi/10.1103/PhysRevLett.77.3025>.
- [69] K. K. Likharev. “Superconducting weak links”. In: *Rev. Mod. Phys.* 51 (1 Jan. 1979), pp. 101–159. DOI: [10.1103/RevModPhys.51.101](https://doi.org/10.1103/RevModPhys.51.101). URL: <https://link.aps.org/doi/10.1103/RevModPhys.51.101>.
- [70] G Deutscher and P G de Gennes. “PROXIMITY EFFECTS.” In: *pp 1005-34 of Superconductivity. Vols. 1 and 2. Parks, R. D. (ed.). New York, Marcel Dekker, Inc., 1969.* (1969). URL: <https://www.osti.gov/biblio/4842932>.
- [71] A. A. Golubov, M. Yu. Kupriyanov, and E. Il’ichev. “The current-phase relation in Josephson junctions”. In: *Rev. Mod. Phys.* 76 (2 Apr. 2004), pp. 411–469. DOI: [10.1103/RevModPhys.76.411](https://doi.org/10.1103/RevModPhys.76.411). URL: <https://link.aps.org/doi/10.1103/RevModPhys.76.411>.
- [72] K A Delin and A W Kleinsasser. “Stationary properties of high-critical-temperature proximity effect Josephson junctions”. In: *Superconductor Science and Technology* 9.4 (Apr. 1996), p. 227. DOI: [10.1088/0953-2048/9/4/001](https://doi.org/10.1088/0953-2048/9/4/001). URL: <https://dx.doi.org/10.1088/0953-2048/9/4/001>.
- [73] A. I. Buzdin. “Proximity effects in superconductor-ferromagnet heterostructures”. In: *Rev. Mod. Phys.* 77 (3 Sept. 2005), pp. 935–976. DOI: [10.1103/RevModPhys.77.935](https://doi.org/10.1103/RevModPhys.77.935). URL: <https://link.aps.org/doi/10.1103/RevModPhys.77.935>.
- [74] V. V. Ryazanov et al. “Coupling of Two Superconductors through a Ferromagnet: Evidence for a π Junction”. In: *Phys. Rev. Lett.* 86 (11 Mar. 2001), pp. 2427–2430. DOI: [10.1103/PhysRevLett.86.2427](https://doi.org/10.1103/PhysRevLett.86.2427). URL: <https://link.aps.org/doi/10.1103/PhysRevLett.86.2427>.
- [75] M. J. M. de Jong and C. W. J. Beenakker. “Andreev Reflection in Ferromagnet-Superconductor Junctions”. In: *Phys. Rev. Lett.* 74 (9 Feb. 1995), pp. 1657–1660. DOI: [10.1103/PhysRevLett.74.1657](https://doi.org/10.1103/PhysRevLett.74.1657). URL: <https://link.aps.org/doi/10.1103/PhysRevLett.74.1657>.
- [76] A I Larkin and Yu N Ovchinnikov. “NONUNIFORM STATE OF SUPERCONDUCTORS”. In: *Zh. Eksperim. i Teor. Fiz.* 47 (Sept. 1964). URL: <https://www.osti.gov/biblio/4653415>.

-
- [77] Peter Fulde and Richard A. Ferrell. “Superconductivity in a Strong Spin-Exchange Field”. In: *Phys. Rev.* 135 (3A Aug. 1964), A550–A563. DOI: [10.1103/PhysRev.135.A550](https://doi.org/10.1103/PhysRev.135.A550). URL: <https://link.aps.org/doi/10.1103/PhysRev.135.A550>.
- [78] A. Buzdin and I. Baladié. “Theoretical description of ferromagnetic π junctions near the critical temperature”. In: *Phys. Rev. B* 67 (18 May 2003), p. 184519. DOI: [10.1103/PhysRevB.67.184519](https://doi.org/10.1103/PhysRevB.67.184519). URL: <https://link.aps.org/doi/10.1103/PhysRevB.67.184519>.
- [79] L.N. Bulaevskii et al. “On possibility of the spontaneous magnetic flux in a Josephson junction containing magnetic impurities”. In: *Solid State Communications* 25.12 (1978), pp. 1053–1057. ISSN: 0038-1098. DOI: [https://doi.org/10.1016/0038-1098\(78\)90906-7](https://doi.org/10.1016/0038-1098(78)90906-7). URL: <https://www.sciencedirect.com/science/article/pii/0038109878909067>.
- [80] L.N. Bulaevskii et al. “Coexistence of ferromagnetism and superconductivity in ErRh₄B₄ and HoMo₆S₈: Exchange or electromagnetic mechanism?” In: *Physics Letters A* 89.2 (1982), pp. 93–95. ISSN: 0375-9601. DOI: [https://doi.org/10.1016/0375-9601\(82\)90514-X](https://doi.org/10.1016/0375-9601(82)90514-X). URL: <https://www.sciencedirect.com/science/article/pii/037596018290514X>.
- [81] S. M. Frolov et al. “Measurement of the current-phase relation of superconductor/ferromagnet/superconductor π Josephson junctions”. In: *Phys. Rev. B* 70 (14 Oct. 2004), p. 144505. DOI: [10.1103/PhysRevB.70.144505](https://doi.org/10.1103/PhysRevB.70.144505). URL: <https://link.aps.org/doi/10.1103/PhysRevB.70.144505>.
- [82] L.N. Bulaevskii, V.V. Kuzii, and A.A. Sobyenin. “On possibility of the spontaneous magnetic flux in a Josephson junction containing magnetic impurities”. In: *Solid State Communications* 25.12 (1978), pp. 1053–1057. ISSN: 0038-1098. DOI: [https://doi.org/10.1016/0038-1098\(78\)90906-7](https://doi.org/10.1016/0038-1098(78)90906-7). URL: <https://www.sciencedirect.com/science/article/pii/0038109878909067>.
- [83] Hermann Sellier et al. “Half-Integer Shapiro Steps at the $0-\pi$ Crossover of a Ferromagnetic Josephson Junction”. In: *Phys. Rev. Lett.* 92 (25 June 2004), p. 257005. DOI: [10.1103/PhysRevLett.92.257005](https://doi.org/10.1103/PhysRevLett.92.257005). URL: <https://link.aps.org/doi/10.1103/PhysRevLett.92.257005>.
- [84] T. Kontos et al. “Josephson Junction through a Thin Ferromagnetic Layer: Negative Coupling”. In: *Phys. Rev. Lett.* 89 (13 Sept. 2002), p. 137007. DOI: [10.1103/PhysRevLett.89.137007](https://doi.org/10.1103/PhysRevLett.89.137007). URL: <https://link.aps.org/doi/10.1103/PhysRevLett.89.137007>.
- [85] Y. Blum, A. Tsukernik, M. Karpovski, and A. Palevski. “Oscillations of the Superconducting Critical Current in Nb-Cu-Ni-Cu-Nb Junctions”. In: *Phys. Rev. Lett.* 89 (18 Oct. 2002), p. 187004. DOI: [10.1103/PhysRevLett.89.187004](https://doi.org/10.1103/PhysRevLett.89.187004). URL: <https://link.aps.org/doi/10.1103/PhysRevLett.89.187004>.

- [86] V. A. Oboznov et al. “Thickness Dependence of the Josephson Ground States of Superconductor-Ferromagnet-Superconductor Junctions”. In: *Phys. Rev. Lett.* 96 (19 May 2006), p. 197003. DOI: [10.1103/PhysRevLett.96.197003](https://doi.org/10.1103/PhysRevLett.96.197003). URL: <https://link.aps.org/doi/10.1103/PhysRevLett.96.197003>.
- [87] J. W. A. Robinson et al. “Critical Current Oscillations in Strong Ferromagnetic π Junctions”. In: *Phys. Rev. Lett.* 97 (17 Oct. 2006), p. 177003. DOI: [10.1103/PhysRevLett.97.177003](https://doi.org/10.1103/PhysRevLett.97.177003). URL: <https://link.aps.org/doi/10.1103/PhysRevLett.97.177003>.
- [88] E. Goldobin, D. Koelle, R. Kleiner, and A. Buzdin. “Josephson junctions with second harmonic in the current-phase relation: Properties of φ junctions”. In: *Phys. Rev. B* 76 (22 Dec. 2007), p. 224523. DOI: [10.1103/PhysRevB.76.224523](https://doi.org/10.1103/PhysRevB.76.224523). URL: <https://link.aps.org/doi/10.1103/PhysRevB.76.224523>.
- [89] Z. Radović, L. Dobrosavljević-Grujić, and B. Vujičić. “Coexistence of stable and metastable 0 and π states in Josephson junctions”. In: *Phys. Rev. B* 63 (21 May 2001), p. 214512. DOI: [10.1103/PhysRevB.63.214512](https://doi.org/10.1103/PhysRevB.63.214512). URL: <https://link.aps.org/doi/10.1103/PhysRevB.63.214512>.
- [90] Z. Radović, N. Lazarides, and N. Flytzanis. “Josephson effect in double-barrier superconductor-ferromagnet junctions”. In: *Phys. Rev. B* 68 (1 July 2003), p. 014501. DOI: [10.1103/PhysRevB.68.014501](https://doi.org/10.1103/PhysRevB.68.014501). URL: <https://link.aps.org/doi/10.1103/PhysRevB.68.014501>.
- [91] Alexandre I. Buzdin, Lev N. Bulaevskii, and Sergei Panyukov. “Critical-current oscillations as a function of the exchange field and thickness of the ferromagnetic metal (F) in an S-F-S Josephson junction”. In: (1982). URL: <https://api.semanticscholar.org/CorpusID:118711826>.
- [92] N. M. Chtchelkatchev, W. Belzig, Yu. V. Nazarov, and C. Bruder. “ π -0 transition in superconductor-ferromagnet-superconductor junctions”. In: *Journal of Experimental and Theoretical Physics Letters* 74.6 (Sept. 2001), pp. 323–327. DOI: [10.1134/1.1421408](https://doi.org/10.1134/1.1421408). URL: <https://doi.org/10.1134/1.1421408>.
- [93] M G Blamire, C B Smiet, N Banerjee, and J W A Robinson. “Field modulation of the critical current in magnetic Josephson junctions”. In: *Superconductor Science and Technology* 26.5 (Apr. 2013), p. 055017. DOI: [10.1088/0953-2048/26/5/055017](https://doi.org/10.1088/0953-2048/26/5/055017). URL: <https://dx.doi.org/10.1088/0953-2048/26/5/055017>.
- [94] S. M. Frolov et al. “Josephson interferometry and Shapiro step measurements of superconductor-ferromagnet-superconductor 0– π junctions”. In: *Phys. Rev. B* 74 (2 July 2006), p. 020503. DOI: [10.1103/PhysRevB.74.020503](https://doi.org/10.1103/PhysRevB.74.020503). URL: <https://link.aps.org/doi/10.1103/PhysRevB.74.020503>.

-
- [95] M. Kemmler et al. “Magnetic interference patterns in $0-\pi$ superconductor/insulator/ferromagnet/superconductor Josephson junctions: Effects of asymmetry between 0 and π regions”. In: *Phys. Rev. B* 81 (5 Feb. 2010), p. 054522. DOI: [10.1103/PhysRevB.81.054522](https://doi.org/10.1103/PhysRevB.81.054522). URL: <https://link.aps.org/doi/10.1103/PhysRevB.81.054522>.
- [96] M Nashaat et al. “Microwave induced tunable subharmonic steps in superconductor-ferromagnet-superconductor Josephson junction”. In: *Low Temperature Physics* (2019). URL: <https://api.semanticscholar.org/CorpusID:202660779>.
- [97] H. Sickinger et al. “Experimental Evidence of a φ Josephson Junction”. In: *Phys. Rev. Lett.* 109 (10 Sept. 2012), p. 107002. DOI: [10.1103/PhysRevLett.109.107002](https://doi.org/10.1103/PhysRevLett.109.107002). URL: <https://link.aps.org/doi/10.1103/PhysRevLett.109.107002>.
- [98] V. V. Bolginov et al. “Magnetic Switches Based On Nb-pdfe-nb Josephson Junctions With a Magnetically Soft Ferromagnetic Interlayer”. In: *JETP Letters* 95 (7 2012), pp. 366–371. DOI: [10.1134/s0021364012070028](https://doi.org/10.1134/s0021364012070028).
- [99] Roberta Satariano et al. “Inverse magnetic hysteresis of the Josephson supercurrent: Study of the magnetic properties of thin niobium/permalloy ($\text{Fe}_{20}\text{Ni}_{80}$) interfaces”. In: *Phys. Rev. B* 103 (22 June 2021), p. 224521. DOI: [10.1103/PhysRevB.103.224521](https://doi.org/10.1103/PhysRevB.103.224521). URL: <https://link.aps.org/doi/10.1103/PhysRevB.103.224521>.
- [100] Timofei I. Larkin et al. “Ferromagnetic Josephson switching device with high characteristic voltage”. In: *Applied Physics Letters* 100.22 (May 2012), p. 222601. DOI: [10.1063/1.4723576](https://doi.org/10.1063/1.4723576). eprint: https://pubs.aip.org/aip/apl/article-pdf/doi/10.1063/1.4723576/14249384/222601_1_online.pdf. URL: <https://doi.org/10.1063/1.4723576>.
- [101] Roberta Satariano. “Master Thesis: Eterostrutture per lo sviluppo di memorie criogeniche.” In: ().
- [102] A. S. Vasenko, A. A. Golubov, M. Yu. Kupriyanov, and M. Weides. “Properties of tunnel Josephson junctions with a ferromagnetic interlayer”. In: *Phys. Rev. B* 77 (13 Apr. 2008), p. 134507. DOI: [10.1103/PhysRevB.77.134507](https://doi.org/10.1103/PhysRevB.77.134507). URL: <https://link.aps.org/doi/10.1103/PhysRevB.77.134507>.
- [103] M. Kupriyanov and Vladimir Lukichev. “Influence of boundary transparency on the critical current of “dirty” SS’S structures”. In: *Zh. Exp. Teor. Fiz. Sov. Phys. JETP* 94 (Aug. 2023).
- [104] S. V. Bakurskiy et al. “Theoretical model of superconducting spintronic SIsFS devices”. In: *Applied Physics Letters* 102.19 (May 2013), p. 192603. ISSN: 0003-6951. DOI: [10.1063/1.4805032](https://doi.org/10.1063/1.4805032). eprint: https://pubs.aip.org/aip/apl/article-pdf/doi/10.1063/1.4805032/13314344/192603_1_online.pdf. URL: <https://doi.org/10.1063/1.4805032>.

- [105] Igor V. Vernik et al. “Magnetic Josephson Junctions With Superconducting Interlayer for Cryogenic Memory”. In: *IEEE Transactions on Applied Superconductivity* 23.3 (2013), pp. 1701208–1701208. DOI: [10.1109/TASC.2012.2233270](https://doi.org/10.1109/TASC.2012.2233270).
- [106] Samme M. Dahir, Anatoly F. Volkov, and Ilya M. Eremin. “Phase-dependent spin polarization of Cooper pairs in magnetic Josephson junctions”. In: *Phys. Rev. B* 100 (13 Oct. 2019), p. 134513. DOI: [10.1103/PhysRevB.100.134513](https://doi.org/10.1103/PhysRevB.100.134513). URL: <https://link.aps.org/doi/10.1103/PhysRevB.100.134513>.
- [107] Igor I. Soloviev et al. “Beyond Moore’s technologies: operation principles of a superconductor alternative”. In: *Beilstein Journal of Nanotechnology* 8 (2017), pp. 2689–2710. ISSN: 2190-4286. DOI: [10.3762/bjnano.8.269](https://doi.org/10.3762/bjnano.8.269). URL: <https://doi.org/10.3762/bjnano.8.269>.
- [108] R. McDermott and M. G. Vavilov. “Accurate Qubit Control with Single Flux Quantum Pulses”. In: *Phys. Rev. Appl.* 2 (1 July 2014), p. 014007. DOI: [10.1103/PhysRevApplied.2.014007](https://doi.org/10.1103/PhysRevApplied.2.014007). URL: <https://link.aps.org/doi/10.1103/PhysRevApplied.2.014007>.
- [109] Kirill G. Fedorov et al. “Fluxon Readout of a Superconducting Qubit”. In: *Phys. Rev. Lett.* 112 (16 Apr. 2014), p. 160502. DOI: [10.1103/PhysRevLett.112.160502](https://doi.org/10.1103/PhysRevLett.112.160502). URL: <https://link.aps.org/doi/10.1103/PhysRevLett.112.160502>.
- [110] S. Nagasawa, H. Numata, Y. Hashimoto, and S. Tahara. “High-frequency clock operation of Josephson 256-word/spl times/16-bit RAMs”. In: *IEEE Transactions on Applied Superconductivity* 9.2 (1999), pp. 3708–3713. DOI: [10.1109/77.783834](https://doi.org/10.1109/77.783834).
- [111] R. Held et al. “Superconducting memory based on ferromagnetism”. In: *Applied Physics Letters* 89.16 (Oct. 2006), p. 163509. ISSN: 0003-6951. DOI: [10.1063/1.2362870](https://doi.org/10.1063/1.2362870). eprint: https://pubs.aip.org/aip/apl/article-pdf/doi/10.1063/1.2362870/14660349/163509_1_1_online.pdf. URL: <https://doi.org/10.1063/1.2362870>.
- [112] Ivan S. Veshchunov et al. “Observation of the magnetic domain structure in Cu_{0.47}Ni_{0.53} thin films at low temperatures”. In: *JETP Letters* 88 (2008), pp. 758–761. URL: <https://api.semanticscholar.org/CorpusID:119281010>.
- [113] Valery V. Ryazanov et al. “Magnetic Josephson Junction Technology for Digital and Memory Applications”. In: *Physics Procedia* 36 (2012). SUPERCONDUCTIVITY CENTENNIAL Conference 2011, pp. 35–41. ISSN: 1875-3892. DOI: <https://doi.org/10.1016/j.phpro.2012.06.126>. URL: <https://www.sciencedirect.com/science/article/pii/S1875389212020639>.

-
- [114] Oleg Mukhanov, Nobuyuki Yoshikawa, Ivan P. Nevirkovets, and Mutsuo Hidaka. *Josephson Junctions for Digital Applications*. Ed. by Francesco Tafuri. Cham: Springer International Publishing, 2019, pp. 611–701. DOI: [10.1007/978-3-030-20726-7_16](https://doi.org/10.1007/978-3-030-20726-7_16). URL: https://doi.org/10.1007/978-3-030-20726-7_16.
- [115] John Clarke and Frank K. Wilhelm. “Superconducting quantum bits”. In: *Nature* 453 (2008), pp. 1031–1042. URL: <https://api.semanticscholar.org/CorpusID:125213662>.
- [116] He-Liang Huang, Dachao Wu, Daojin Fan, and Xiaobo Zhu. “Superconducting Quantum Computing: A Review”. In: *Science China Information Sciences* 63 (2020). DOI: [10.1007/s11432-020-2881-9](https://doi.org/10.1007/s11432-020-2881-9).
- [117] Anton Frisk Kockum and Franco Nori. “Quantum Bits with Josephson Junctions”. In: *Springer International Publishing* (2019). DOI: [10.1007/978-3-030-20726-7_17](https://doi.org/10.1007/978-3-030-20726-7_17). URL: http://dx.doi.org/10.1007/978-3-030-20726-7_17.
- [118] C. Lang et al. “Correlations, indistinguishability and entanglement in Hong–Ou–Mandel experiments at microwave frequencies”. In: *Nature Physics* (2013). DOI: [10.1038/nphys2612](https://doi.org/10.1038/nphys2612). URL: <https://doi.org/10.1038/nphys2612>.
- [119] M.H. Devoret and R.J. Schoelkopf. “Superconducting Circuits for Quantum Information: An Outlook”. In: *Science* 339.6124 (Mar. 2013), pp. 1169–1174. DOI: [10.1126/science.1231930](https://doi.org/10.1126/science.1231930). URL: <https://ui.adsabs.harvard.edu/abs/2013Sci...339.1169D>.
- [120] Yu Chen et al. “Qubit Architecture with High Coherence and Fast Tunable Coupling”. In: *Phys. Rev. Lett.* 113 (22 Nov. 2014), p. 220502. DOI: [10.1103/PhysRevLett.113.220502](https://doi.org/10.1103/PhysRevLett.113.220502). URL: <https://link.aps.org/doi/10.1103/PhysRevLett.113.220502>.
- [121] P Das, R Bruyn de Ouboter, and KW Taconis. “A realization of a London-Clarke-Mendoza type refrigerator”. In: *Low Temperature Physics LT9: Proceedings of the IXth International Conference on Low Temperature Physics Columbus, Ohio, August 31–September 4, 1964*. Springer. 1965, pp. 1253–1255. DOI: [10.1007/978-1-4899-6443-4_133](https://doi.org/10.1007/978-1-4899-6443-4_133). URL: https://link.springer.com/chapter/10.1007/978-1-4899-6443-4_133.
- [122] James C Ho, HR O’neal, and Norman E Phillips. “Low temperature heat capacities of Constantan and Manganin”. In: *Review of Scientific Instruments* 34.7 (1963), pp. 782–783. DOI: [10.1063/1.1718572](https://doi.org/10.1063/1.1718572). URL: <https://pubs.aip.org/aip/rsi/article-abstract/34/7/782/301668/Low-Temperature-Heat-Capacities-of-Constantan-and?redirectedFrom=fulltext>.

- [123] John M. Martinis, Michel H. Devoret, and John Clarke. “Experimental tests for the quantum behavior of a macroscopic degree of freedom: The phase difference across a Josephson junction”. In: *Phys. Rev. B* 35 (10 Apr. 1987), pp. 4682–4698. DOI: [10.1103/PhysRevB.35.4682](https://doi.org/10.1103/PhysRevB.35.4682). URL: <https://link.aps.org/doi/10.1103/PhysRevB.35.4682>.
- [124] FP Milliken, JR Rozen, GA Keefe, and RH Koch. *50 Ω characteristic impedance low-pass metal powder filters*. Vol. 78. 2. AIP Publishing, 2007.
- [125] A Lukashenko and AV Ustinov. “Improved powder filters for qubit measurements”. In: *Review of Scientific Instruments* 79.1 (2008).
- [126] Mark A Cejer et al. *Choosing the optimal source measurement unit instrument for your test and measurement application*. Source measure unit, 2013.
- [127] R. Caruso. “Properties of unconventional S-F-S Josephson junctions.” PhD thesis. PhD Thesis, Università degli Studi di Napoli Federico II, 2017.
- [128] Roberta Caruso et al. “Properties of Ferromagnetic Josephson Junctions for Memory Applications”. In: *IEEE Transactions on Applied Superconductivity* 28.7 (2018), pp. 1–6. DOI: [10.1109/TASC.2018.2836979](https://doi.org/10.1109/TASC.2018.2836979).
- [129] Antonio Vettoliere et al. “High-Quality Ferromagnetic Josephson Junctions Based on Aluminum Electrodes”. In: *Nanomaterials* 12.23 (2022). ISSN: 2079-4991. DOI: [10.3390/nano12234155](https://doi.org/10.3390/nano12234155). URL: <https://www.mdpi.com/2079-4991/12/23/4155>.
- [130] H. Kroger, L. N. Smith, and D. W. Jillie. “Selective niobium anodization process for fabricating Josephson tunnel junctions”. In: *Applied Physics Letters* 39.3 (1981), pp. 280–282. DOI: [10.1063/1.92672](https://doi.org/10.1063/1.92672). eprint: https://pubs.aip.org/aip/apl/article-pdf/39/3/280/7747440/280_1_online.pdf. URL: <https://doi.org/10.1063/1.92672>.
- [131] M. Gurvitch, M. A. Washington, and H. A. Huggins. “High quality refractory Josephson tunnel junctions utilizing thin aluminum layers”. In: *Applied Physics Letters* 42.5 (1983), pp. 472–474. DOI: [10.1063/1.93974](https://doi.org/10.1063/1.93974). eprint: https://pubs.aip.org/aip/apl/article-pdf/42/5/472/7750801/472_1_online.pdf. URL: <https://doi.org/10.1063/1.93974>.
- [132] M. Maezawa et al. “Specific capacitance of Nb/AlO_x/Nb Josephson junctions with critical current densities in the range of 0.1–18 kA/cm²”. In: *Applied Physics Letters* 66.16 (1995), pp. 2134–2136. DOI: [10.1063/1.113927](https://doi.org/10.1063/1.113927). URL: <https://doi.org/10.1063/1.113927>.
- [133] H.J. Mamin et al. “Merged-Element Transmons: Design and Qubit Performance”. In: *Phys. Rev. Appl.* (2021). DOI: [10.1103/PhysRevApplied.16.024023](https://doi.org/10.1103/PhysRevApplied.16.024023). URL: <https://link.aps.org/doi/10.1103/PhysRevApplied.16.024023>.

-
- [134] O. M. Kapran et al. “Crossover between short- and long-range proximity effects in superconductor/ferromagnet/superconductor junctions with Ni-based ferromagnets”. In: *Phys. Rev. B* (2021). DOI: [10.1103/PhysRevB.103.094509](https://doi.org/10.1103/PhysRevB.103.094509). URL: <https://link.aps.org/doi/10.1103/PhysRevB.103.094509>.
- [135] X. Hao, J. S. Moodera, and R. Meservey. “Spin-filter effect of ferromagnetic europium sulfide tunnel barriers”. In: *Phys. Rev. B* (1990). DOI: [10.1103/PhysRevB.42.8235](https://doi.org/10.1103/PhysRevB.42.8235). URL: <https://link.aps.org/doi/10.1103/PhysRevB.42.8235>.
- [136] Guo-xing Miao et al. “Spin regulation in composite spin-filter barrier devices”. In: *Nature Communications* (2014). URL: <https://api.semanticscholar.org/CorpusID:36729849>.
- [137] V. M. Krasnov et al. “Collapse of Thermal Activation in Moderately Damped Josephson Junctions”. In: *Phys. Rev. Lett.* (2005). DOI: [10.1103/PhysRevLett.95.157002](https://doi.org/10.1103/PhysRevLett.95.157002). URL: <https://link.aps.org/doi/10.1103/PhysRevLett.95.157002>.
- [138] Rupert M. Lewis and Michael David Henry. “Decoupling Superconducting Qubits from the Quantum Bus/Readout Resonator to Enable Scaling”. In: (2015). DOI: [10.2172/1504855](https://doi.org/10.2172/1504855). URL: <https://www.osti.gov/biblio/1504855>.
- [139] Joseph C. Bardin, Daniel H. Slichter, and David J. Reilly. “Microwaves in Quantum Computing”. In: *IEEE Journal of Microwaves* 1 (2021). ISSN: 2692-8388. DOI: [10.1109/jmw.2020.3034071](https://doi.org/10.1109/jmw.2020.3034071). URL: <http://dx.doi.org/10.1109/JMW.2020.3034071>.
- [140] Simon Berger. “Master Thesis: OBSERVATION OF BERRY’S PHASE IN A TRANSMON QUBIT”. In: *Laboratory for Solid State Physics, ETH Zurich* ().
- [141] V. M. Krasnov et al. “Anticorrelation between temperature and fluctuations of the switching current in moderately damped Josephson junctions”. In: *Phys. Rev. B* (2007). DOI: [10.1103/PhysRevB.76.224517](https://doi.org/10.1103/PhysRevB.76.224517). URL: <https://link.aps.org/doi/10.1103/PhysRevB.76.224517>.
- [142] Michel H. Devoret et al. “Resonant Activation from the Zero-Voltage State of a Current-Biased Josephson Junction”. In: *Phys. Rev. Lett.* (1984). DOI: [10.1103/PhysRevLett.53.1260](https://doi.org/10.1103/PhysRevLett.53.1260). URL: <https://link.aps.org/doi/10.1103/PhysRevLett.53.1260>.